3D Printed Horn Antenna for Ultra Wideband Applications

By Vegard Midtbøen

Thesis submitted for the degree of
Master of science in Electronics and computer science, Microelectronics
60 credits

Department of Informatics
Faculty of mathematics and natural sciences

UNIVERSITY OF OSLO

Spring 2017

3D Printed Horn Antenna for Ultra Wideband Applications

By Vegard Midtbøen

3D Printed Horn Antenna for Ultra Wideband Applications

http://www.duo.uio.no/

Printed: Reprosentralen, University of Oslo

Abstract

This thesis was initiated by the University of Oslo at the Department of Informatics. The field of study regarding snow analysis, characterization and imaging of snow layers, has been an ongoing study-field at the Department of Geophysics for some years. The transverse collaboration project, Land-ATmosphere Interactions in Cold Environment (LATICE) seeks new advanced instruments for characterizing the impact of climate changes to the snow. In this thesis, 3D printed high gain, ultra-wideband antennas for snow-penetrating radar applications has been simulated and manufactured.

A custom build stepped ridge horn antenna was found to be best suited regarding large bandwidth and high gain that covers the entire band. Two antennas have been constructed and characterized for a gain between 10 dBi to 15 dBi covering the range between 2.3 GHz to 6.1 GHz. The antennas are 3D printed in low cost polylactic acid (PLA) and coated with conductive copper spray. The measured half-power beamwidth for the first printed antenna is 26° in the E-plane and 26° in the H-plane. For the second printed antenna, the half-power beamwidth is 24° in the E-plane and 28° in the H-plane. Measured peak directivity is 12.6 dBi and 12 dBi, and the front-to-back ratio is 22 dB and 24 dB for the first and second antenna, respectively. In addition, a new technique for feeding 3D printed waveguide structures are presented. The work on this feeding technique has been submitted to the IEEE MTT-S International Microwave Workshop Series on Advanced Materials and Processes (IMWS-AMP) conference in September 20-22, 2017 (Appendix A).

The antennas have been tested together with the Novelda X2 Ventricorder module at the snow lab at the Department of Informatics, and outdoor measurements at Finse Alpine Research Center, Norway. Promising results has been achieved from these measurements. The radar is able to detect different layers of pressed wood with a measured permittivity of 1.89. Results from the outdoor measurements has been shown in the end of the thesis, but not verified due to limited time.

Contents

Preface

This thesis was submitted for the degree of Master of Science (M. Sc) at the University of Oslo at the Department of Informatics. The work has been carried out in the period, January 2016 to May 2017 under the supervision of Professor Tor Sverre Lande (UiO), Ph. D. Kristian Gjertsen Kjelgård (UiO) and Professor Dag T. Wisland (UiO/Novelda). The assignment was given by the Department of Informatics, NANO group, as a collaboration project with the Department of Geophysics.

First, I would like to thank my supervisors for excepting me for this interesting assignment and giving continuous feedback and excellent guidance through the hole process. Their help has been essential to me for managing this task. Also, a special thanks goes to Jon Håvard Eriksrød and Mathias Tømmer for good help on antenna design and radar measurements, as well as a nice field trip to Finse with Håvard. Thanks to senior engineer Olav Stanly Kyrvestad for making it easy to order components and other stuff.

I would also like to give a special thanks to my lab-partner Espen Klein Nilsen for good help, and a lot of off topic discussions. I also would like to thank the rest of the master students at ELDAT and NANO for two nice years. Lastly, I would like to thank ROBIN for allowing me to use their 3D printer and Novelda for supporting with the Ventricoder module.

Oslo, Norway, May 2017
Vegard Midtbøen

Chapter 1

Introduction

1.1 Surface Penetrating Radar

Geophysicists and climatologists has for several years been interested in seeing the thickness and structural aspects of ice and snow. Snow analysis is important for several reasons, among them the importance of mapping the potential risk for snow avalanches. So fare, the most used and reliable method is to dig snow pits and manually analyses the snow layer structure. This is very time-consuming and not very efficient if a large area is to be mapped. A faster method is to use snow sticks to *feel* the snow-layer by hand. This is done by applying different forces to the stick in order to penetrate each layer. If much force is needed, it is almost sure that there exists an ice layer. However, this method is not particularly reliable because some layers may be difficult to feel. There exists some products on the market that makes it possible to measure the applied force [1], but is a large area covered by snow is to be mapped, it will be inefficient to use these methods.

Surface penetrating radars has been around for several years and can penetrate the surface and make images of the segments of the earth beneath. These radars can be used for many different applications, for example mapping of water pipes, mine detection, locate artifacts and snow imaging. Figure 1.1 shows one example where a surface penetrating radar is used on a groomer for snow analysis. Common for

Figure 1.1: Image of a typical GPR mounted on a snow groomer. From [2]

most of these radar systems, is that they operate in the VHF/UHF band (IEEE standard 30 MHz-300 MHz/300 MHz-1 GHz [3]). Low frequencies requires large antenna apertures and for many applications this will be impractical to carry out in the field.

Lately, a company named Novelda AS has developed a high precision short range radar (named X2) operating in the C-X band (IEEE standard 4 GHz-12 GHz) [4]. A special version of this radar was created for medical research and is called Ventricorder. This model has a lower frequency band which makes it suitable for medical and snow imaging applications. The Ventricorder operates in the S-C band (IEEE standard 2 GHz-8 GHz) with a center frequency of 3.9 GHz. The X2 radar can *see* through walls with relative high permittivity, which makes it suitable for Snow Penetrating Radar (SPR) applications [4].

1.2 History

Radars has been around for several years, and are often associated with military usage for airplane and missile detection, or police radar controls. The history of radar extends all the way back to late 1800 and early 1900, when Heinrich Hertz (1857 - 1894) first demonstrated reflection of radio waves and Nikola Tesla (1856 - 1943) described a concept for electromagnetic detection and velocity measurements [5]. The first use of electromagnetic signals for detecting the presence of distant objects relates back to 1904 and Christian Hülsmeyer (1881-1957). Hülsmeyer created the first ship collision avoidance system that were able to detect ships up to a distance of 3 kilometers. This was pioneering work on detection of nearby ships under foggy weather conditions. However, Hülsmeyers "Telemobiloscope" was not able to measure distance and target location based on the traditional radar technology, only the existence of the object [6] [7]. In 1926, Dr. Hülsenbech introduced the first pulsed radar that were able to determine the structure of buried features [6] [8]. He discovered that any variations in the dielectrics would reflect parts of the transmitted signal. In the middle and late 1930s, the United States, Britain, Germany, France, Russia, Italy and Japan started rapidly the development of radar systems. In 1936, the US demonstrated the first pulsed radar, and in 1938 they developed the first antiaircraft fire control system, the CCR-268. The same year, Britain developed their first pulse radar and created the famous Chain Home surveillance system that was actively used to the end of WW2 [5].

In the 1970s, the US Army Engineering Research and Development Command (ERDC) rapidly started to develop radars for snow and ice imaging in the arctic areas of Alaska and Antarctica. In 1975, the Geological Survey of Canada started the research of understanding the permafrost in the Canadian Arctic. Figure 1.2 shows an image of the radar system that was used for this research [9, pp. 5].

Figure 1.2: GPR system in operation for geological survey in the Canadian Arctic, from [9, pp. 5]

1.3 Motivation and goals

At the University of Oslo there are an on-going transverse collaboration project between the Department of Geophysics and Department of Informatics called Land-ATmosphere Interactions in Cold Environments (LATICE). Climate changes impacts the Earth more rapidly, especially in the high latitudes. Therefore, the need of more highly sophisticated sensors are crucial in order to get a better understanding of the climate impact of the ice and snow.

A more consumer related application using radar technology to penetrate the surface, is the detection of potential risk for snow avalanches. Since 2014 there has been recorded over 350 near-accidents in Norway where humans have been involved. In addition to those accidents there has been recorded totally 14 death accidents in the same period of time [10]. A snow avalanche may be triggered from a 30° increment in the terrain, and can extend twice as long in the horizontally field as the size of the avalanche release area. Therefore, a snow avalanche may strike anyone who are skiing in the mountain surrounded by hills or summits. Figure 1.3 shows a snow avalanche release point. The risk for snow avalanches increases if there exists a fine crystal layer, often called sugar-layer because it reminds of sugar, and a ice layer beneath.

Figure 1.3: Image showing a snow avalanche release point, from [11]

The need for a easy-to-carry snow penetrating radar system able to image or detect dangerous snow layers, are necessary for scientists to map a potentially large area. To do so, a light weighted radar system is needed. Commercially available antennas suitable for this type of application, are both large and heavy, and not particular suited for light weight applications. In the past years, 3D printing technology has shown to be a promising technique for manufacturing antennas. These plastic antennas need to be copper coated in order to be conductive, so that currents can flow on the surface of the antenna.

The main goal for this thesis will be to design and develop a light weight 3D printed antenna, suitable for snow imaging and snow layer detection purposes. This will require antennas with high gain and large bandwidth in order to get detailed images of the snow profile.

Chapter 2

Background

The purpose of this chapter is to give a brief overview of basic radar concepts with focus on the dielectric properties, especially for snow. Further, a short introduction to snow avalanche and snow profiles will be given, followed by a short discussion of some high gain, ultra-wideband antennas suitable for snow imaging applications. In the end, parameters for designing a pyramidal horn antenna will be given.

2.1 Fundamentals of RADAR

Radio detection and ranging, or commonly known as RADAR is familiar to most people. Since the first use of pulsed radars in the early 1900, the development of many different types of radar systems has rapidly increased. The police traffic radar is probably common to most people. The principles of radar are much the same as sound-wave reflection. If one shout in one direction it is often possible to hear the echo, especially if you are located in the mountains. The radar works in the same way. An antenna transmit a pulse to a target, either through air or other types of mediums and the scattered (reflected) signal is received by the same, or a different antenna depending on the application. Using this concept, radars can be used in a variety of applications, like imaging, tracking or detection [5, pp. 1-2] [12].

2.1.1 Target detection

In vacuum, electromagnetic waves travels at the speed of light. The total distance the pulse need to travel for detecting an object, is two times the distance to the object, or 2R. The traveling time can be found by recording the time between the transmitted and received pulse. One can therefore express the distance to the object by the following formula from basic physics [5]

$$R = \frac{c\Delta t}{2} \tag{2.1}$$

where: c = speed of light
Δt = pulse traveling time.

All excising materials have different dielectric properties which will influence the reflected signal. The dielectric constant is expressed in terms of a real and an imaginary part. The real part is called the real permittivity which is related to the

stored energy within the medium. The complex part of the permittivity related to the dispersion, or losses of energy within the medium. The complex dielectric constant is given as [13, pp. 37]

$$\varepsilon = \varepsilon' - j\varepsilon'' = \varepsilon' - j\frac{\sigma}{\omega\varepsilon_0} \tag{2.2}$$

where: ε' = real part of the permittivity
ε_0 = permittivity in vacuum ($8.85x10^{-12}F \cdot m^{-1}$)
σ = conductivity
ω = frequency.

The velocity of the propagating wave is dependent on the relative permittivity of the material. Eq. (2.1) assumes that the wave is propagating with a velocity of speed of light. This is true for vacuum, but for all other materials, this will not be the case. A more accurate expression for the velocity is expressed as

$$v_r = \frac{1}{\sqrt{\mu\varepsilon}} = \frac{1}{\sqrt{\mu_0\mu_r\varepsilon_0\varepsilon_r}} \tag{2.3}$$

where: μ_0 = permeability in vacuum ($4\pi x10^{-7}H/m$)
μ_r = relative permeability
ε_r = relative permittivity.

In almost all cases, the relative permeability is equal to one. The expression above can therefore be simplified to

$$v_r = \frac{c}{\sqrt{\varepsilon_r}}. \tag{2.4}$$

Inserting Eq. (2.4) into Eq. (2.1) is necessarily to estimate the distance to the target. This is especially important for non-air radar applications, like human body imaging, through wall detection or ground/snow penetrating radar applications where ε_r is unequal to one.

2.1.2 Dielectric properties of a material

The dielectric properties of a material describes how the material reacts to electromagnetic waves. The dielectric constant expressed in Eq. (2.2) consists of the real permittivity (real part) and a loss factor (imaginary part). The loss tangent ($\tan\delta$) is a ratio between the complex and the real dielectric constant, indicating the losses in a medium. Mathematically, the loss tangent is expresses as

$$\tan\delta = \frac{\omega\varepsilon'' + \sigma}{\omega\varepsilon'}. \tag{2.5}$$

Rewriting Eq. (2.2) by inserting Eq. (2.5), one can express the complex dielectric constant as

$$\varepsilon = \varepsilon_r\varepsilon_0(1 - j\tan\delta). \tag{2.6}$$

For a loss-less materials, the loss factor is equal to zero, which gives a dielectric constant of [14]

$$\varepsilon = \varepsilon_r\varepsilon_0. \tag{2.7}$$

In the real world, such as loss-less materials does not exist. Both the real permittivity and the loss factor varies depending on the type of material. For SPR applications, these differences in the dielectric materials is important considerations in order to determine the different layer structures. This will be discussed more in an later section. Table 2.1 summarizes some dielectric properties for some typical materials.

Material	Frequency	ε_r	tan δ	Temperature
Alumina (99.5%)	10 GHz	9.5 - 10	0.0003	25°
Teflon	10 GHz	2.8	0.0004	25°
Glass (pyrex)	3 GHz	4.82	0.0054	25°
Water (distilled)	3 GHz	76.7	0.1570	25°
Polyethylene	10 GHz	2.25	0.0004	25°
Ceramic (A-35)	3 GHz	5.60	0.0041	25°
Ceramic (A-35)	9.375 GHz	5.60	0.0041	-4°

Table 2.1: Different permittivities and loss factors for some materials, from [15].

Dielectric properties of snow

In this thesis, the focus will be on the characterization against snow. This section gives a short introduction to the dielectric properties of this material. Snow is a mixture of ice and air. Therefore, the complex dielectric constant for dry snow (ε_{ds}) is a mixture of the dielectric constant for air (ε_h), dielectric constant for ice (ε_i), and a ice volume factor (v_i) [13, pp. 140]. The volume factor is defined by

$$v_i = \frac{\rho_s}{0.9167}, \tag{2.8}$$

where the constant 0.9167 g/cm^3 is the density of pure ice. In [13], there has been some work around the estimation and measurement on the dielectric properties of snow. It was shown that the dielectric constant for dry snow (ε_{ds}) could be expressed by the volume factor (v_i) and the complex dielectric constant for ice (ε_i). If one assumes that the imaginary part is much less than the real part for the dielectric constant ($\varepsilon''_{ds} \ll \varepsilon'_{ds}$), one can remove the imaginary part from the expression. Then, by using a typical value for the real permittivity of ice, $\varepsilon_i = 3.17$, the following result is obtained for the real part of the dielectric constant for dry snow [13, pp. 140]

$$\varepsilon'_{ds} = \frac{1 + 0.84 v_i}{1 - 0.42 v_i}. \tag{2.9}$$

Figure 2.1 (a) shows a plot of the estimated formula given in Eq. (2.10) for the relative permittivity as a function of snow-density together with measured permittivity for a wide frequency range. The estimation shows a good match to the measured results. In Figure 2.1 (b), the loss factor is plotted as a function of temperature. It was shown in literature that the permittivity is almost unaffected by variations in temperature and frequency. This is not the case for the loss factor. From Figure 2.1 (b), it can be seen that for a density of $\rho_s = 0.76$ at 9.375 GHz, the loss factor varies from 18x30^{-4} (0.0054) at -0°C, to 5.8x30^{-4} (0.0174) at -18°C.

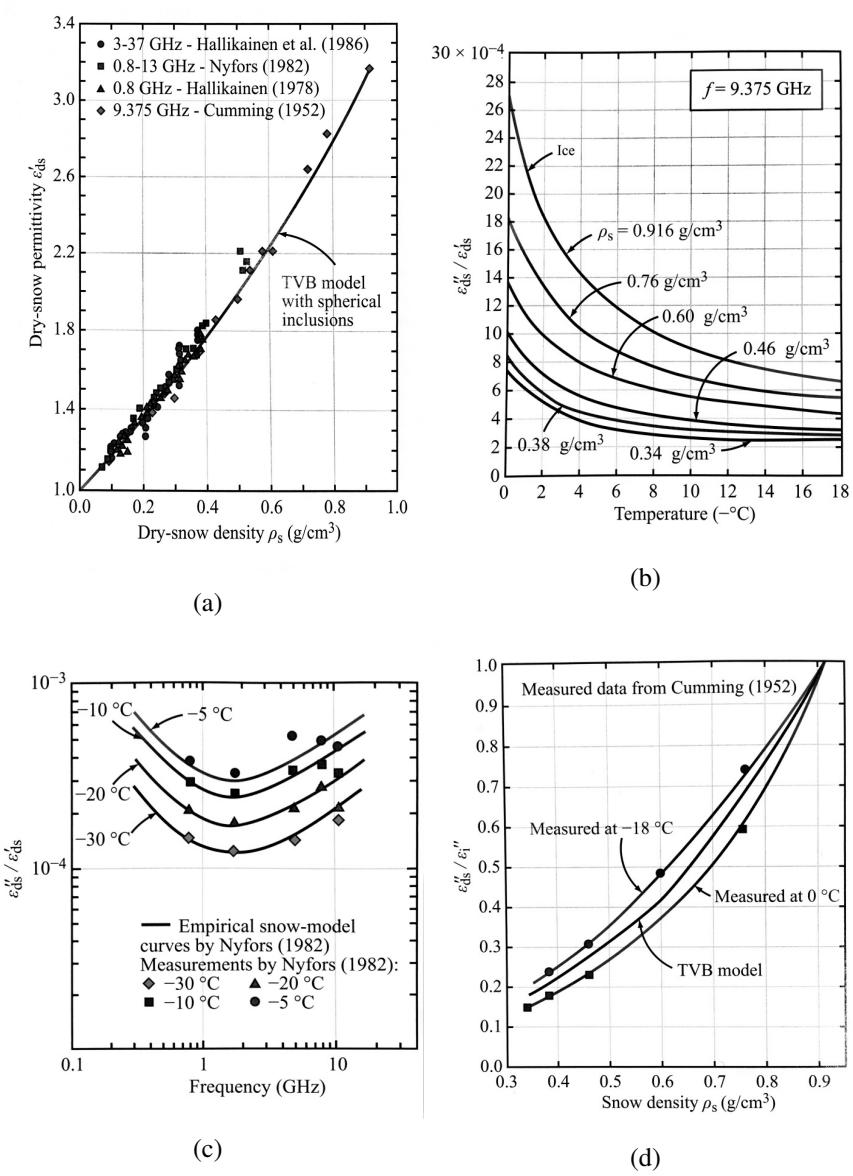

Figure 2.1: (a) showing a plot of measured permittivity of dry snow as a function of snow density, and (b) showing the loss factor as a function of temperature at 9.375 GHz. (c) shows a plot of the loss tangent as a function of frequency and (d) shows a plot of estimated $\varepsilon''_{ds}/\varepsilon''_i$ compared to measured. From [13, pp. 141 - 143].

Figure 2.1 (c) shows a plot of the loss tangent ($\varepsilon''_{ds}/\varepsilon'_{ds}$) for a frequency range between 0.8 GHz to 12.6 GHz at different temperatures. The plot clearly shows that the loss tangent is strongly affected by variations in both temperature and frequency. Recalling that dry snow is mixture of ice and air, one can develop the following expression for the loss factor given as

$$\varepsilon''_{ds} = \frac{0.34 v_i \varepsilon''_i}{1 - 0.42 v_i^2} \tag{2.10}$$

In Figure 2.1(d), a plot of the loss tangent as a function of snow density is presented together with measured results at -18° and -0°. It can be seen that the estimations is a good approximation and is close to the measured results.

So far, only dry snow has been discussed. Since wet snow contains of more water, it is expected that the water will strongly affect the dielectric constant. Figure 2.2 (a) shows a plot of the wet snow permittivity (ε_s') as a function of frequency. Each

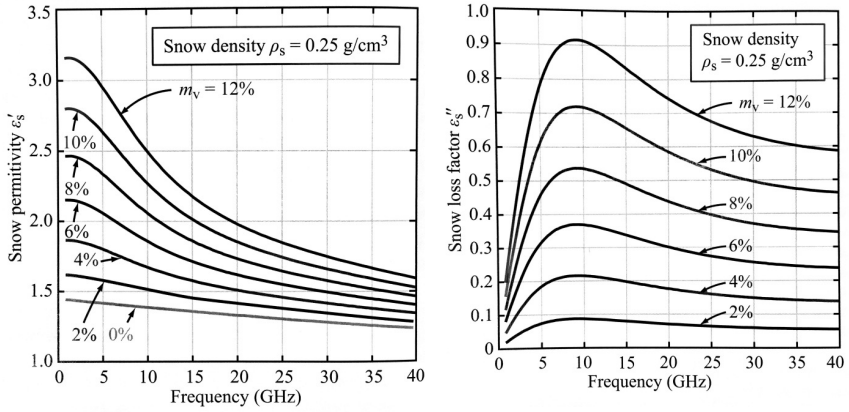

(a) (b)

Figure 2.2: (a) showing a plot of measured permittivity of wet snow as a function of frequency, and (b) showing the loss factor as a function of frequency. From [13, pp. 144].

of the curves represents different densities of water in the snow. It is shown that for low frequencies, the variation in the permittivity is strongly affected by the water content. At higher frequencies, this variations are almost negligible. The study of dielectric properties for wet snow was presented by Hallikainen et al. in [16] [17] [18]. Figure 2.2 (b) shows a plot of the loss factor as function of the frequency. Here, it is observed that for 3 GHz to 6 GHz, ε_s'' has a steep slope. This is due to the large increase in the magnitude of ε_w'' for water over the frequency range [13, pp. 145].

The study of the dielectric properties for snow are important in order to estimate how the wave will be affected at different types of snow layers. It has been shown that the relative permittivity is relatively low for both dry and wet snow. The difference lays in the losses. Dry snow has a typical loss factor of about 0.0171 (0.0054x3.17) to about 0.247 (0.078x3.17), strongly affected by both the temperature, density and frequency. For wet snow, it was shown that the loss factor varied between 0.02 to about 0.9. This is considerable much more losses than for dry snow. The more practical issues will be discussed in a later section.

2.1.3 Resolution

For applications where only the depth from the surface to the ground is required, for example from the snow surface to ground, it is possible to place the radar at a

specific position and measure the time between the transmitted and received pulse. However, for most surface penetrating radar applications, it is desirable to see more information about what is in between the radar and the ground, for example pipe lines, buried mines, soil layer structure or even snow layer structure, which is the main focus in this thesis [19]. The radars ability to distinguish between two or more objects are called resolution. The resolution can be divided into two main categories; range resolution (downrange) and cross range resolution (often called azimuth resolution). The range resolution is the ability to detect two or more closely separated objects in the depth and is directly proportional to the system bandwidth. The cross range resolution is the ability to detect two or more closely separated object at the same distance away from the radar. Figure 2.3 shows an illustration of the basic resolution concept to a aircraft radar detection system. The resolution of the radar are an important considerations if one want to create radar images.

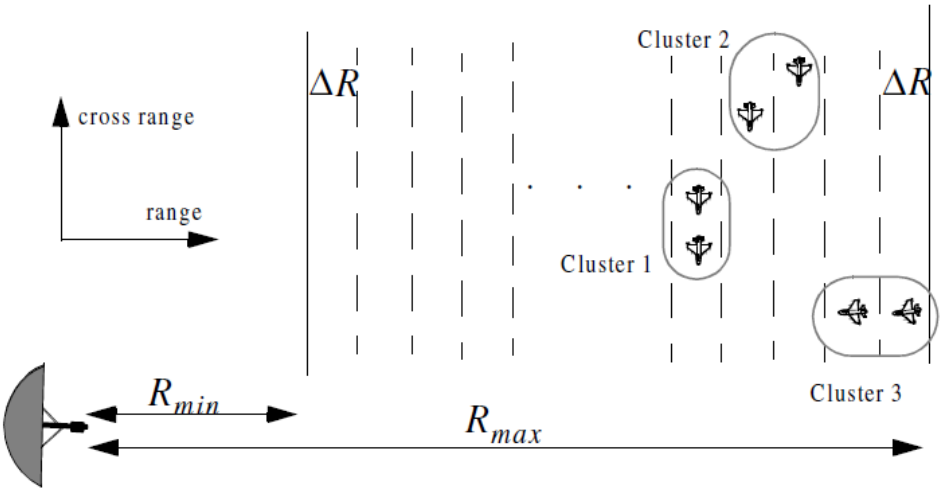

Figure 2.3: Resolution of a radar system illustrated. Resolution is divided into *range resolution* and *cross range resolution*. From [20].

Range resolution

The range resolution is the minimum distance between two closely separated targets in the depth field of the radar, as was seen in Figure 2.3. Range resolution, denoted ΔR, is directly proportional to the system bandwidth in the following relation

$$\Delta R = \frac{c\tau}{2} \tag{2.11}$$

where: c = speed of light
τ = pulse width in seconds.

Since the pulse width is proportional to the system bandwidth as

$$B = \frac{1}{\tau}, \tag{2.12}$$

one can rewrite Eq. (2.11) as

$$\Delta R = \frac{c}{2B}. \tag{2.13}$$

The band resolution is best understood by looking at the amplitude modulated sine waves shown in Figure 2.4. A signal having a large pulse duration in the time domain, is having a narrow bandwidth in the frequency domain. For a pulse with a short time duration, the opposite applies. Figure 2.5 shows the concept of having

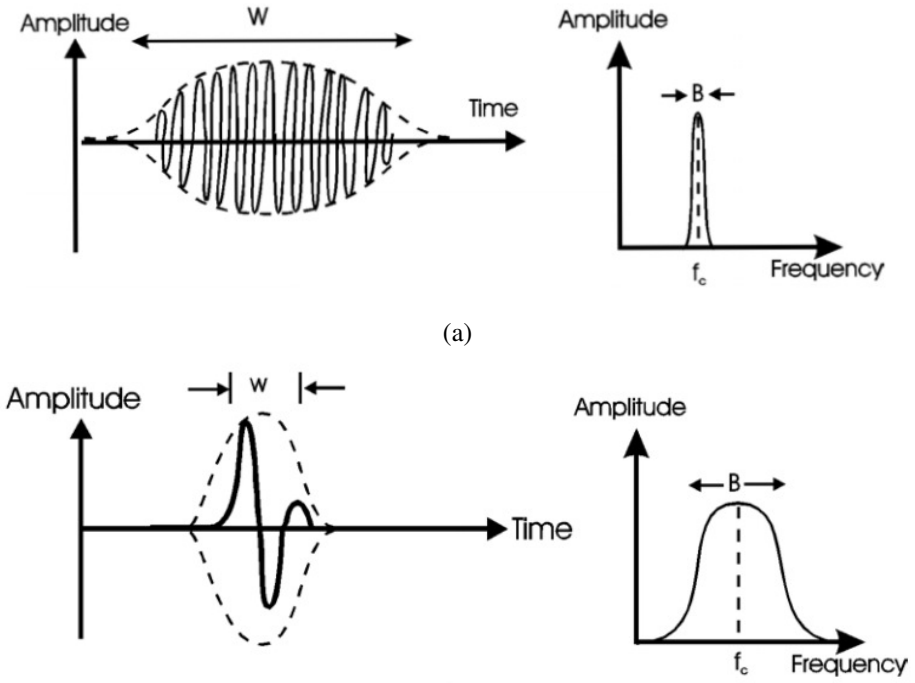

Figure 2.4: (a) showing a narrow bandwidth signal and (b) showing a wide-banded signal, from [9, pp. 93-103]

a wide bandwidth for optimal range resolution. A long pulse width (green line) are not able to detect the two objects because the reflections from the two objects cancel because of the signal bandwidth. For a small pulse width, the two object is detected because the range resolution are smaller than the pulse width.

Cross range resolution

The cross range resolution is the ability to detect closely separated objects that are located at the same distance away from the antenna, as was seen in Figure 2.3. The cross range resolution is often associated with *Real-aperture radars* (RAR) and *Synthetic Aperture Radars* (SAR). These types of radars can create two dimensional (in some cases three-dimensional) images of the ground surface by sweeping over a area and measure the distance to the target. Figure 2.6 shows an illustration of a RAR measuring the distance to the ground. The resolution cell is the area defined by the range resolution and cross range resolution. A smaller resolution cell gives a more accurate image. For a RAR system, the antenna has a large aperture size in the horizontal direction and small aperture size in the vertical direction. A large

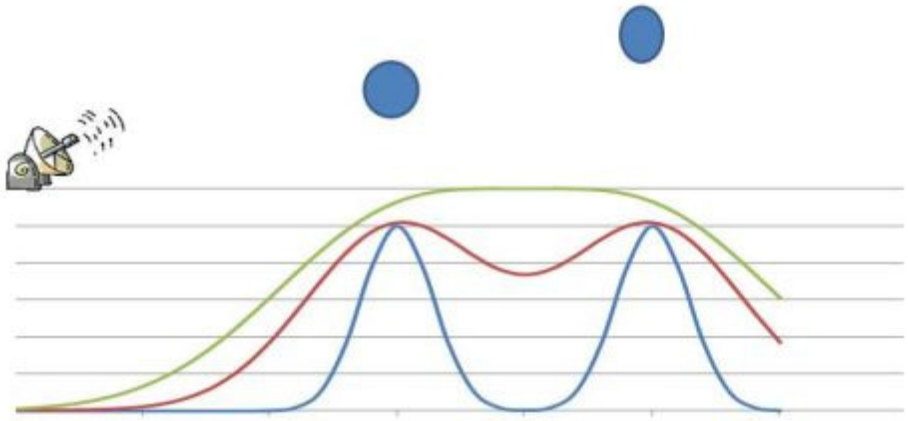

Figure 2.5: Range resolution concept. Large pulse width (green) are not able to detect closely separated object. A shorter pulse width (blue) detects the two targets. From [21].

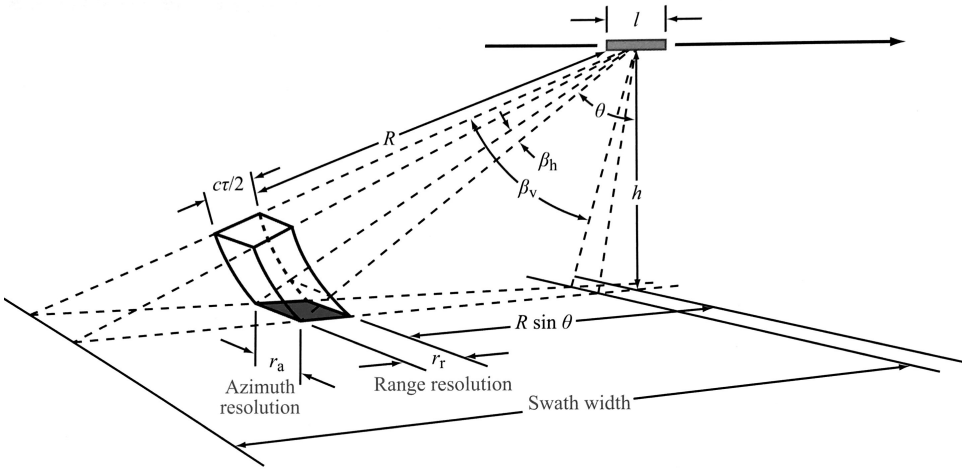

Figure 2.6: Real-aperture radar (RAR). The accuracy is determined by the resolution cell which is defined by the range resolution and cross range resolution. From [13, pp. 173].

aperture antenna gives a narrow beamwidth gives as

$$\theta = \frac{\lambda}{l} \tag{2.14}$$

where: λ = wavelength
l = antenna length.

The cross range resolution (ΔCR) is defined by the beamwidth for the antenna and the distance to the target given as

$$\Delta CR = \theta R. \tag{2.15}$$

Inserting Eq. (2.14) into Eq. (2.15) gives

$$\Delta CR = \frac{\lambda R}{l}. \tag{2.16}$$

The range- and cross range resolution can be used in the radar equation to determine the total power delivered to the receiving antenna. The total power at a given angle (θ) is expressed as [13]

$$\langle P_p^r(\theta) \rangle = \left[\frac{P_q^t \lambda^3 G^2(\theta) c\tau}{2l(4\pi)^3 R^3 sin\theta} \right] \cdot \sigma_{pq}^0(\theta) \tag{2.17}$$

where: P_q^t = power delivered from transmitter
λ = wavelength
$G^2(\theta)$ = Gain in a direction θ
c = speed of light
τ = pulse width
l = aperture length
R = distance from antenna to target
σ_{pq}^0 = backscattered cross section per unit area.

2.1.4 Antennas

Antennas are the radar systems "eyes" and "ears'. The Institute of Electrical and Electronic Engineers (IEEE)'s Standard Definition of Terms for Antennas (IEEE std. 145-1973) defines an antenna as *"a mean for radiating or receiving radio power"*. In practice, the antenna works as a radiating element which acts as a transducer between an electrical signal in a system and a propagating wave [20]. In many ways, the antenna can be treated as a transmission line between a source (typically 50Ω) and a load with a given impedance (typically air (377Ω)). The purpose of the antenna, besides what has been explained, is to focus as much of the transmitted energy as possible in a decried direction. The field of which the antenna is able to transmit energy is called the antenna beam. The shape of the beam is strongly determined by the aperture size. A large antenna aperture results in a narrow beamwidth. In most radar systems, it is desirable to have a narrow beamwidth on order to detect closely separated objects [22, pp. 538-539].

A radar antenna is characterized by its gain, radiation pattern, polarization, bandwidth and aperture size. In the following sub-sections, each of these terms will be briefly explained.

Antenna directivity and gain

The directivity of the antenna can be described by the following term [20]

$$D = \frac{maximum\ radiation\ intensity}{average\ radiation\ intensity}, \tag{2.18}$$

or expressed by by its solid angles (θ, ϕ)

$$D = \frac{1}{\frac{1}{4\pi}\iint F(\theta,\phi)d\Omega} = \frac{4\pi}{\Omega_A} \tag{2.19}$$

where: Ω_A = beam solid angle.

However, a more approximate expression for the directivity can be made by assuming that the antenna has one narrow major lobe and very negligible minor lobes. Eq. (2.19) can thereby be written as

$$D = \frac{4\pi}{\Theta_{1r}\Theta_{2r}} \tag{2.20}$$

where: Θ_{1r} = half-power beamwidth in one plane (rad)
Θ_{2r} = half-power beamwidth in a plane at a right angle to the other (rad).

The gain describes how much of the radiated signal that is concentrated in a given direction. The gain for an antenna is directly related to the directivity. In fact of one neglects the antenna losses, the gain is equal to the directivity. Therefore, the gain can be expressed as a function of the directivity times a efficiency constant, or [23, pp. 19-25]

$$G = De_0 \tag{2.21}$$

where: D = directivity
e_0 = efficiency.

Radiation pattern

The radiation pattern gives a graphical representation of the antenna radiation properties. This can be represented in several ways; field patter (linear scale), power pattern in linear scale and power pattern in decibel scale. The most common is to define the pattern in order of power in dB. The angle of the beam (beamwidth) is defined by its half-power beam width (HPBW), which is defined by the -3 dB point from the maximum directivity [23, pp. 3-5].

Polarization

The polarization of the antenna defined as the *"property of an electromagnetic wave describing the time-varying direction and relative magnitude of the electric-field vector; specifically, the figure traced as a function of time by the extremity of the vector at a fixed location in space, and the sense in which it is traced, as observed along the direction of propagation"* [23, pp. 27]. The polarization can be either linear, circular or elliptical. In this thesis, only linear polarized antennas will be discussed.

Bandwidth

The bandwidth of an antenna does not have a common definition applying for all types of antennas. For example, for a wideband antenna the bandwidth is defined for its upper and lower frequency in the acceptable value of either input impedance, pattern, beamwidth, polarization, side lobe level, gain, beam direction or, radiation efficiency. For a narrow band antenna the bandwidth is defines as a percentage of the upper and lower frequency difference over the center frequency [23, pp. 26]. In this thesis, the bandwidth will be defined by the upper and lower frequency at which point the reflected signal is 10 %, or -10 dB of the transmitted signal.

Effective aperture

For an effective antenna the gain is approximately equal to the beam pattern. The efficiency of the aperture is given by the following expression

$$A_e = \frac{P}{W} \tag{2.22}$$

where: P = Power delivered to the antenna
W = Wave power density

The effective aperture is defined as; *"The effective aperture is the area A_e such that, if all the power incident on the area was collected and delivered to the load with no loss, it would account for all the observed power outputs of the actual antenna"* [5, pp.11 - 12]. Knowing the effective aperture, one can express the directivity of a antenna as

$$D = \frac{4\pi}{\lambda^2} A_e \tag{2.23}$$

where: λ = wavelength

2.2 Using radar for snow imaging

Snow penetrating radars (SPR), or more commonly known as surface penetrated radars has been around for several years. Sophisticated radar systems, like the pulseEKKO GPR [24] are able to see through the snow or ice surface and create images of the snow profile and ground, as can be seen in Figure 2.7. Most surface

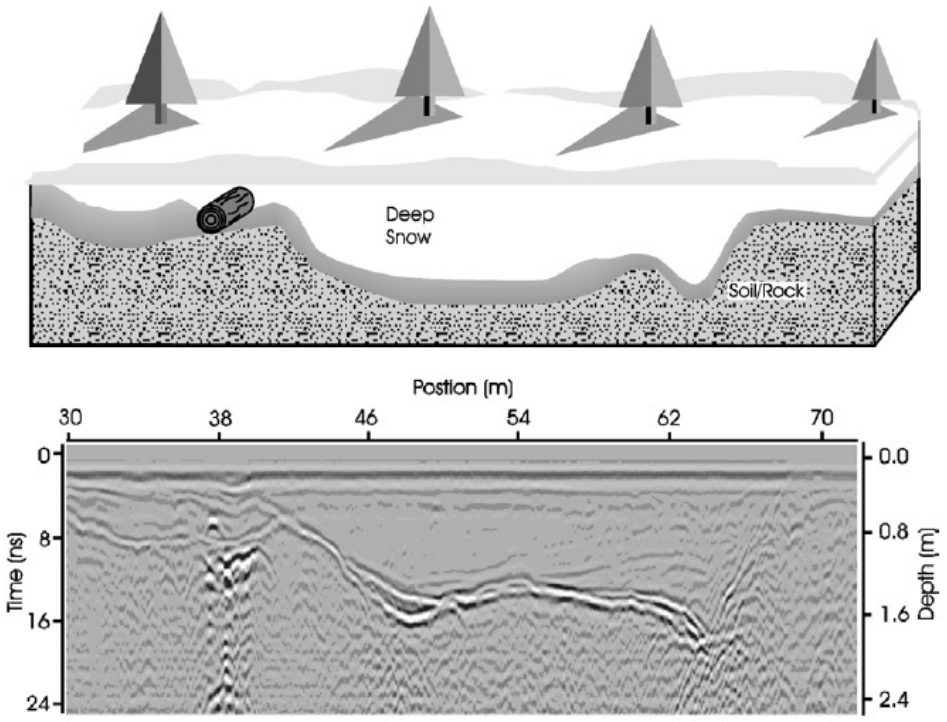

Figure 2.7: Illustration and GPR measurement of snow profile using pulseEKKO 1000 operating at 900 MHz. From [9]

penetrating radars operate in the MHz range. Because low frequencies are less affected by the permittivity, these radars can penetrate the snow/ice up to several hundreds of meters. However, these radar systems are not particular accurate regarding the resolution. In order to extend the resolution, one must increase the bandwidth, as was discussed in an earlier section. Increasing the bandwidth limits the maximum depth the radar is able to penetrate because it is more exposed to reflections. A second option is to increase the center frequency which enables even higher bandwidths. Figure 2.8 (a) shows an image of a ground profile over two highway tunnels using a pulseEKKO GPR at 50 MHz. One can clearly see the shape of the two tunnels, and some information about the ground profile. In Figure 2.8 (b), the same two tunnels have been scanned for a frequency of 100 MHz. The tunnels are still visible but not nearly as clear as it was for the 50 MHz measurement. However, the image contains more information about the ground soil [9]. In applications where information about the snow layers are desirable, one must increase the frequency range.

Radar systems operating in the MHz-range require relatively large antennas. For

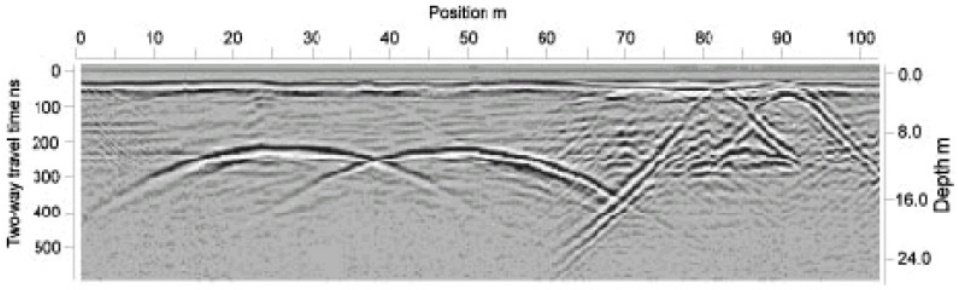

(a)

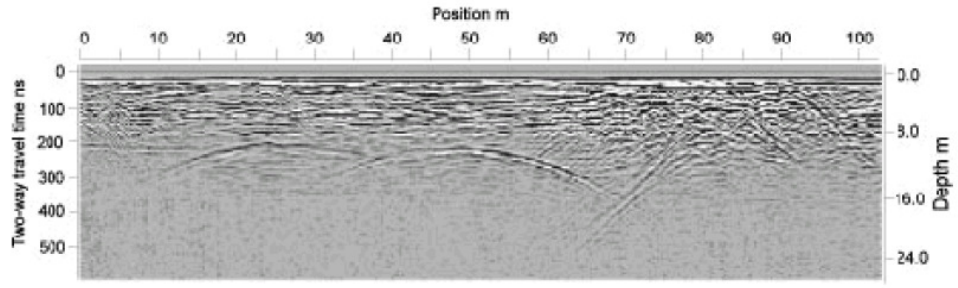

(b)

Figure 2.8: (a) showing an image scan using pulseEKKO at 50 MHz, and (b) is showing a scan from the same radar at 100 Mhz. From [9]

remote Geo-Sensing applications, it is desirable to have a radar system that is easy to carry out in the field. Also, for detection of possible risk of snow avalanche the need for long depth measurements are not particularly interesting. Instead, more information about the snow profile is the main goal. In fact, increasing the frequency and hence the bandwidth is crucial for detecting different layers in the snow. This will be discussed in the next section.

2.2.1 Snow avalanches

The risk of potential snow avalanche exists in all areas where the mountain or hill has a 30° slope or more. The avalanche area is often divided into two main zones; starting zone and deposition zone. The staring zone is the area where the potential risk of an avalanche can occur. The deposition zone is the area where the avalanche may strike and can be two times as long as the starting zone [25].

Over time, temperature and wind will change the snow characteristic and create different layers in the snow pack. Figure 2.9 shows a typical snow pack with different layers. In the middle of the figure, it is shown two layers indicated *Weakest* and *Ice*. These two layers are the main reason for an avalanche to happen. The weakest layer can be as thin as one centimeter and up to some few centimeters thick and consists of snow crystals formed during cold and windy conditions. The crystals looks like sugar, and is therefore often called sugar-layer. If a crystal-layer lays on top of a ice layer as seen in the figure, the hole snow pack above the crystal-layer will eventually start to glide if the slope is steep, or if it gets triggered by a skier or by weather conditions.

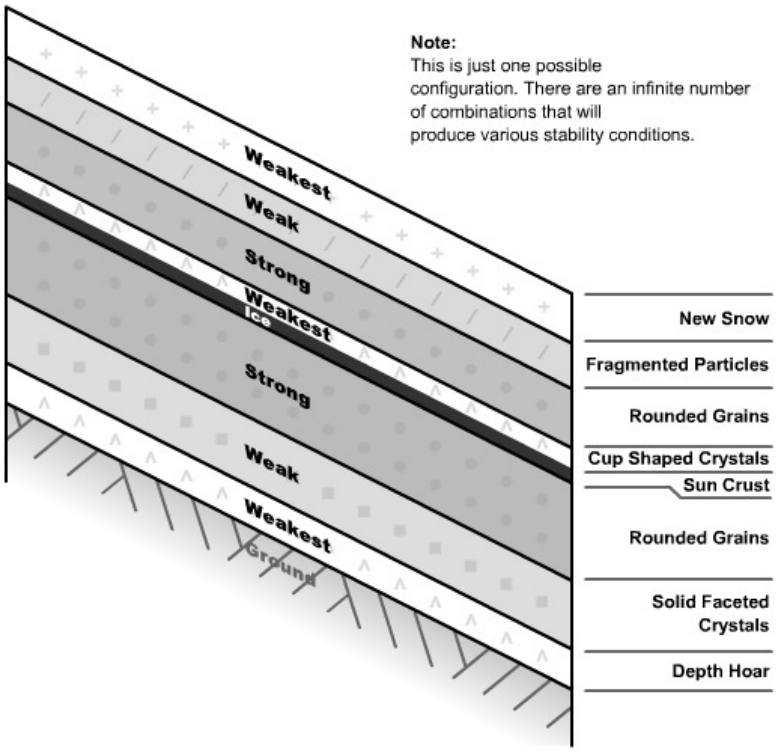

Figure 2.9: One possible snow layer configuration. From [26].

Because of the low thickness of these crystal-layers, it is important to have a radar with a high resolution. Some layers are very wet and some are dry which means that each layer will have different dielectric constants. This makes it possible to distinguish between the different layers. Since the crystal layer is a mixture of ice and air, it is not expected much reflections from this layer. The same applies for the ice layer. For pure water, the relaxation lays in the microwave region, meaning that one would expect much reflections from pure water. For ice, the relaxation lays in the kilohertz region, which means that microwave signal will just go straight through without major losses [13, pp. 124-129]. Therefore, it may be difficult to distinguish between the ice and crystal layer. However, reflections from the layer beneath the ice layer may be achievable making it potentially possible to locate the critical area.

To summarize, having a large bandwidth is crucial in order to get a high enough resolution to be able to distinguish between small (in order of some few centimeters) layer of ice and snow crystals.

2.2.2 Surface penetrating radars

As was explained in the beginning of this section, surface penetrating radars are used to crate images of the surface or ground. The goal for this thesis is to create a SPR for remote Geo-Sensing applications. To address the concept of SPR, this sub-

sections starts by explaining the basic concept of GPRs as these two applications uses the same type of technology.

Ground Penetrating Radars

For imaging applications of the ground soil, GPRs has been the preferred technology to use since it was first invented in the early 1900. GPRs uses electromagnetic waves to penetrate the surface in order to create images of the shallow subsurfaces. Usually, these radars operates in the frequency range between 25 MHz to 1000 MHz [27]. The basic system architecture is shown in Figure 2.10. The system consists of

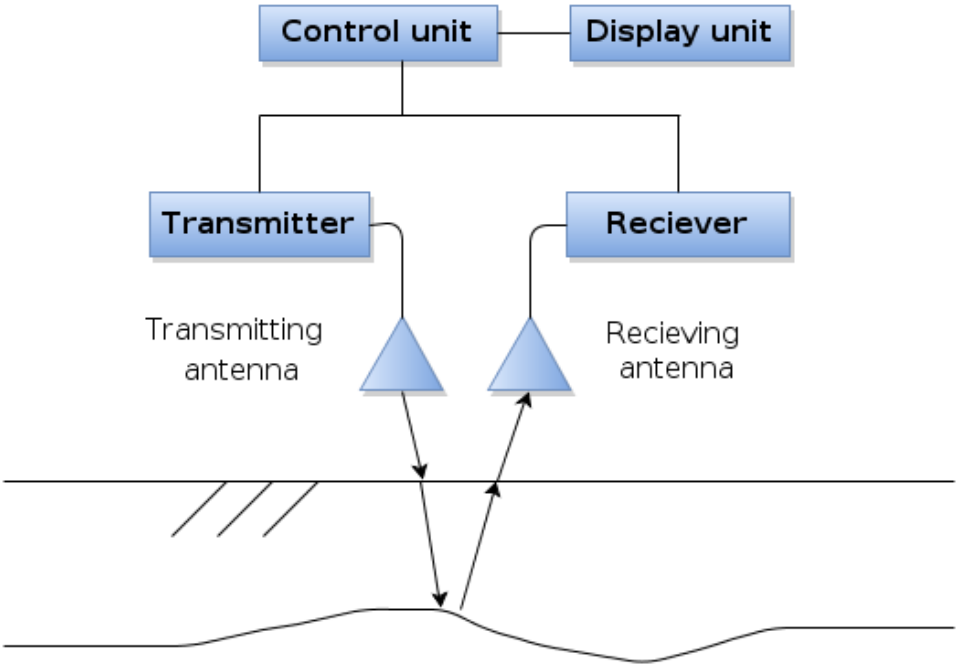

Figure 2.10: Brief system overviw of GPR system.

an transmit- and receive antenna, and a control unit for data handling. The transmit and receive antennas are usually equally designed and need to be characterized to fit the desired waveform. [19].

Most GPRs measures the backscatter signal from the target to create images of the ground. The backscattered signal undergoes various losses in the propagation path back to the receiver. The total path loss for a particular distance is given by

$$L_T = L_e + L_m + L_{t1} + L_{t2} + L_s + L_a + L_{sc} \tag{2.24}$$

where: L_e = antenna efficiency loss in dB
L_m = antenna mismatch losses in dB
L_{t1} = transmission loss from air to material in dB
L_{t2} = retransmission loss from material to air in dB
L_s = antenna spreading losses in dB
L_a = attenuation loss of material in dB
L_{sc} = target scattering loss in dB

To get a accurate prediction of the losses, this calculation has to be performed for the frequencies of interest. Equations for calculating the different losses can be found in the literature [19].

Depth measurement using GPR

The dielectric properties of the medium is often unknown. Therefore, for a practical measurement, the velocity has to be estimated by means of multiple measurements. Figure 2.11 shows one example of a common depth point estimation. By moving the transmit and receive antennas in equal distance from the common midpoint, it is possible to obtain the same apparent reflection position [19]. Then, the distance

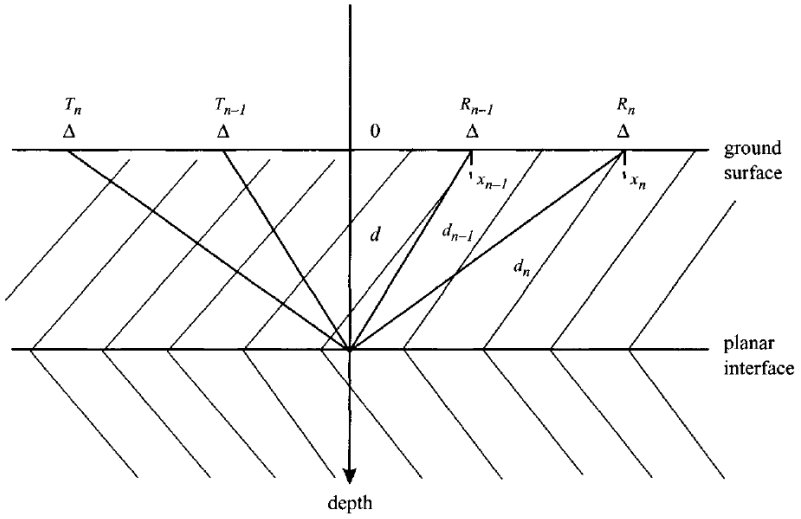

Figure 2.11: The common depth point estimation illustrated, from [19].

can be calculated using the following expression

$$d_n = \sqrt{\frac{x_{n-1}^2 t_n^2 - x_n^2 t_{n-1}^2}{t_{n-1}^2 - t_n^2}} \tag{2.25}$$

This is especially important in snow analysis, where the dielectric properties of the snow may be unknown for the individual layers. In section *2.1.2 Dielectric properties of materials* it was shown that the dielectric properties of snow was different depending on the condition of the snow. Dry snow had low dielectric losses, while wet snow suffered from high losses.

The dielectric properties of different layers in the ground soil is much higher than for snow. Depending on the condition of the soil, it may vary between 4 to 30 in relative permittivity [28]. The need for a radar system operating in the MHz range is therefor desirable in order to penetrate the ground. For snow imaging, the dielectric properties are much less, and the radar system may therefore increase the frequency of operation.

Snow penetrating radars

SPRs works much in the same way as a GPR. The difference lays in the potential usage of the frequency of operation, as was discussed above. Imaging and measuring depth of glaciers was one of the first applications where SPRs were used. Since the ice almost has a constant permittivity as a function of temperature (approximately 3.2), it is easy for the electromagnetic waves to penetrate the glacier [29]. Most of the work related to snow and ice is related to glaciers and not so much regarding snow profile imaging with respect to snow avalanches.

The radar intended for snow imaging applications is the Novelda X2 radar module [4]. The radar operates in the range 4 GHz to 12 GHz with a adjustable center frequency between 5.3 GHz and 8.8 GHz. A special model of this radar, called the Ventricoder is adjusted down in the frequency band to 2.5 GHz to 5.5 GHz with a center frequency of approximately 3.9 GHz. With a accuracy of approximately 1 mm, the radar seams to be promising for snow imaging applications. Figure 2.12 shows a picture of the Ventricorder module that has been used.

Figure 2.12: Picture of the Ventricorder radar module.

2.3 Directional UWB Antennas for snow imaging

As has been discussed in the previous sections, it is desirable to have a large signal bandwidth in order to get a good resolution for the SPR image. To accomplish this, the transmit and receive antennas needs to have sufficient bandwidth to meet this requirement. An antenna having a narrow bandwidth will result in oscillations and stretching of the propagating signal.

In addition to an antenna having a large bandwidth, it is important to have a large gain and narrow beamwidth. For snow imaging applications, this is essential for getting reliable measurements. As the signal is propagating down into the snow, the receive antenna will pick up reflections from each snow-layer. If the antenna has a wide beamwidth, the receive antenna will pick up multiple reflections from multiple layers at the same time. It will therefore be difficult to distinguish between the different layers. Having a narrow beamwidth (ideally as the beam of a laser), the receive antenna will see reflections from the different layers at different times. This makes it easier to distinguish between the different layers.

For remote Geo-Sensing applications like SAR or RAR imaging, it is essential to have a radar system that is mobile and easy to carry out in the field. A large radar system would be impractical for many applications, especially avalanche detection where measuring the mountain side with slopes steeper than 30° is the critical part. Weight and size is two important considerations that needs to be evaluated along with the gain and bandwidth requirements.

During the past years, 3D printed antennas has shown to be a promising technology regarding light weighted antennas [30] [31]. These antennas are printed in low cost plastic (PLA) and coated with copper spray, or electroplated to make the surface conductive. In this section, a selection of different high gain, ultra-wideband (UWB) antennas will be shown, in addition to a discussion of the weight and size with respect to the intended application.

2.3.1 Reflector antennas

Reflector antennas was first introduced by Heinrich Hertz (1857 - 1894) in 1887. The reflector antenna, or parabolic antennas are known to most people and are often used for television signals, wireless LAN, satellite communication and as radar antennas. These antennas are popular for end to end applications where high gain is desired [32]. Reflector antennas are categorized into the main classes; planar reflectors, corner reflectors and parabolic cylinder reflectors are some of them. In this section, only the parabolic reflector will be examined because of its high gain and relatively large bandwidth [33].

Parabolic reflector antenna

Parabolic reflector antennas can be designed for very high gain (in the order 30 dBi). The focal length of a reflector antenna determines the dimensions. If the vertex lies at the origin and the parabola is oriented towards the positive y-axis with

a focal point at $y = p$, the equation for the parabola is

$$y = \frac{1}{4p}x^2 \tag{2.26}$$

This can be seen in Figure 2.13. Circular reflector antennas can be designed in

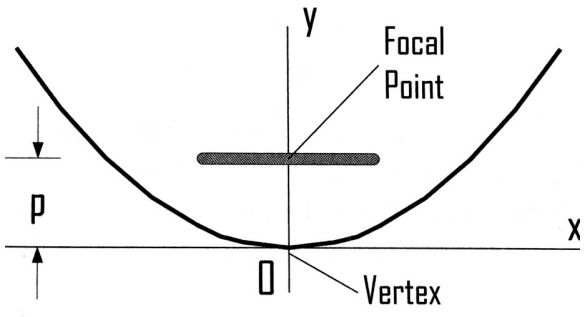

Figure 2.13: Reflector antenna focal point, from [33, pp. 477]

two ways; compact or large. A compact reflector antenna is designed for relatively high gain but it suffers from some mismatch due to reflections back to the source. A large circular reflector is designed for high gain. However, since the gain of an

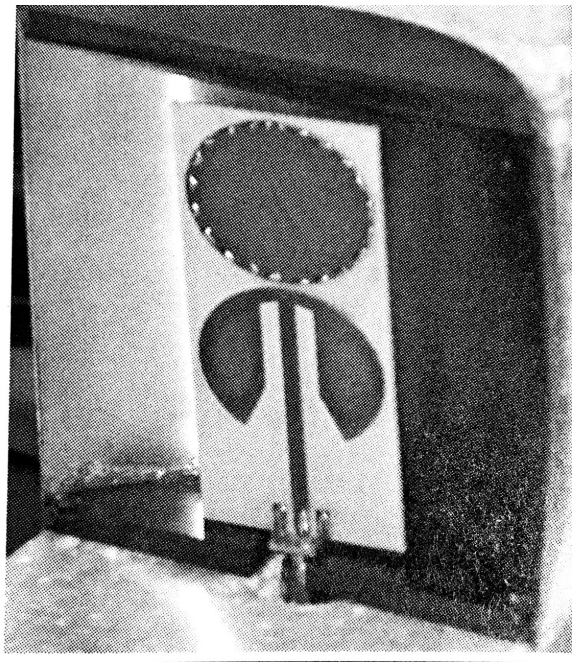

Figure 2.14: Planar dipole antenna as feed for a parabolic reflector antenna, from [33, pp. 477]

antenna is a function of the aperture (Eq. (2.23)), these antennas tends to be quite large. Figure 2.14 shows an image of a parabolic reflector antenna with a planar dipole feed in the middle. In Figure 2.15 (a), the gain of the presented antenna is compared to the planar dipole without the parabola. For the reflector antenna, a 9

dB gain is achieved, while for the planar dipole, a 3 dB gain is obtained. Adding a parabola therefore increases the gain of the antenna by 6 dB. Figure 2.15 (b) shows a plot of the reflection coefficient and VSWR for the same. It can be seen that the lower and upper bandwidth is approximately 3.3 GHz to 5.6 GHz.

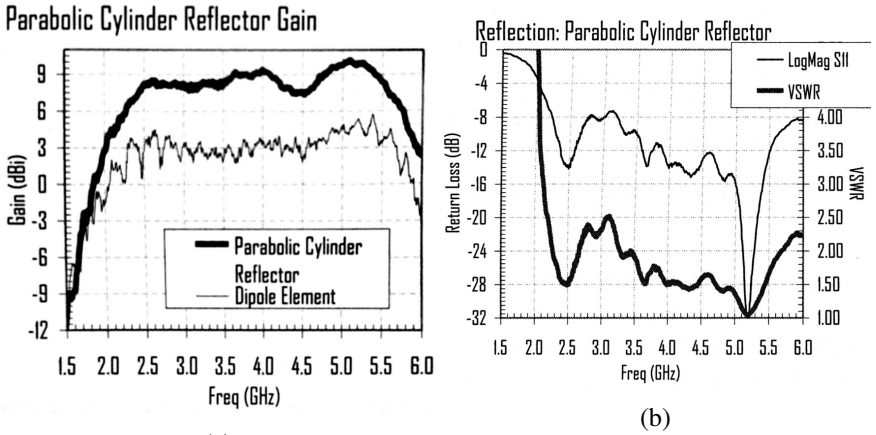

(a) (b)

Figure 2.15: (a) showing the gain for a single planar dipole antenna compared to a planar dipole used together with parabolic reflector antenna. (b) showing the reflection coefficient and VSWR for the same antenna. From [33, pp. 477]

Using a parabolic reflector antenna for snow imaging could be a potential antenna of choice. However, for a relative high gain, the antenna would be quite big. This would have resulted in a relatively heavy antenna it would have been manufactured in metal. Also 3D printing a large antenna would (depending on the printer size) potentially require many separated parts which would be quite difficult to design.

2.3.2 Microstrip array antennas

Microstrip patch antennas with traditional shapes as rectangular, quadratic, circular, triangular or other, tends to have a narrow bandwidth, often less than 5% if the substrate are relatively thin. However, with technology advancement, bandwidth in the order of 50% may be achievable for these simple geometrical antennas [34]. One other option is to make the antenna frequency independent. Frequency independent antennas have the advantage of a very wide bandwidth, often in the order of several decades. The bandwidth limitation is due to the physical scaling of the antenna. The disadvantage of these types of antennas is due to the scaling which gives rise to dispersion [33, pp. 364]. In addition, these antennas tends to have a relatively low gain, which makes them less suitable for snow imaging applications.

One possible option would be to make arrays of microstrip patch antennas. Large arrays can achieve very high gain, often in the order of 20 dBi or more [35]. However these antennas often suffer from narrow bandwidth due to mutual coupling between the array elements. In the recent years, lots of effort has been put into the study of making patch arrays more wide-banded, while keeping a relatively high

gain. It was observed that if a bandwidth of 10:1 was to be achieved, the maximum area of the unit cell has to be no longer than 0.05 times the wavelength at the lowest frequency. If the radiating elements exceeded 0.5 wavelength, grating lobes and surface waves starts to appear in the frequency band. One type of patch antenna that offer high gain and wide bandwidth is the *current sheet array*, which will be discussed in the next sub-section [36].

Current sheet antenna array

In 1999, Harris Corporation together with Dr. Ben Munk developed the first current sheet antenna array (CSA) based on a requirement of a 9:1 bandwidth antenna array targeted for 2 - 18 GHz operation. Harris and Muck discovered that a closely spaced overlapping dipole array exhibits a wide bandwidth when employed as an frequency selective surface (FSS) antenna. Due to the overlap capacitance between the elements, an array of dipoles with a small elements spacing above the ground plane could achieve a relatively high bandwidth. In order to extend this theory to obtain a even wider bandwidth, Harris and Munk discovered that by adding a dielectric layer on top of the dipole arrays, one would obtain an even wider bandwidth. The results showed that for a VSWR of 2:1, a bandwidth of 7:1 was obtained [36].

Figure 2.16 (a) shows an image of a CSA patented by Munk and Harris [37]. The image shows an early stage of the CSA with a 12-in x 18-in array. The interdigital capacitors shown in Figure 2.16 (b) ensures capacitive coupling between the elements [37]. In a later development, a 22-in x 22-in dual-polarized array was

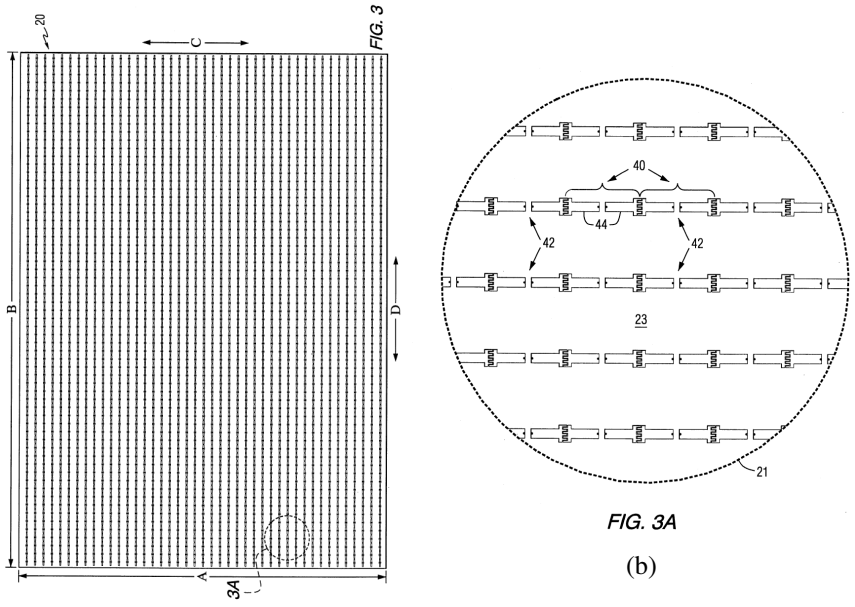

(a) (b)

Figure 2.16: (a) showing the antenna array for a current sheet array (CSA), and (b) showing the interdigital capacitors. From [37]

created to meet the original requirement for a bandwidth between 2 to 18 GHz.

The array consisted of 2664 elements, of which only 64 dual-polarized elements located at the center of the array are connectorized. The remaining elements are terminated by a 100Ω resistor. The measured gain for the 8 x 8 array was in the range 5 to 22 dB, as can be seen in Figure 2.17 [36].

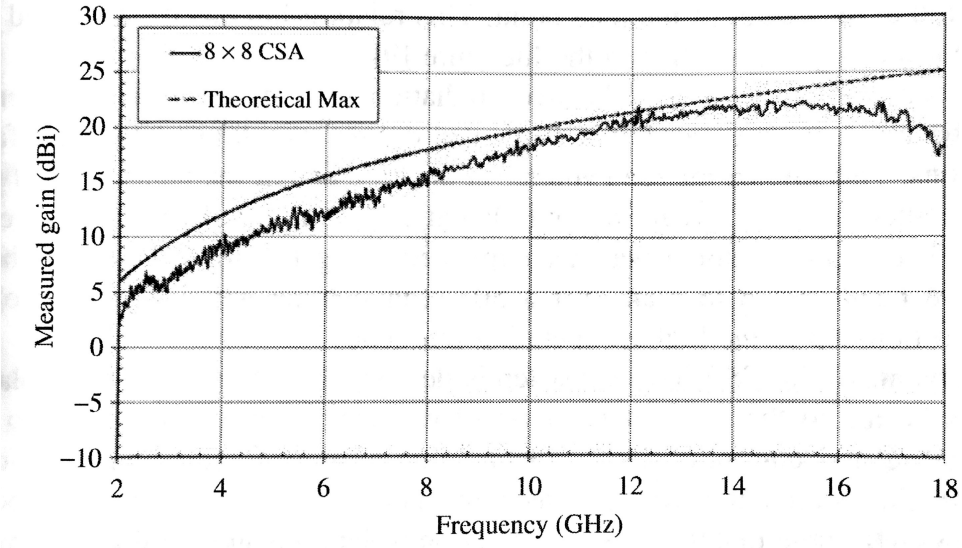

Figure 2.17: Gain obtained by the 8 x 8 CSA, from [36]

Summary of array antennas

The current sheet array is one example of an array antenna offering high gain and large bandwidth. Other antennas like the *Vivaldi antenna arrays* or *fragmented array antennas* can be used for the same types of applications. However, these antennas will not be discussed further in this thesis, but can be found in the literature [36]. Common for all of these antennas, besides the high gain and wide bandwidth, is the relatively large size. For snow imaging applications, these types of antennas would not be preferred. Also, designing these antennas are quite time consuming because the arrays needs to be carefully designed in order to minimize the mutual coupling between the elements.

2.3.3 Horn antennas

Since the first horn antenna was developed by Jagdis Chandra Bose (1858 - 1937) in the 1890's, it has been the preferred choice for applications requiring relatively high gain. Figure 2.18 shows a test setup created by Bose, demonstrating the use of horn antennas for transmitting signals between a transmit and receive antenna. In the middle, a dual-prism is used as attenuator [38].

As the antennas design in the late 1800 was designed for relatively low frequencies having large wavelengths, horn antennas would have been impractical to use. It wasn't until the 1930's that the horn antennas were suitable for RF applications, as the RF technology started to increase rapidly. For a proper use of the horn,

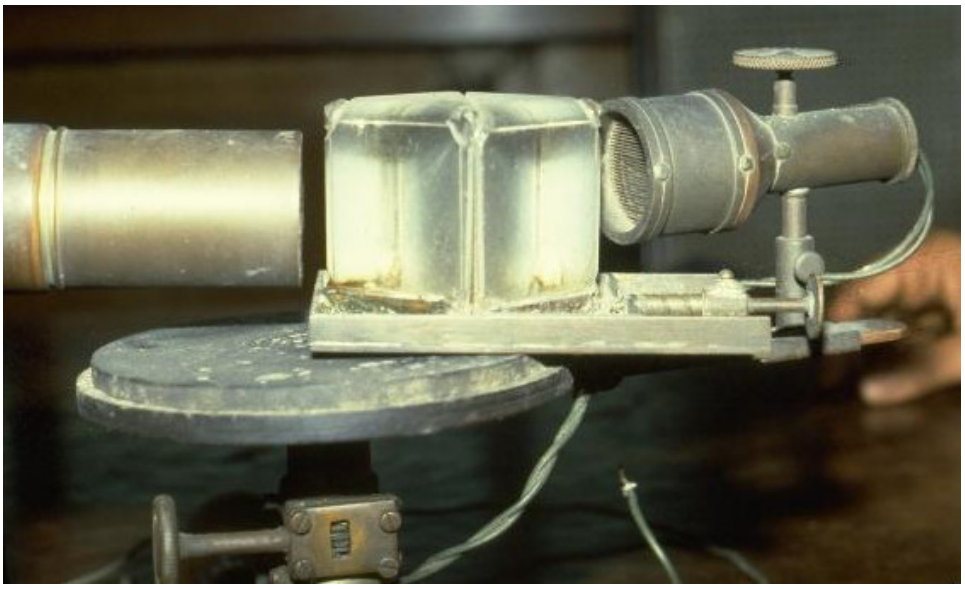

Figure 2.18: The figure is showing a test setup using one of the first invented horn antennas created by J. C. Bose in the 1890's. The transmit antenna can be seen to the left, while the receive antenna is to the right. From [38].

the length of the antenna is almost a wavelength long, resulting in large apertures which leads to directional antennas with relatively high gains. Lots of research has been developed for these types of antennas. In 1937, Wilmer L. Barrow (1903 - 1973) and Len Jen Chu (1913 -1973) described the physics of the horn antenna, and Schelkunoff and Friis has developed excellent equations for horn design calculations [33] [39].

The horn antenna acts as a flared or tapered transmission line designed to transmit and receive electromagnetic waves. Besides of having a relatively high gain, these antennas tend to have a narrow bandwidth. In order to increase the bandwidth, one can add a tapered ridged waveguide which lowers the cut-off frequency of the dominant mode, and increase the cut-off frequency for the next dominant mode [33]. A good selection of these types of horn antennas exists on the market. Figure 2.19 shows a typical double ridged waveguide horn antenna. The aperture size is 15.9 cm x 24.2 cm and the length is 27.9 cm. The antenna is designed for a bandwidth between 750 MHz and 18 GHz. At 750 MHz the gain is about 2.6 dBi, but at 1 GHz it reaches approximately 7 dBi. Between 3 GHz and up to 8 GHz, the antenna has a almost linear gain between 10 dBi and 12 dBi. The antenna is matched with an maximum VSWR of 5:1, but typically in the range 2:1 above 800 MHz [40]. Typical half-power beamwidth (HPBW) are 30-40° in the H-plane, and 45° in the E-plane [33].

For snow imaging purposes, it is desirable to have a almost linear gain over the entire frequency band. It was shown in Figure 2.15 (a) for the parabolic reflector that the gain was close to flat over a band between 2.5 GHz to 5.5 GHz. This is not the case for the double ridge waveguide horn that was described. This charac-

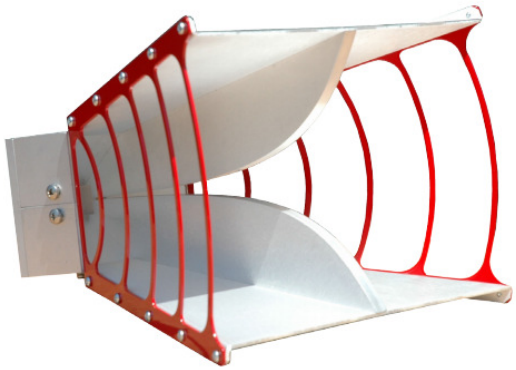

Figure 2.19: A standard double ridge waveguide horn antenna designed for high bandwidth and high gain. From [40]

teristics of the gain of these antennas is common for double ridged horn antennas. Therefore, for snow imaging purposes, these antennas are not well suited.

Also, a horn antenna with the same size as the one presented, has a typical weight of 1.5 Kg. Using one antenna for transmitting signals and one for receiving, the total weight would be around 3 Kg. For remote Geo-Sensing, this would not be a particularly practical system. However, the difference between a parabolic reflector and a horn antenna designed for the same gain requirements, is the size. The horn has a smaller aperture size, which makes it suitable for 3D printing.

Based on the discussion of high gain UWB antennas for snow imaging, it is reasonable to believe that the horn antenna would be the best choice regarding bandwidth requirements, high gain and the potential simplicity in design and manufacturing. In the next section, a more detailed discussion of the design of rectangular and double ridge horn antenna will be discussed.

2.4 Horn antenna parameters

A quick history and a example of the performance of the horn antenna was given in the previous section. The purpose of this section is to give the reader a detailed discussion of the design procedures and parameters obtained to create a rectangular horn antenna. A traditional rectangular horn antenna is divided intro three main parts; feed, waveguide and horn aperture. Each of these parts will be discussed in this section stating with the waveguide. Then the feeding technique of rectangular waveguides will be discussed, followed by the design parameters for a rectangular horn antenna.

2.4.1 Waveguide design parameters

A waveguide is an transmission medium for effectively transmitting electromagnetic signals from one point to another. Waveguides can have many shapes. Figure 2.20 shows a variety of different waveguides. In this thesis, three of these types will be used; coaxial line, microstrip line and rectangular waveguide. The purpose of this section is to give the reader an overview of the different design parameters given for these three waveguide types. First, the coaxial line will roughly be explained

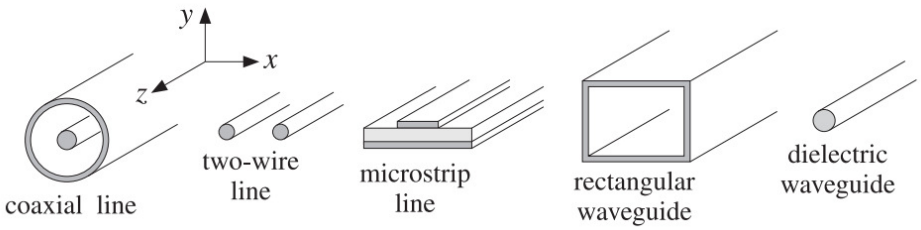

Figure 2.20: Typical waveguide structures, from [41, pp. 361].

followed by the microstrip line. The main focus is on the rectangular waveguide, as it is to be used together with the rectangular horn.

Coaxial lines

Coaxial lines consist of a inner conductor, a dielectric material and a outer conductor, as can be seen in Figure 2.20. Often, coaxial cables are designed to match 50Ω, but 75Ω and 100Ω also exists. The following equation is used to calculate the characteristic impedance of a coaxial cable [42]

$$Z_0 = \sqrt{\frac{L}{C}} = \frac{138}{\sqrt{\mu_r \varepsilon_r}} log\left(\frac{b}{a}\right) \tag{2.27}$$

where: L = inductance between the inner and outer conductor
C = capacitance between the inner and outer conductor
138 = a given constant
b = diameter of the outer conductor
a = diameter of the inner conductor.

Microstrip lines

A PCB transmission line can have many shapes and forms. In this thesis, only equations for the microstrip transmission line will be given. Other types can be found in literature [33, pp. 140]. The microstrip line is a single strip-line on one side of a PCB with a ground plane on the other side, separated by a dielectric. The equations for the characteristic impedance is a function of the height of the substrate, width of the trace and the dielectric constant for the substrate, given as

$$Z_0 = \frac{120\pi}{\sqrt{\varepsilon_{eff}} \cdot \left[\frac{W}{H} + 1.393 + \frac{2}{3} ln\left(\frac{W}{H} + 1.444\right)\right]} \tag{2.28}$$

where: ε_{eff} = effective dielectric constant
W = width of the strip line
H = height of the substrate

the effective dielectric constant is given by

$$\varepsilon_{eff} = \frac{\varepsilon_r + 1}{2} + \frac{\varepsilon_r - 1}{2}\left(1 + 12\left(\frac{H}{W}\right)\right]^{-1/2} \tag{2.29}$$

where: ε_r = relative dielectric constant

Rectangular waveguides

Designing a rectangular waveguide is mainly based on the requirements for the center- and cutoff frequency for the system. The general equation for the cut-off frequency are given as

$$f_c = \frac{1}{2\sqrt{\varepsilon\mu}}\sqrt{\left(\frac{m}{a}\right)^2 + \left(\frac{n}{b}\right)^2}, \tag{2.30}$$

where: ε = dielectric constant
μ = permeability constant
a = width of the waveguide
b = height of the waveguide
m, n = integers defining number of half-wavelengths that will fit in a and b dimensions, respectively.

The integers m, and n is determined by the selection of the propagation mode. Rectangular waveguides support different propagation modes. These are called the *transverse electric* mode and *transverse magnetic* mode, denoted TE_{mn} and TM_{mn}. The index m indicates the number of half-wavelength variations in the width of the waveguide (a), and the index n is the number of half-wavelength variations in the height (b). Figure 2.21 (a) shows an image of one single mode propagating in the rectangular waveguide. For this mode, the electric (green) and magnetic (blue) field are perpendicular to each other. Figure 2.21 (b) shows two propagating modes. In

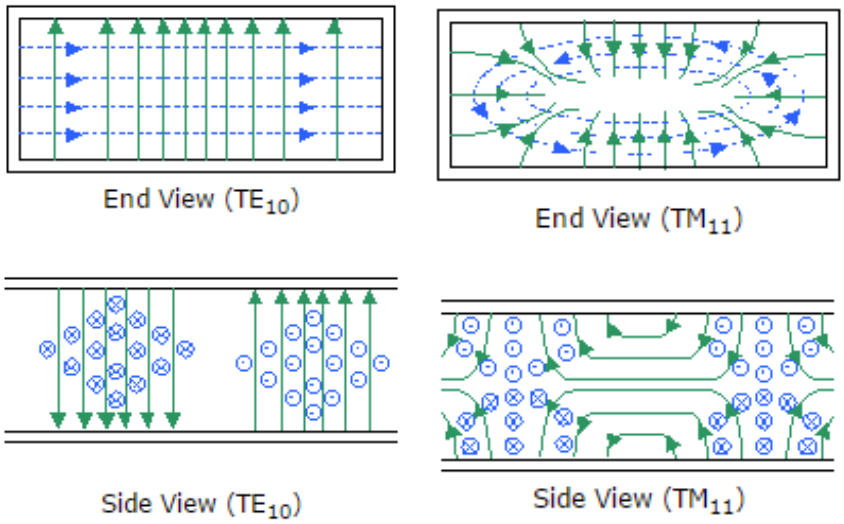

Figure 2.21: (a) showing one single propagating mode, and (b) showing two propagating modes. From [43]

this thesis, only modes propagating in the TE_{10} mode is considered. Therefore, Eq. (2.30) can be expressed as

$$f_c = \frac{1}{2a\sqrt{\varepsilon\mu}}. \tag{2.31}$$

The most common way to express the cut-off wavelength for a waveguide is by the following expression

$$\lambda_c = \frac{2}{\sqrt{\left(\frac{m}{a}\right)^2 + \left(\frac{n}{b}\right)^2}}. \tag{2.32}$$

Of course, this is just another way to express the relation

$$\lambda_c = \frac{c}{f_c} \tag{2.33}$$

Inside the waveguide there is something called the guided-wavelength. The guided wavelength is the distance between two equal phases along the waveguide section, and is expresses by the cut-off frequency and the center frequency in the following relation.

$$\lambda_g = \frac{\lambda_0}{\sqrt{1 - \left(\frac{f_c}{f}\right)^2}}, \tag{2.34}$$

where: λ_g = wavelength in waveguide
λ_0 = wavelength in free space
f_c = waveguide cut-off frequency
f = operating frequency.

Using all of this equations, one can calculate the dimensions for the waveguide based on the cut-off frequency and the center frequency.

Ridged rectangular waveguides

Traditional rectangular waveguides as the one expressed above, tends to have a narrow bandwidth. To increase the bandwidth, one can add ridges. The function of the ridges is to lower the dominant mode cut-off frequency, and increase the next dominant mode cut-off frequency. Ridging can be either single-sided or double-sided, depending on the application. In this section, the general equations for determining the gap between two single-sided ridges will be shown.

The early study of ridged waveguides was performed by Walton and Sundberg in 1964 [44], but is also well documented in [45]. Here, basic equations for calculating the capacitance between two ridges inside a waveguide are presented. The cross section of a single-sided and double-sided waveguide, together with the equivalent circuit, can be seen in Figure 2.22. The gap between the two ridges,

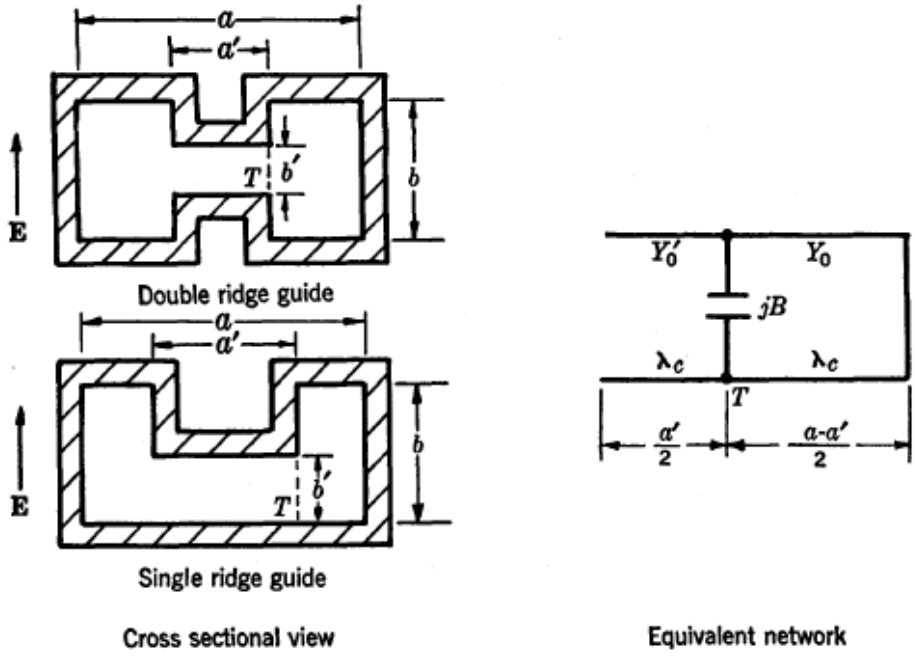

Figure 2.22: Single and double sided ridged waveguide and equivalent circuit, from [45].

are represented by a capacitor, as can be seen from the equivalent circuit. The propagating wavelength for a ridged waveguide is represented by the resonance conditions (at the reference plane T) as

$$\frac{Y_0'}{Y_0} tan \frac{\pi}{\lambda_c} a' + \frac{B}{Y_0} - cot \frac{\pi}{\lambda_c}(a - a') = 0 \tag{2.35}$$

where

$$\frac{Y_0'}{Y_0} = \frac{b}{b'} \tag{2.36}$$

These are the fundamental equations for calculating the dominant mode cut-off wavelength for a ridged waveguide. More about the equations can be found in the literature [45, pp. 399-402]

2.4.2 Feeding techniques for rectangular waveguides

Feeding a rectangular waveguide is traditionally done by probing a coaxial stub a quarter of a wavelength down into the waveguide. More on this technique and other is explained in a later chapter.

2.4.3 Horn design parameters

As has been discussed, horn antennas can be designed for a large gain, often more than 12 dBi. Figure 2.23 shows the typical design parameters for a standard rectangular horn antenna. The equations for calculating the dimensions of the horn

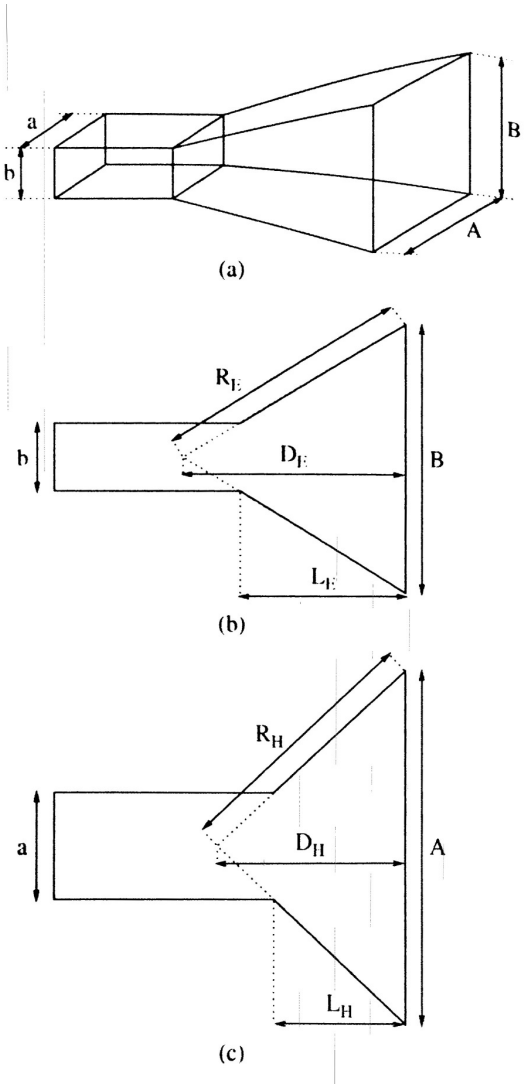

Figure 2.23: Typical horn shape. (a) showing a 3D model of the horn shape, (b) shows a cross section of the side and (c) shows the cross section from the top. from [46, pp. 101].

is based on the desired gain and the size of the waveguide. The following equations

is given as [46, pp. 118-119]

$$G_l = 10^{G_{dBi}/10} \tag{2.37}$$

$$A = 0.096aG_l^{0.232} + 0.42\lambda G_l^{0.503} - 0.193b \tag{2.38}$$

$$R_H = A\sqrt{\frac{1}{A} + \left(\frac{A}{3\lambda}\right)^2} \tag{2.39}$$

$$L_H = (A-a)\sqrt{\left(\frac{R_H}{A}\right)^2 - \frac{1}{4}} \tag{2.40}$$

$$D_H = \sqrt{R_H^2 - \left(\frac{A}{2}\right)^2} \tag{2.41}$$

$$B = \frac{1}{2}\left[b + \sqrt{b^2} + 8L_H\lambda\right] \tag{2.42}$$

$$R_E = \frac{B}{2}\sqrt{1 + \left(\frac{B}{\lambda}\right)^2} \tag{2.43}$$

$$L_E = (B-b)\sqrt{\left(\frac{R_B}{B}\right)^2 - \frac{1}{4}} \tag{2.44}$$

$$D_E = \sqrt{R_E^2 - \left(\frac{B}{2}\right)^2}. \tag{2.45}$$

2.4.4 Summary of horn antenna parameters

This section gives a brief overview over the basic design parameters for designing a rectangular horn antenna and a ridged waveguide. Designing a rectangular horn is quite straight forward if the center frequency, cut-off frequency and gain is known. Designing a ridged waveguide is more challenging if the design equations are to be used. For this particular design, a more methodical design approach would probably more preferred for time saving.

2.5 System overview

The main goal in this thesis is to create an ultra-wideband (UWB) 3D printed antenna suitable for snow imaging purposes. Such a system requires specific specifications for the bandwidth considering resolution and the performance of the Novelda radar module. In addition, high gain over the entire bandwidth is desirable so that the antenna does not receive unwanted backscattered signal from multiple layers at the same time. Also, requirements for the antenna size is important in order to get a mobile and robust radar system. However, it is important to notice that this will only be a prototype and no commercial product. In this section, the system requirements will be discussed.

2.5.1 Antenna parameters

Gain

To get reliable data from the snow measurements, it is important to have a directive antenna with a narrow beam. Discussed earlier, a high directivity is needed to minimize the backscattered signals from unwanted layers. Assuming homogeneous and equally spaced snow layers, the transmitted waves propagate spherical down into the snow pack. If the beam is wide, backscattered signals from layers fare out to the side will hit the antenna at the same time as for example the next layer. This will make it impossible for the radar system to separate the unwanted and wanted reflection. Therefore, a very directive antenna is needed to minimize unwanted reflections. Directionality and gain is the same for a 100% effective antenna. Therefore, a high gain in the order of 15 dBi to 20 dBi is decried.

Polarization

There are no requirements for the polarization in this thesis. However, as the selection of the antenna is to be a rectangular horn, it is in general not desired to have cross polarization. Therefore the antenna should be linear polarized.

Frequency range and bandwidth

The requirements for the bandwidth is more restricted. To radiate the pulse generated by the Novelda X2 radar, it is desirable to have a bandwidth of approximately 3 GHz in the 2.5 GH to 5.5 GHz. The center frequency is approximately 3.9 GHz, so designing for a center frequency of 4 GHz will work.

Also, as was discussed in section *2.1.3 Resolution*, the downrange resolution is a function of the bandwidth. In order to get detailed images of the snow profile, a high bandwidth is needed.

2.5.2 Practical usage

This sub-section is more related to the practical usage of the antennas and the radar system, discussing the antenna size and practical challenges.

Antenna size

The antenna size is not limited by the requirements. However, the antennas should be designed not to be too big, so that they would be impractical to carry out in the field. Since the size and the gain is related, horn antennas can be extremely large if a very high gain is needed. Therefore, it will be important to discuss the trade-offs of a high gain and large size.

Portable and robust radar system

Taking the radar out in the field requires some additional hardware design for robustness against the weather. Also the practical usage needs to be considered. For SAR or RAR imaging, it will be impractical to bring a lab setup out in the field. Therefore, a suitable portable system needs to be created.

2.5.3 Design specification overview

A summary of the specifications is given below.

- Gain: 15 dBi - 20 dBi
- Bandwidth: 3 GHz
- Frequency band: 2.5 GHz - 5.5 GHz
- Impedance matching level: $|S_{11}| < -10\text{dB}$
- Polarization: linear polarized
- Antenna size: Suitable for hand-held applications

Chapter 3

Design and analysis

In this chapter, the design steps for a horn antenna will be described in detail based on the requirements discussed in the previous chapter. Based on the provided theory, the horn was found to be the best suited antenna for snow imaging purposes. This is based on the properties for the horn antenna and the physical challenges for manufacturing the antenna using additive manufacturing techniques (3D printing). This chapters starts be describing the methods that has been used during the design process. In the second section, the design steps for creating a standard rectangular horn antenna based on design equations given in the literature will be discusses. The next section describes two different design approaches for making the antenna more wide-banded. In the forth section, a new technique for feeding 3D printed plastic structures will be examined and the fifth section shows a relatively new design approach for making a high gain, ultra wide-banded antenna. The last section explains the design process and possible challenges for 3D printed antennas.

3.1 Design method

All antenna simulations has been performed using Ansys High Frequency Structural Simulator (HFSS). HFSS is a professional CAD-modeling EM-simulation software used to simulate the performance of antennas and other RF-parts. The software is based on Finite Element Method (FEM) which means that the model is meshed down into smaller structures where each of the structures are solved for Maxwell's equations. In the early beginning of the project, EMPro by Keysight was used for some antenna designs. As for all advanced softwares, EMPro missed some features that HFSS was more suited for. Therefore, it was decided to use HFSS instead. To create a 3D printed model of the designed antenna, a specific file formate is needed. Unfortunately, HFSS does not support this file format. Therefore, the 3D models have been exported to SolidWorks in order to create the right file formats for 3D printing.

The 3D printing has been performed at the University of Oslo, Department of Informatics, mostly at the ROBIN group but also at the NANO group. For the purpose, Ultimaker 2+/3 Extended has been used for creating the models. The models has been printed in polylactic acid (PLA), and some models has bin printed in VeroClear (discussed in Chapter 5).

3.2 Design of pyramidal horn antenna

In the following sections, design and discussions of the three main parts; waveguide, feed and horn aperture will be shown. Before determining the gain of the antenna and the size of the horn aperture, it is important to design a proper waveguide that works for the frequency of operation. After the waveguide has been designed and simulated, one can design the horn aperture.

3.2.1 Designing a waveguide for rectangular horn

The basic formulas for determining the cut-off frequency and the wavelength inside the waveguide was shown in Chapter 2. In this section, these equations are used to determine the dimensions for a rectangular waveguide. As seen in Eq. (2.30), the center frequency and the dimensions of the waveguide is dependent on the permittivity of the medium that the waveguide is designed for. As a good approximation, and for a simplified design, the waveguide will be characterized for air. In a later design, it should be characterized for the right material with the correct dielectric constant (for snow). In order to determine the dimensions for the waveguide, it is reasonable to start by defining a cut-off frequency which can be expressed by the dimensions for the waveguide given as

$$f_c = \frac{1}{2\sqrt{\varepsilon\mu}}\sqrt{\left(\frac{m}{a}\right)^2 + \left(\frac{n}{b}\right)^2}. \tag{3.1}$$

The dielectric constant (ε) is the sum of the permittivity in free space (ε_0) and the permittivity of the material relative to that of free space (ε_r). The permeability constant (μ) is the sum of the relative permeability (μ_0) and the permeability to a material (μ_r). In air ε_r and μ_r is both equal to one, resulting in $\varepsilon = \varepsilon_0$ and $\mu = \mu_0$ [47].

For the TE_{10} mode the width is larger than the hight of the waveguide, which can be seen in Figure 3.1. The index $m = 1$ and $n = 0$ means that only one mode is allowed to propagate in the electric field and none in the magnetic. Inserting values for m and n into Eq. (3.1), gives the simplified expression

$$f_c = \frac{1}{2a\sqrt{\varepsilon\mu}}. \tag{3.2}$$

By selecting a proper cut-off frequency the width of the waveguide can be calculated. Since the requirements for the bandwidth is in the region 2.5 GHz - 5.5 GHz, it is reasonable to set a cut-off frequency to $f_c = 2$ GHz, some lower than the minimum frequency. Rearranging Eq. (3.2), and inserting the cut-off frequency, it is found that the width of the waveguide is equal to $a = 74.95$ mm. A good approximation for the height of the waveguide is half the width, equal to $b = 37.47$ mm.

The length of the waveguide is generally not limited, and depend on the application. However, for a practical implementation it is reasonable to use a length of one wavelength, or equal to the width a.

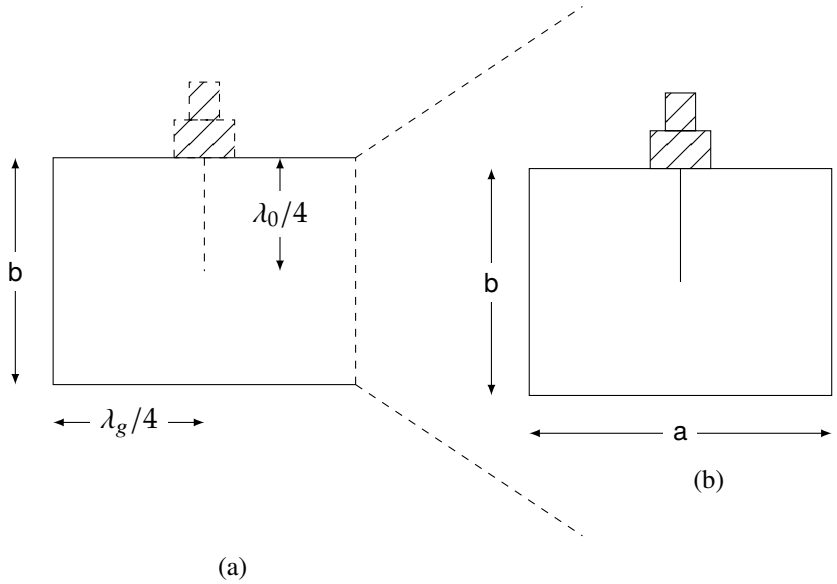

Figure 3.1: Standard waveguide feed. (a) cross section of waveguide side and, (b) cross section of waveguide front.

The cut-off wavelength can be expressed by the formula

$$\lambda_c = \frac{2}{\sqrt{\left(\frac{m}{a}\right)^2 + \left(\frac{n}{b}\right)^2}}. \tag{3.3}$$

Inserting the values into the expression, gives an cut-off wavelength equal to $\lambda_c = 150mm$.

Recalling the equations for the guided wavelength from Chapter 2

$$\lambda_g = \frac{\lambda_0}{\sqrt{1 - \left(\frac{f_c}{f}\right)^2}}, \tag{3.4}$$

and inserting the wavelength in free space (λ_0 = 75 mm), the cut-off frequency (2 GHz) and the center frequency (4 GHz), gives an guided wavelength of λ_g = 86.6mm [47].

3.2.2 Feeding a rectangular waveguide

Feeding a waveguide is traditionally accomplished by using a coaxial probe going through the waveguide wall and into the inside of the waveguide, as can be seen in Figure 3.1 [48].

The length of the probe and the distance between the probe and the cavity is normally $\lambda_0/4$ and $\lambda_g/4$, respectively, where λ_0 is the wavelength at 4 GHz and λ_g is the guided wavelength. Equations for calculating the dimensions for the coaxial cable has been given in Chapter 2. A handful of softwares and online tools exist for calculating dimensions of coaxial cables, transmission lines and waveguides. In

this thesis, AppCAD has been used for this purpose. Using a inner conductor with a diameter of $d = 1.2$ mm, a outer shield diameter of $D = 4.2$ mm and polyethylene with a dielectric constant of $\varepsilon_r = 2.25$, a characteristic impedance of $Z_0 = 50.68\Omega$ is obtained.

3.2.3 Simulation of rectangular waveguide

The waveguide model can be seen in Figure 3.2. The dimensions has been calculated in previous sections, and is also displayed in the figure.

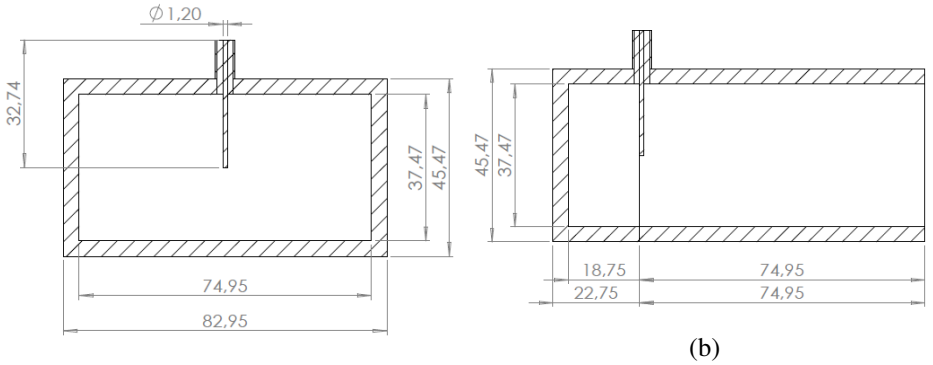

(a) (b)

Figure 3.2: Cross section of rectangular waveguide. (a) cross section of waveguide front and, (b) cross section of waveguide side.

A plot of the reflection coefficient (S_{11}) and the transmitted signal (S_{21}) can be seen in Figure 3.3. The blue and orange curves shows the reflected signal and the transmitted signal respectively.

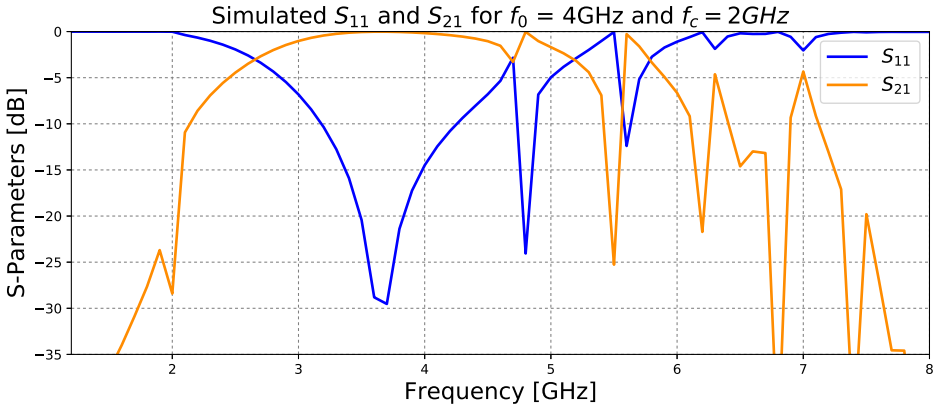

Figure 3.3: Plot of S_{11} and S_{21} for a rectangular waveguide.

As explained in Chapter 2, the bandwidth is determined by the point where the reflected signal is less than 10% of the transmitted signal, or -10 dB expressed in decibels. From the plot, it is shown that the frequency band of operation is between

3.2 GHz - 4.3 GHz, which gives an bandwidth of 1.1 GHz. It is also observed that S_{21} is approaching 0 dB within the band, which means that all the signal is transmitted through the waveguide. Around 4.8 GHz, it is observed a narrow band in which the waveguide is functional. These two bands however, does not meet the requirements for the bandwidth of 3 GHz within the band 2.5 GHz - 5.5 GHz.

Also in Chapter 2, it was seen that ridging the waveguide would increase the bandwidth of the system. This solution, along with one alternative solutions is discussed in a later sections. Even if the bandwidth of the waveguide does not meet the requirements, it is interesting to see whether the performance is the same when adding a horn aperture to the waveguide. This design approach is discussed in the next section.

3.2.4 Design of horn aperture

In the specifications, it is given that the antenna should have a gain of 15 to 20 dBi. The size of the antenna and the gain is proportional to each other. A general rule of thumb is that increasing the gain of 3 dB, doubles the size of the antenna. This means that increasing the gain from 15 to 20 dB, will increase the size significantly. Trade-off between the size and gain is therefore important to discuss.

As has been discussed several times before, the high gain is important so that the beam is as narrow as possible down to the snow. The importance of a narrow beam is illustrated in Figure 3.4. For simplicity, the transmit and receive antenna is illustrated as one single antenna. The figure shows three different cases. The

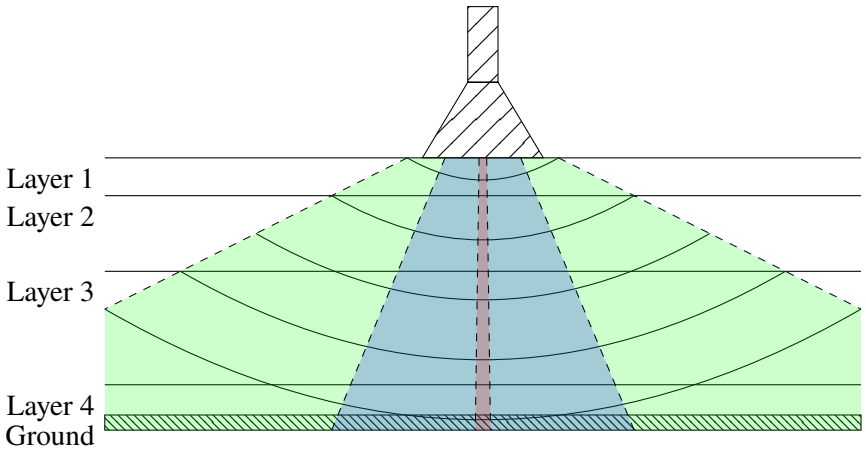

Figure 3.4: Radiating beam down to the snow.

first (green field) is an antenna with a low gain, i.e. wide beam. In this case, the receiving antenna will pick up scattered signals from distances far away from the antenna, as well as close to the antenna. These reflections will reflect from the same snow layer, but at different places which will result in a time delay. Because of this time delay, it will therefore be difficult to distinguish which layer the signal is scattered from. In the second case (blue field) it is shown an antenna with a higher gain. In this case, the receive antenna will pick up reflected signals from a narrower

view, which will result in less unwanted reflections. One can think of an ideal case where a laser is pointed down into the snow (red field). In this case, the antenna only experience reflections from one point in each layer at the time. The trade-off for such a narrow beam, is that it would be required an extremely large antenna.

To calculate the dimensions for a standard rectangular horn, equations given by [46] is used. Recalling these equations from Chapter 2 gives

$$G_l = 10^{G_{dBi}/10} \tag{3.5}$$

$$A = 0.096aG_l^{0.232} + 0.42\lambda G_l^{0.503} - 0.193b \tag{3.6}$$

$$R_H = A\sqrt{\frac{1}{A} + \left(\frac{A}{3\lambda}\right)^2} \tag{3.7}$$

$$L_H = (A-a)\sqrt{\left(\frac{R_H}{A}\right)^2 - \frac{1}{4}} \tag{3.8}$$

$$D_H = \sqrt{R_H^2 - \left(\frac{A}{2}\right)^2} \tag{3.9}$$

$$B = \frac{1}{2}\left[b + \sqrt{b^2} + 8L_H\lambda\right] \tag{3.10}$$

$$R_E = \frac{B}{2}\sqrt{1 + \left(\frac{B}{\lambda}\right)^2} \tag{3.11}$$

$$L_E = (B-b)\sqrt{\left(\frac{R_B}{B}\right)^2 - \frac{1}{4}} \tag{3.12}$$

$$D_E = \sqrt{R_E^2 - \left(\frac{B}{2}\right)^2}. \tag{3.13}$$

A gain of 15 dBi, gives an linear gain of $G_l = 31.62$, if the decibel value is inserted to Eq. (3.5). Using this linear gain in Eq. (3.6), one can calculate the width (A), height (B), and length (L_H or L_E) of the horn aperture. Inserting the gain of 15 dBi gives the following dimensions listed in Table 3.1. Also, dimensions for a 20 dBi gain antenna is included in the table. Comparing these sizes, it is clear that the size of an antenna with 20 dBi gain, is much larger than an 15 dBi antenna.

3.2.5 Simulation of rectangular horn antenna

The simulation of the rectangular horn antenna has been performed in Ansys HFSS. A 2D drawing including dimensions, and a 3D model of the antenna can be seen in Figure 3.5 and Figure 3.6, respectively. All of the three parts; waveguide, feed and horn aperture, has now been discussed and the dimensions has been determined. Now that all the three parts are implemented together, it is time to simulate the

	$G_{dBi} = 15dB$	$G_{dBi} = 20dB$
G_l	31.62	100
A	187.78 mm	333.09 mm
R_H	253.14 mm	758.19 mm
L_H	141.26 mm	573.24 mm
D_H	235.08 mm	739.67 mm
B	165.50 mm	312.57 mm
R_E	200.48 mm	669.81 mm
L_E	141.26 mm	573.24 mm
D_E	182.60 mm	651.33 mm

Table 3.1: Calculations of horn parameters for gain of 15 dBi and 20 dBi.

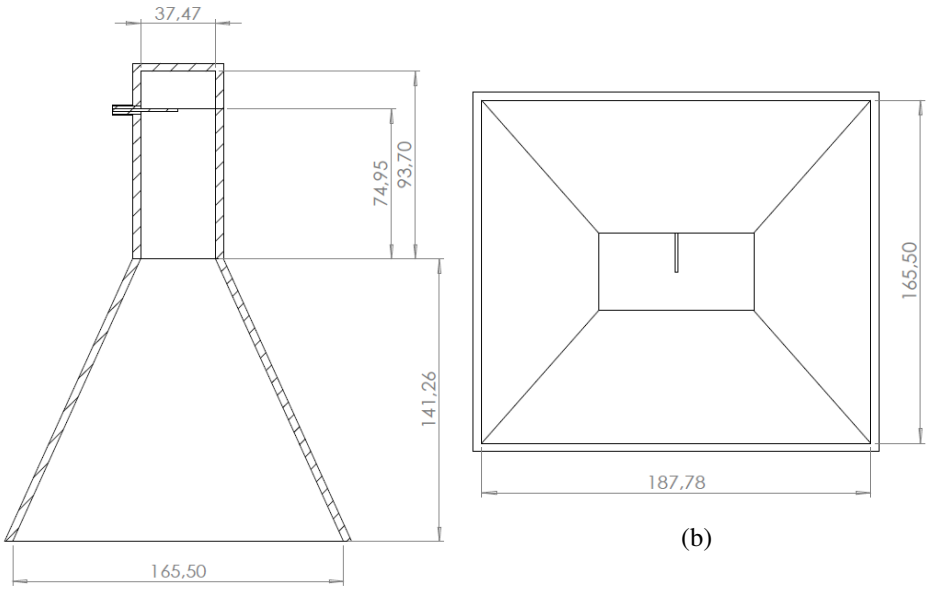

(a) (b)

Figure 3.5: Cross section of rectangular horn. (a) cross section of horn side and, (b) horn front.

behavior. For simplicity, perfect electrical conductor (PEC) is used on the surface of the model. PEC does not suffer from any losses, so the simulation will differ from the real performance.

A plot of the reflection coefficient can be seen in Figure 3.7. From the figure, it is shown that the bandwidth is within 3.2 GHz - 4.3 GHz, which gives a total bandwidth of 1.1 GHz. This was also achieved for the waveguide alone. This means that the horn aperture does not change the bandwidth of the system. This is good, because if a higher gain is needed, one can simply keep the waveguide and change the aperture. This is important regarding cost and 3D printing time.

The antenna gain is measured relative to an isotropic antenna, and is measured in

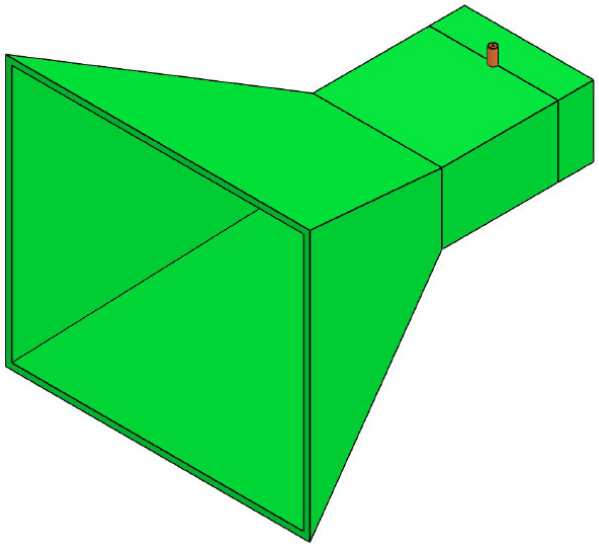

Figure 3.6: 3D model of the rectangular horn antenna.

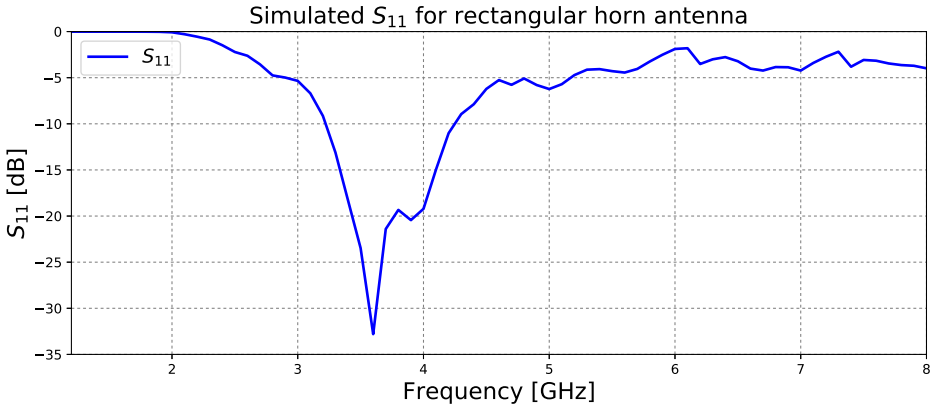

Figure 3.7: Plot of reflection coefficient, S_{11}.

the far-field. The gain is proportional to the directivity which is the antennas ability to concentrate RF signals in a subset of directions rather than all directions. For a horn antenna, the gain is proportional to the area of the flared open flange (A), and inverse proportional to the square of the wavelength. This simplified expression is given as [47]

$$G = \frac{10A}{\lambda^2}, \tag{3.14}$$

where: G = antenna gain
A = flange area
λ = wavelength.

It is expected that the gain will increase linearly according to Eq. (3.14). To see whether this is true, a plot of the gain versus the frequency can be seen in Figure 3.8. From the figure, it is shown that over the frequency-band, the gain is varying

from approximately 11 dB at 2 GHz to 17 dB at 4 GHz. Above 6 GHz, the gain starts to decrease significantly, but this is outside the frequency range of interest.

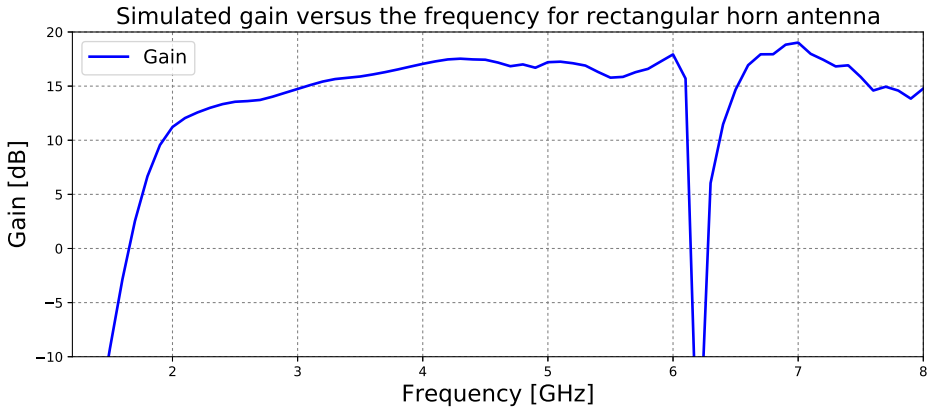

Figure 3.8: Plot of gain versus frequency for rectangular horn antenna. Gain at 4 GHz is approximately 17 dB.

The E- and H-plane directivity measured at 4 GHz can be seen in Figure 3.9. The half-power beamwidth (HPBW) is approximately 24° in the E-plane, and 26° in the H-plane. The front-to-back ratio was simulated to be approximately 27 dB.

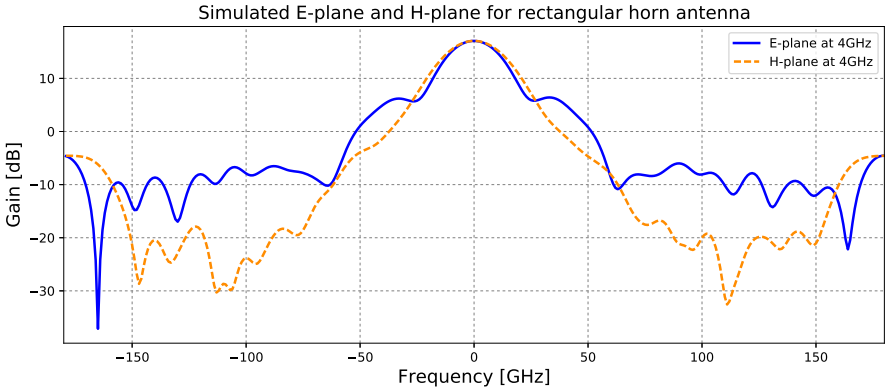

Figure 3.9: E- and H-plane directivity at 4 GHz showing a maximum directivity of $D_0 = 17.0dB$ with half-power beamwidth of approximately 24° and 26° in the E- and H- plane respectively.

3.2.6 Summary

In this section, a rectangular horn antenna has been designed for a center frequency of 4 GHz and a cut-off frequency of 2 GHz with a gain of 15 dBi. The simulated results shows that the requirements for a gain between 15 and 20 dBi is fulfilled, with a simulated gain of 17 dBi. This is somewhat higher than the calculated gain. It was also shown that the bandwidth of the system was unchanged by the horn aperture, which means that the waveguide can remain unchanged if a higher gain

is needed. However, the bandwidth does not meet the system requirements of 3 GHz bandwidth between 2.5 GHz to 5.5 GHz. Other techniques needs to be used in order to get a wider bandwidth. This is discussed in the next section.

3.3 Design of tapered double ridged horn antenna

One improvement for the bandwidth would be to add a ridges to the antenna. This is called a tapered double ridged horn antenna (DRHA), and can be customized for single polarization using double-ridged waveguide, or dual polarization using quad-ridged waveguide. The dual-ridged waveguide is well documented in [45] [49], and widely used for ultra-wideband applications covering a large specter of frequencies.

In this section, a single sided tapered ridged horn is designed and examined. The section starts by designing a ridged waveguide, followed by an discussion of the feed solution for a ridged waveguide. In the end of the section, the ridged waveguide is implemented together with a tapered ridged horn.

3.3.1 Design of ridged waveguide

Figure 3.10 shows a cross section of a double sided ridged waveguide. The most

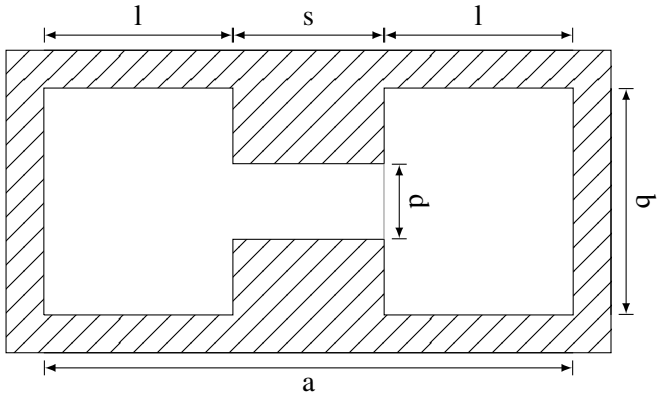

Figure 3.10: Model for a ridged waveguide including dimensions [49].

common way, and the one discussed in this thesis, is the double sided ridge which has been well documented by the early work from Walton and Sundberg [44]. The basic equations were given in Chapter 2 and are also documented in [45]. Solving these equations are quite complex, and probably not worth the effort. Instead, a more methodical approach has been used for determining the size of the ridges.

3.3.2 Feeding the ridged waveguide

Before simulations will be performed, the feeding of the ridged waveguide needs to be discussed. The feeding technique uses the same concept as for a regular waveguide. A coaxial stub is placed $\lambda_g/4$ away from the back of the cavity. The difference between the feeding of a ridged waveguide and a standard rectangular waveguide, is that the coaxial stub is connected to the lower ridge. Also, the coaxial stub needs to be isolated from the waveguide wall and the upper ridge. The coax-to-ridged-waveguide transition is illustrated in Figure 3.11.

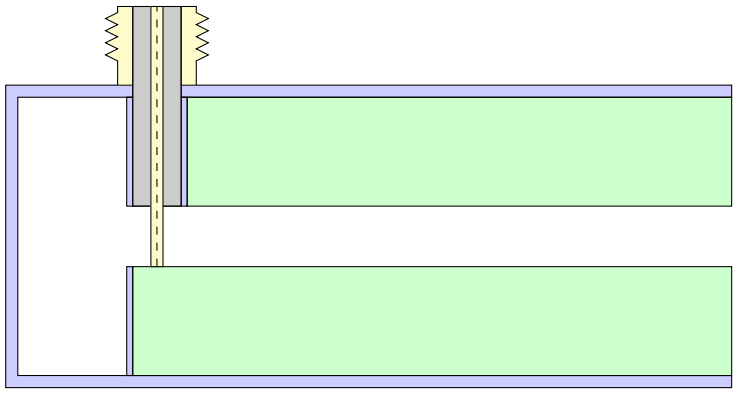

Figure 3.11: Cross section of coax to ridged waveguide transition. Coax stub is isolated by a dielectric material from the upper ridge, and is connected to the lower ridge [44].

3.3.3 Simulation of ridged waveguide

The ridged waveguide has the same dimensions as calculated in section *3.2.1 Design of waveguide for rectangular horn*. The critical parameters are mainly the gap and the width of the ridges. Simulations has been carried out in order to optimize these two parameters.

It was found that a gap equal to 1 mm and a ridge-width equal to 10 mm gave the best performance. A plot of S_{11} is shown in Figure 3.12. The new bandwidth

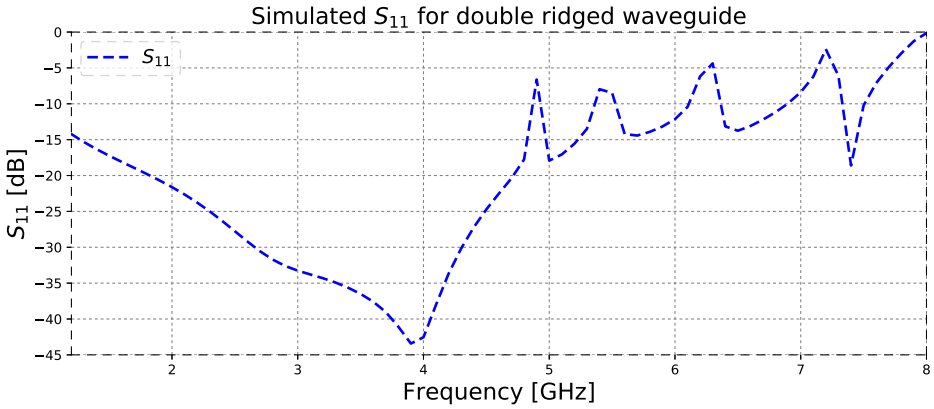

Figure 3.12: Plot of S_{11} for double ridged waveguide with a gap of 1 mm and a ridge-width of 10 mm.

for the waveguide is in the region between approximately 700 MHz to 4.9 GHz, giving a total bandwidth of 4.2 GHz. Comparing this result with the one in Figure 3.3 for the rectangular waveguide, it is clear that by adding ridges increases the bandwidth. However, this does not meet the system requirements for a bandwidth between 2.5 GHz and 5.5 GHz. From the figure it is shown that the upper frequency is almost unchanged, while the lower frequency is shifted down by more than 3 GHz. Therefore, one possible solution for obtaining a bandwidth covering the entire

region, would be to move the lower cut-off frequency to an higher frequency. This will be discussed in the next section.

3.3.4 Design of double ridged waveguide for a new cut-off frequency

Increasing the cut-off frequency, will result in an increase for the band of operation in the frequency scale. Because the size of the waveguide is proportional to the lower cut-off frequency, it will result in a smaller waveguide. Table 3.2 shows the design-parameters for a new ridged waveguide with a cut-off frequency of 4 GHz and a center frequency of 6 GHz.

Parameter	Unit
f_0	6 GHz
f_c	4 GHz
λ_0	49.97 mm
λ_c	74.95 mm
λ_g	67.04 mm
a	37.47 mm
b	18.74 mm
s	5.00 mm
d	1.00 mm
l	37.47 mm
cavity depth	16.76 mm

Table 3.2: Parameters for new waveguide with a cut-off frequency of 4 GHz. See Figure 3.10 for dimensions.

The first approach is to characterize the new waveguide as an standard rectangular waveguide in order to see if the new shape changes the frequency band. A plot of S_{11} is shown in Figure 3.13. The results shows a bandwidth of approximately 3

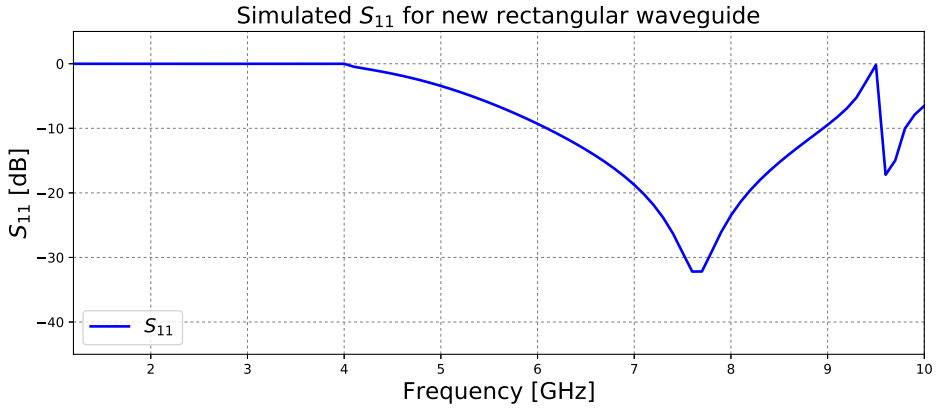

Figure 3.13: Plot of S_{11} for new waveguide with f_c = 4 GHz and f_0 = 6 GHz.

GHz in the range 6 GHz to 9 GHz. The simulated model is a bit different from the

model in the previous section. For the calculated dimensions in Table 3.2, it was experienced that using a standard probe feed for feeding this waveguide decreased the performance significantly. One possible solution, would be to add a shaped probe instead. A model of a shaped probe is illustrated in Figure 3.14.

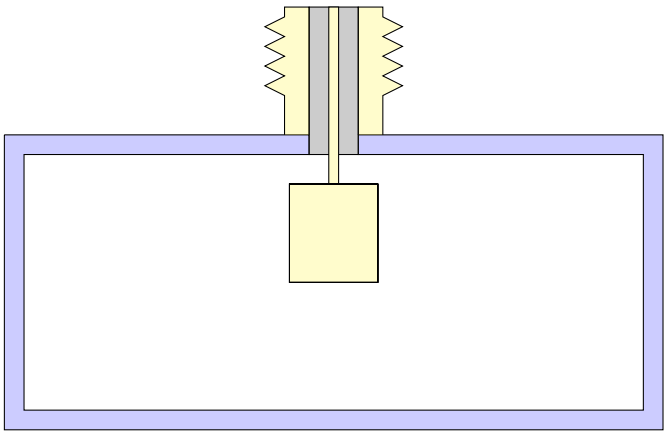

Figure 3.14: Cross section of waveguide with shaped feed probe.

The next step is to add ridges to the waveguide. The gap and width of the ridges has been optimized through simulations, and is listed in Table 3.2. The complete model can be seen in Figure 3.15. The feeding technique is the same as designed in the previous section. The simulation result for the reflection coefficient is shown in Figure 3.16. The new bandwidth is approximately between 2 GHz and 8 GHz, giving a total bandwidth of 6 GHz.

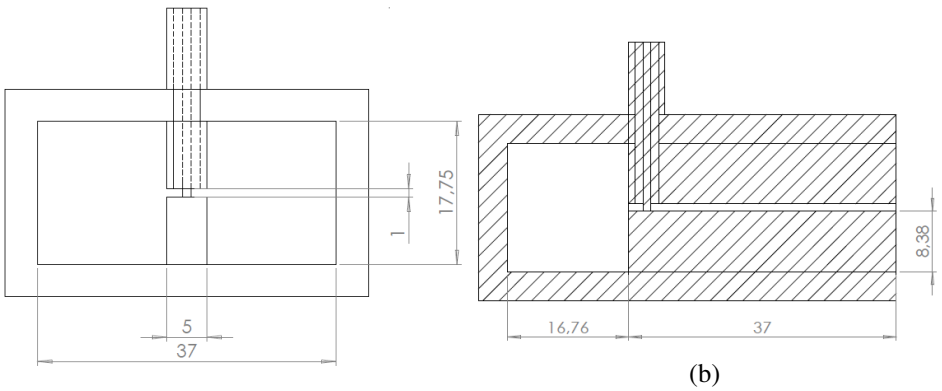

(a) (b)

Figure 3.15: Cross section of new ridges waveguide. (a) cross section of waveguide side and, (b) waveguide front.

Reducing the size of the waveguide shows significant improvements for the desired bandwidth. Comparing the results obtained by the old ridged waveguide and the new, shows an increase in the bandwidth from 5 GHz to 6 GHz. Also, the lower and upper frequency band has changed from 1 to 1.9 GHz and 4.9 to 7.9 GHz. It is therefore reasonable to use the new waveguide for further use when the horn section

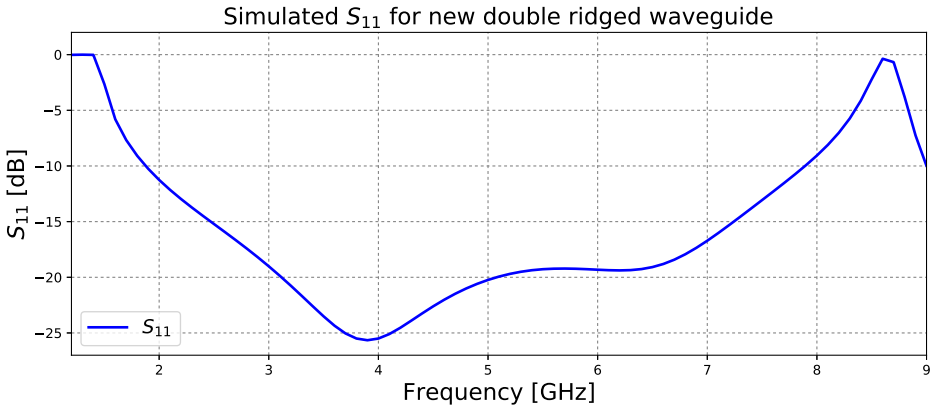

Figure 3.16: Plot of S_{11} for new ridged waveguide with $f_c = 4$ GHz and $f_0 = 6$ GHz.

is to be designed.

3.3.5 Design of tapered ridged horn aperture

The double-ridged horn antenna is a well known antenna used for wideband applications. The main functionality of the ridges is to ensure a smooth transition from the input impedance of 50 Ω to the impedance of free space (377 Ω). This is accomplished by tuning the width and height of the ridges [44].

In the previous section, it was shown that reducing the size of the waveguide and by adding ridges, improved the bandwidth. A reduction in the size is beneficial for the production of the antenna. Smaller geometries gives shorter 3D printing time and lower cost, in addition to a smaller radar system. Since the size of the waveguide is changed, the horn aperture dimensions designed for the previous antenna can not be used because the geometry of the horn is dependent on the size of the waveguide. Table 3.3 summarizes the new and old dimensions together width the difference in the size. From the table, it is observed that the height and width is almost unchanged, while the length is increased by 37 mm. According to Eq. (3.14) this is expected since the aperture size is only dependent on the gain.

Proper design of the shape and width of the ridge is important for a functional waveguide. If the shape is not well designed, it may trap the propagating mode which will cause mismatch and reduction in gain. It is therefore important that the ridge supports the dominant mode everywhere along the geometry [50, pp. 14-62 to 14-63].

The tapered ridge can be designed in many ways. In this thesis, two different design approaches will be discussed. The first is a sectional design method, which use the geometry of the horn section, and the input- and output impedance to calculate the shape of the ridge. The second approach, uses similar design steps as for designing an Vivaldi microstrip antenna [51]. This second approach is not directly dependent on the horn geometry, but rather dependent on an constant, R, which will be discussed in the associated section.

	New horn	Old horn	Difference
G	15 dBi	15 dBi	-
A	183.38 mm	187.78 mm	-4.41 mm
R_H	242.22 mm	253.14 mm	-10.92 mm
L_H	178.38 mm	141.26 mm	37.12 mm
D_H	224.20 mm	235.08 mm	-10.88 mm
B	173.21 mm	165.50 mm	7.71 mm
R_E	217.96 mm	200.48 mm	17.48 mm
L_E	178.38 mm	141.26 mm	37.12 mm
D_E	200.02 mm	182.60 mm	17.42 mm

Table 3.3: New and old horn dimensions for a gain of 15 dBi.

Exponentially tapered ridges using sectioned design method

Sectioned design method is fairly dependent on the horn geometry. Using this design approach ensures good matching for the transition between the input and output. This is because the design equations are directly dependent on the associated input- and output impedance. The accuracy of the antenna performance is given by the number of sections designed. More sections gives better performance. The two most important parameters are the gap and the width of the ridge. The width was found from the simulations of the ridged waveguide discussed in the previous section. The gap is determined for each section using the following design steps [52],

$$Z_i = Z_0 e^{\alpha y_i}, \qquad y_i = \frac{iL}{n}, \qquad i = 1, 2, ..., n \tag{3.15}$$

where: Z_i = characteristic impedance of each step
Z_0 = characteristic impedance of the feed
y_i = length of the ridge section.

The constant α is calculated using the equation,

$$\alpha = \frac{1}{L} ln\Big(\frac{Z_L}{Z_0}\Big) \tag{3.16}$$

where: L = length of the horn section
Z_L = intrinsic impedance of free space.

The spacing between the two ridge-sections seen in Figure 3.17, is given by an exponential function given as,

$$d_i = a e^{b y_i} \tag{3.17}$$

where a and b are constants given by

$$a = d_0, \qquad b = \frac{1}{L} ln\Big(\frac{d_L}{d_0}\Big) \tag{3.18}$$

where: d_0 = length of input aperture
d_L = length of output aperture.

Inserting values for the gap between the ridges in the waveguide section (d_0), the height of the horn aperture (d_L), and the length of the horn section (L) into Eqs. (3.15) - (3.18), gives the following results listed in Table 3.4. It is seen from the table that the characteristic impedance (Z_L) is matched from 50 Ω to 377 Ω as the ridge tapers.

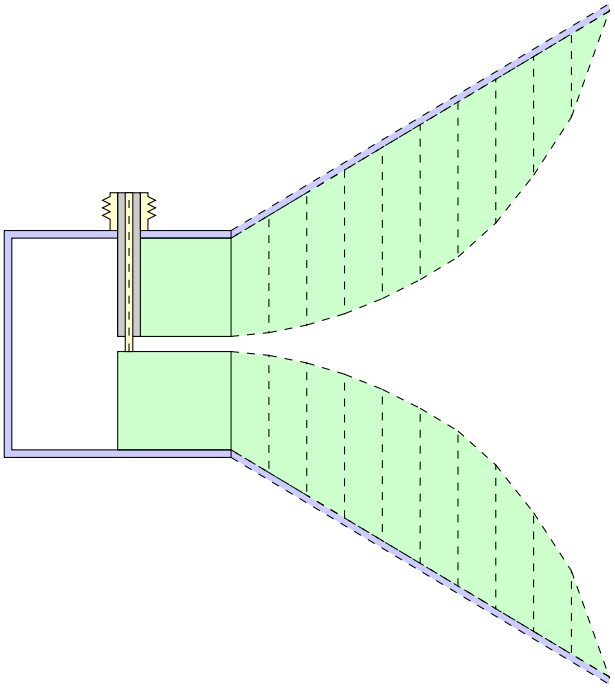

Figure 3.17: Cross section of ridged tapered horn.

n	y_i (mm)	Z_L (Ω)	d_i (mm)
0	0	50	1.00
1	17.84	61.19	1.67
2	35.68	74.89	2.80
3	53.51	91.66	4.69
4	71.35	112.18	7.86
5	89.19	137.30	12.16
6	107.03	168.03	22.04
7	124.87	205.56	36.90
8	142.70	251.69	61.78
9	160.54	208.04	103.45
10	178.38	377.00	173.21

Table 3.4: Dimensions for the ridged sections.

Simulation results

A 3D model of simulated antenna can be seen Figure 3.18, and a drawing of the antenna cross section including dimensions for the ridge sections can be seen in

Figure 3.19. The reflection coefficient (S_{11}) is plotted in Figure 3.20. It is shown

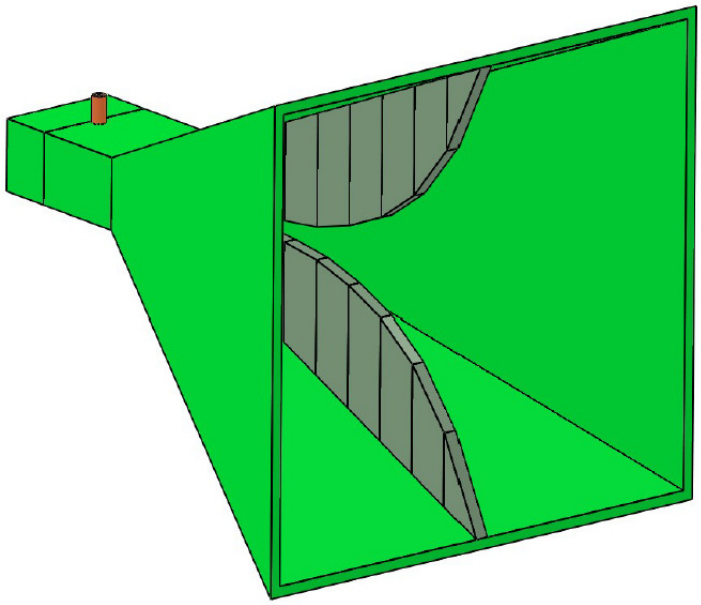

Figure 3.18: 3D model of the ridged horn with section design method. The antenna is fed by a standard coax-to-waveguide transition.

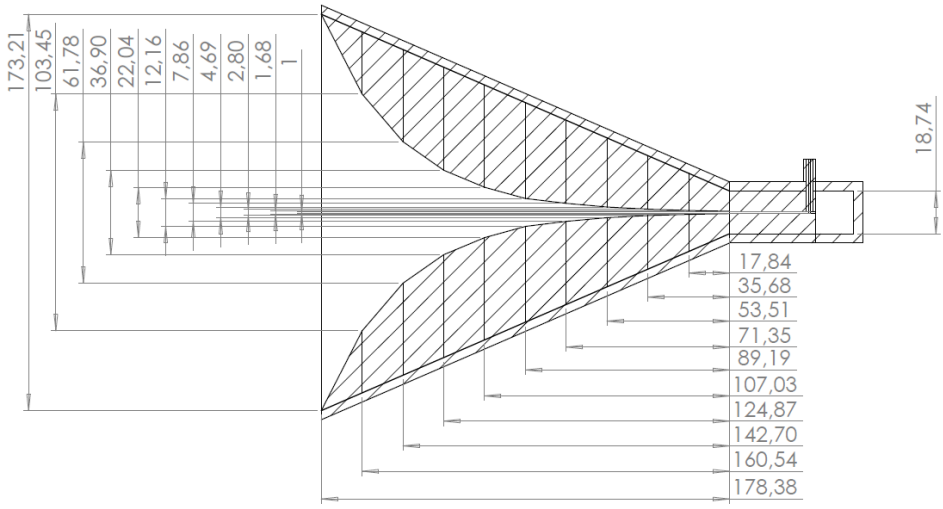

Figure 3.19: Cross section of ridged horn antenna including dimensions for the ridge sections.

that the bandwidth of the antenna is approximately 5.6 GHz in the frequency range between 2.4 GHz and 8 GHz. This is approximately the same bandwidth as achieved for the waveguide alone, meaning that the tapered ridges ensures good transition between the source and load.

One major drawback using tapered ridges, is reduction in the gain. A plot of the gain

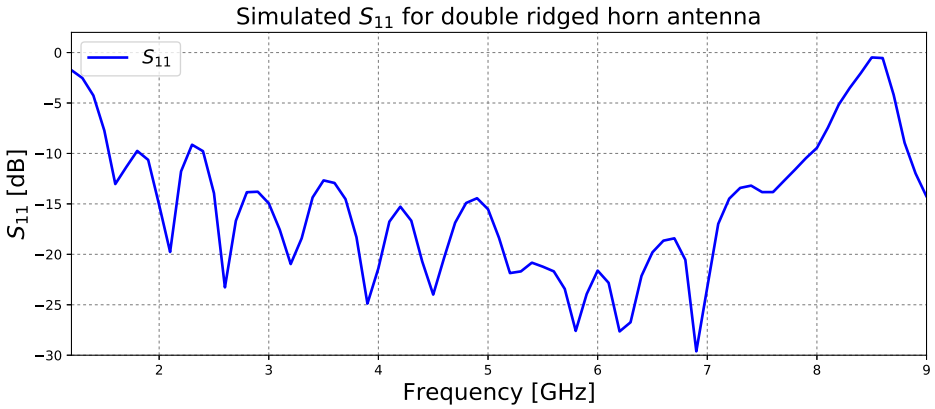

Figure 3.20: Plot of reflection coefficient, S_{11} for ridged horn antenna.

versus the frequency can be seen in Figure 3.21. For the standard rectangular horn designed in the section *3.2.4 Design of horn aperture*, it was shown that the gain was approximately linearly increasing as the frequency increased. For the ridged

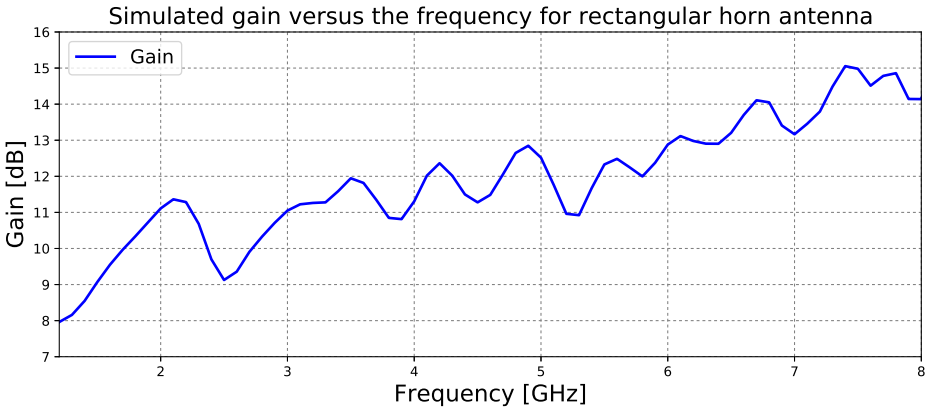

Figure 3.21: Plot of gain versus frequency.

horn antenna, this is not the case. Using ridges, decreases the gain performance of the antenna significantly. This is an trade-off one has to take into considerations when designing an horn antenna for a specific application. At 4 GHz (f_o), the gain of the antenna is approximately equal to 11 dBi. This does not meet the system requirements for a gain of 15 - 20 dBi.

Figure 3.22 shows a plot of the E-plane and H-plane at 4 GHz. In the H-plane, a HPBW of approximately 40° was obtained. For the E-plane, a HPBW of approximately 60° has been simulated. This is an significant increase compared to the rectangular horn. Also, comparing the front-to-back of the two antennas, it is seen that the new ratio is approximately 16 dB compared to 27 dB. The overall performance of the gain and directivity is reduced compared to the rectangular horn, besides the bandwidth which is significantly improved.

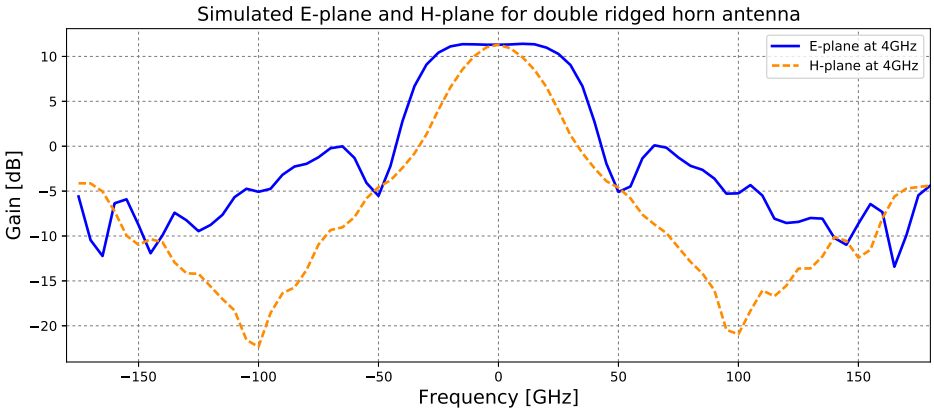

Figure 3.22: Plot of the E- and H-plane directivity at 4 GHz showing a maximum directivity of $D_0 = 11.2dB$ with HPBW of approximately 65° and 40° in the E- and H-plane, respectively.

Because the geometry of the ridges is a function of the antenna geometry and the input- and output impedance, it is not possible to change the form of the ridge using this method. This leads to the second design approach, where the ridge geometry follows the same design approach as an Vivaldi antenna.

Exponentially tapered ridge using Vivaldi design method

One possible thought for increasing the total performance of the DRHA, would be to tune the taper and the length of the ridge in the horn section to get the best solution for the gain and the reflection coefficient.

The Vivaldi design approach does not directly depend on the geometry of the horn antenna, neither is it dependent of the input- and output impedance. Using this approach the ridge can be customized to achieve the best suitable result. The equations for the tapered ridge is given by the exponential function [53],

$$y = C_1 e^{Rz} + C_2 \tag{3.19}$$

where: C_1 = First coordinate for the tapered ridge
C_2 = Second coordinate for the tapered ridge
R = Variable for changing the rate of the opening
z = Variable.

The coordinates C_1 and C_2 is given by,

$$C_1 = \frac{(y_2 - y_1)}{(e^{Rz_2} - e^{Rz_1})}, \qquad C_2 = \frac{(y_1 e^{Rz_2} - y_2 e^{Rz_1})}{(e^{Rz_2} - e^{Rz_1})} \tag{3.20}$$

where: y_1 = start coordinates for y direction
y_2 = end coordinates for y direction
z_1 = start coordinates for z direction
z_2 = end coordinates for z direction.

The variable R controls the taper of the ridge, and increasing the R value gives an steeper ridge. Selecting this parameter properly, is the greatest design challenge for an properly designed ridge.

Simulation results

A plot of S_{11} for three different R values, are shown in Figure 3.23. The plot clearly shows the effect of changing the variable. It is shown that for a R equal to 20 gives an bandwidth of approximately 3.3 GHz in the range 4.5 GHz to 7.8 GHz, while for an R equal to 60, the bandwidth is increased to about 5.7 GHz in the range 2.3 GHz to 8 GHz. In this case, the antenna fulfill the requirements for the bandwidth.

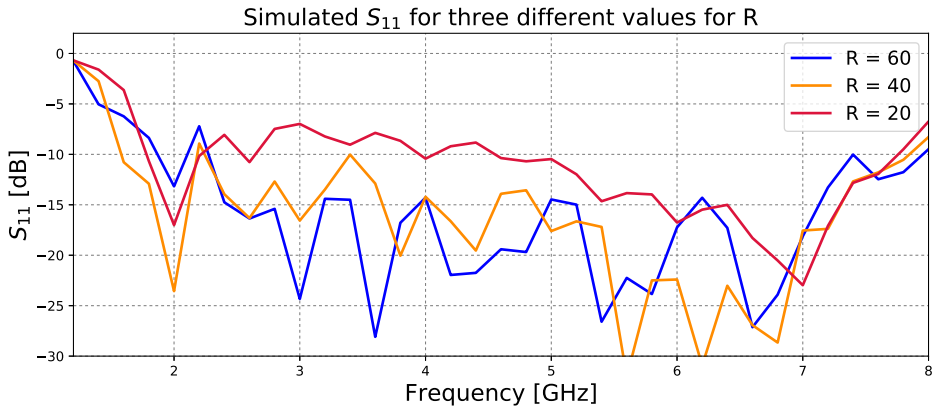

Figure 3.23: Plot of reflection coefficient, S_{11} for ridged horn antenna with three different R values.

Having a relatively steep ridge, ensures good bandwidth, but this will affect the gain of the antenna. A plot of the gain versus frequency for the same values are shown in Figure 3.26. As can be seen, the gain varies due to the changes in the ridge.

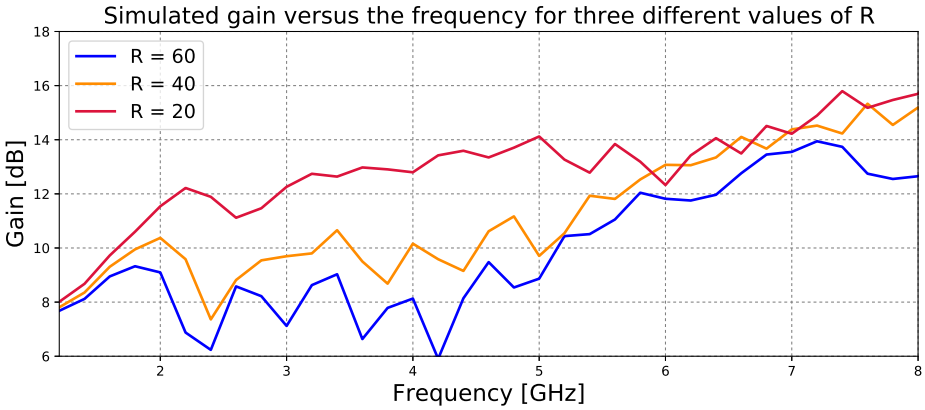

Figure 3.24: Plot of gain versus frequency for three different R values.

The best gain is achieved when the bandwidth is poorest. At center-frequency (4

GHz), the gain is about 13 dBi for R equal to 20 and about 8 dBi for R equal to 60. Reduction in gain is common for double ridged horn antennas as multiple modes are excited and the beamwidth broadens. This effect has been documented by [54, pp. 365-372] and Figure 3.25 shows a plot of the gain for a quad-ridged horn compared to smooth- and corrugated-wall horns.

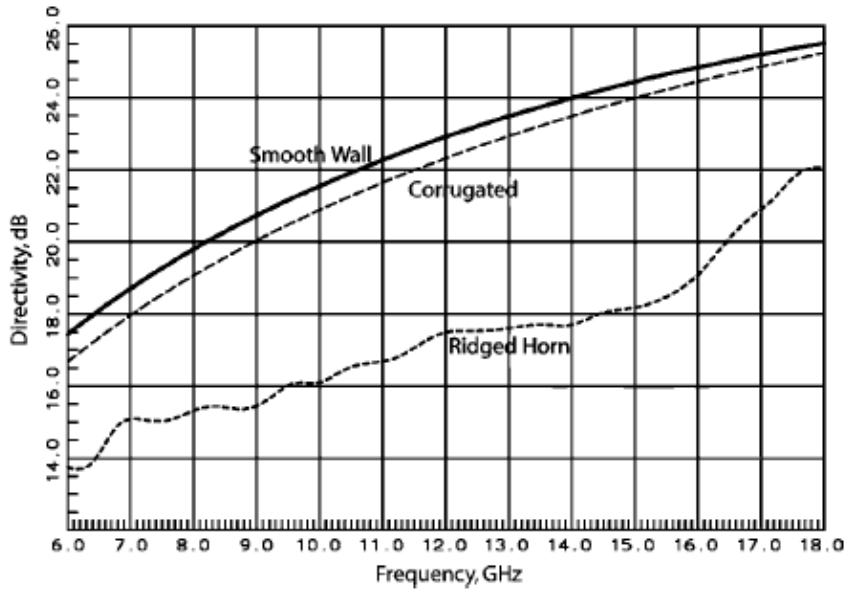

Figure 3.25: Measured directivity of a circular quad-ridged horn compared to those of smooth- and corrugated-wall horns. From [54].

Radiation pattern

The simulated radiation pattern for the E- and H-plane for R equal to 60, 40 and 20 at 4 GHz is shown in Figure 3.26. As previously explained, the highest directivity is achieved when the R-value is lowest. The simulated maximum directivity for this case, is at D_0 = 12.8 dB, with a HPBW equal to 52° in the E-plane and 30° in the H-plane. For the two other R-values, it is observed that the directivity in zenith is slightly degraded from the maximum directivity. As the R increases, this degradation becomes greater. For R equal to 40, the maximum directivity is measured to be D_0 = 10.2 dB, with a HPBW equal to 54° in the E-plane, and 30° in the H-plane. For R equal to 20, the measured maximum directivity is equal to D_0 = 8.1 dB, and the HPBW equal to 56° and 30° in the E- and H-plane, respectively.

3.3.6 Summary

In this section, ridges has been added to the waveguide and horn section. It was shown that the ridge lowered the cut-off frequency of the first dominant mode, which lead to an reduction in the size of the waveguide. This is beneficial considering production time and the practical usage. Then, two different design methods for adding ridges to the horn section was explained and simulated using HFSS. It was shown that the ridges increased the bandwidth of the antenna compared to the

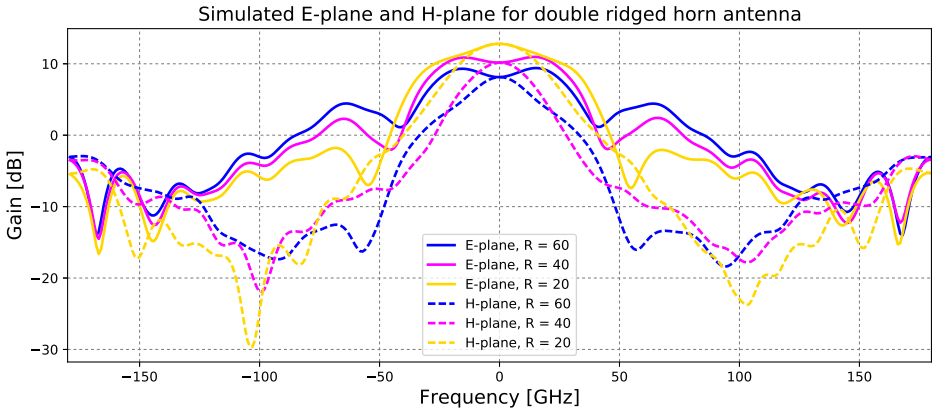

Figure 3.26: E-pane and H-plane directivity at 4 GHz for R = 60, R = 40 and R = 20. Peak directivity of 8 dB, 10.2 dB and 12.8 dB, HPBW of 56°, 54° and 52° in the E-plane. H-plane HPBW of 30°, 30° and 30°, respectively

rectangular horn designed in the first section. However, the ridges also decreased the total gain of the antenna. It is concluded that none of the two design methods for the ridges ware able to meet the system requirements for the gain between 15 dBi and 20 dBi, while keeping the required bandwidth between 2.5 GHz and 5.5 GHz.

Based on the presented results, a idea about decreasing the length of the ridge inside the horn second, and keeping the ridged inside the waveguide could possibly be tuned to find a point where both the gain and bandwidth could satisfy the requirements. This idea was tested in HFSS. The ridge in the waveguide was unchanged, but instead of ending the ridge at the end of the horn section, various lengths for the ridge was tested. Also changing the R values for different length was performed. Simulations showed that the theory did not work. Based on these observations, a new design where stepping the ridges already inside the waveguide, and keeping the horn section as it was for a standard rectangular horn, lead to further work which will explained in a later section.

Because of challenges regarding feeding of the waveguide occurs when dealing with plastic models, a new feeding technique will be examined before the discussion of the new antenna design. The next sections therefore explains with this new technique.

3.4 A new method for feeding plastic waveguides

So fare the discussion of the design method for the different horn antennas has used a traditional method for feeding the waveguide. Using coaxial feed probe requires good and stable connection to the ridge to ensure good electrical characteristics. For a 3D printed antenna, soldering the probe to the ridge would melt the plastic which would have resulted in a deformation in the geometry and change the antenna characteristics. Also, drilling a hole in the ridge and place the probe inside to ensure stable contact as, illustrated in Figure 3.27, would cause trapping of the RF signal below the copper coated layer and probably result in mismatch and unwanted reflections. One possible solution would be to determine the exact required length

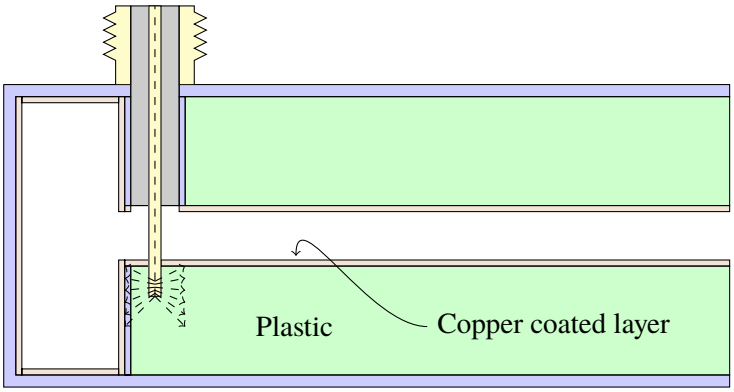

Figure 3.27: Illustration showing the drawback of having a probe connected through a plastic structure with copper coated layer inside.

for the probe, and then use pressure to hold the probe against the ridge. This is not any good solution because the 3D printed semi-flexible waveguide could be deformed by mechanical pressure. Working with light weighted plastic structures introduces new challenges. In this thesis, low-cost 3D printing filaments (PLA) has been explored. However, the selection of 3D printing filaments with different materials are increasing rapidly and alternative, perhaps more expensive, materials may give advantages. In order to solve these challenges, a new technique for feeding ridged waveguides has been developed [31].

3.4.1 Microstrip transmission line feed

Several reports on metalized 3D printed antennas exists, and the performance matches the machined metal reference [55], [30], [56]. Less reports exists on feeding the waveguide and the interface between RF parts and 3D printed parts. Some efforts are reported on Substrate Integrated Waveguides (SIW) used to feed horn antennas instead of using traditional waveguides [57]. However, the purpose of these designs is to replace the heavy waveguide with light substrate integrated waveguides, fed directly to the horn aperture.

The proposed solution discussed in this thesis is to use a PCB microstrip transmission line as waveguide feed. The idea is to clamp the PCB between the cavity and waveguide, as can be seen in Figure 3.28. This solution does not require any

soldering, which makes it more suitable to plastic structures.

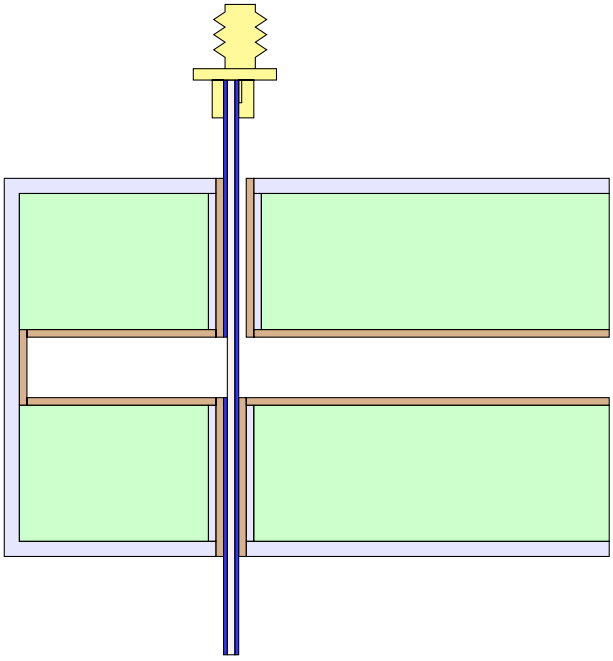

Figure 3.28: Microstrip transmission line feed clamped between the cavity and the waveguide.

A model for the PCB can be seen in Figure 3.29. The PCB is inserted across the waveguide by splitting the model in two. The copper and the substrate is removed for the free space areas of the waveguide imposing negligible interference. Opening the PCB as described, will weaken the mechanical properties but significantly improve RF properties.

Breaking up the waveguide into different parts is in general not preferred due to possible leakage of the RF signals in the gaps between the parts. It is therefore important to minimize this risk. A PCB placed between two waveguide-parts would from an RF perspective look like an air gap with a given permittivity between the two parts. This will cause leakage through the substrate which will cause mismatch in the signal. It is therefore important to place vias around the PCB, avoiding electrical gap between the two parts. Via spacing needs to be less than $\lambda/4$ of the highest propagating frequency. For extra protection, copper sheets between the two copper layers has been included in the simulation.

The gap between the two ridges is matched to approximately 50 Ω in order to match the coaxial probe. It is therefore important that the transmission line is matched to the same impedance. Seen in Figure 3.29, the transmission line is modeled as a coplanar waveguide all the way down to where the ridge ends. After this point, the transmission line is a microstrip stub without ground-plane on the back side of the PCB. The ground plane is removed so that the stub is able to radiate in the way as the coaxial stub. Equations for calculating the width of the copper

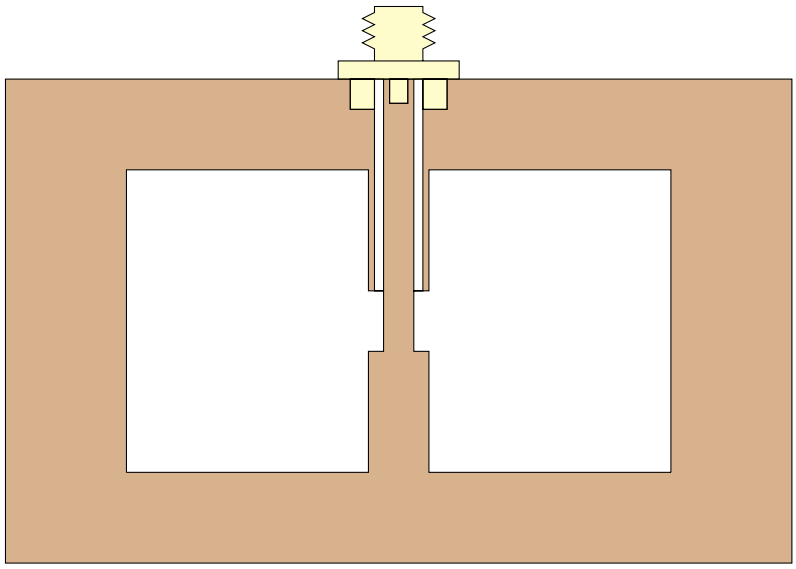

Figure 3.29: Microstrip transmission line feed. The microstrip is matched to 50 Ω.

trace can be found in the literature [50, 51-11 to 51-12] or in Chapter 2. In this thesis, AppCAD has been used. Using FR-4 with a substrate thickness of 800 μm and a copper thickness of 10 μm at 4 GHz, it was found that a width of 1.45 mm and a gap between the transmission line and the top layer ground plane of 1.375 mm gave an characteristic impedance of 50.9 Ω. The coplanar waveguide is terminated through a SMA connector at the top of the substrate, as seen in the figure.

3.4.2 Simulation of microstrip transmission line feed

The validation of the microstrip transmission line feed is done by using the same ridged waveguide model as in section *3.3 Design of tapered ridged rectangular horn*. A 3D model and the cross section similar to the one shown in Figure 3.28 can be seen in Figure 3.30. A model for the SMA connector is not included in the simulation. Instead, a lumped port of 50 Ω is used.

Figure 3.31 shows a plot of the reflection coefficient for the waveguide using traditional coaxial feed, and the new microstrip transmission line feed. The simulation shows that the cut-off frequency for the two models are the same. The coaxial feed model has a band of operation between 2 GHz to 7.9 GHz, while the microstrip feed has a bandwidth between 2 GHz to 8.5 GHz. One interesting observation is the shape of the two plots. For the waveguide using coaxial feed probe, the lowest reflection happens at approximately 4 GHz. For the transmission line solution, the lowest reflection happens at approximately 7.5 GHz. This may be cause by the interface between the coaxial probe and the ridge, and the transmission line and the ridge. The electromagnetic field for a coaxial cable is equal in all directions. When the wave intersects with the ridge, the field is rotated by 90°. From there, the wave will propagate out through the waveguide. Figure 3.32 and Figure 3.34 shows this propagation for four different phases (0°, 90°, 180° and 270°) at 4 GHz and 7.5 GHz, respectively.

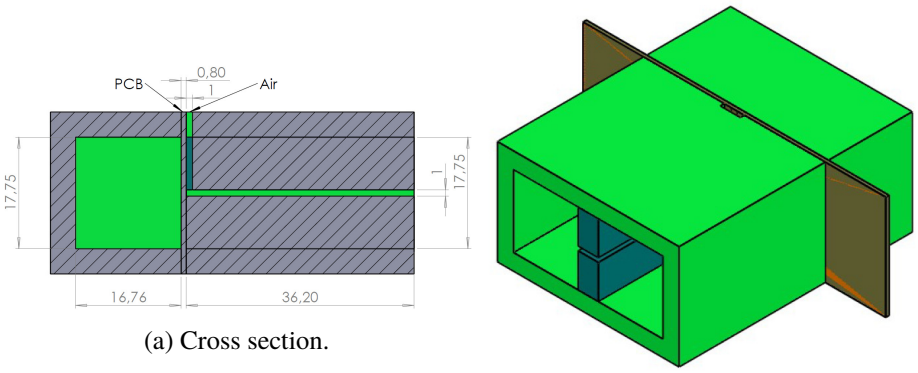

(a) Cross section.

(b) 3D model.

Figure 3.30: Cross section and 3D model of the double ridged waveguide using transmission line feed solution.

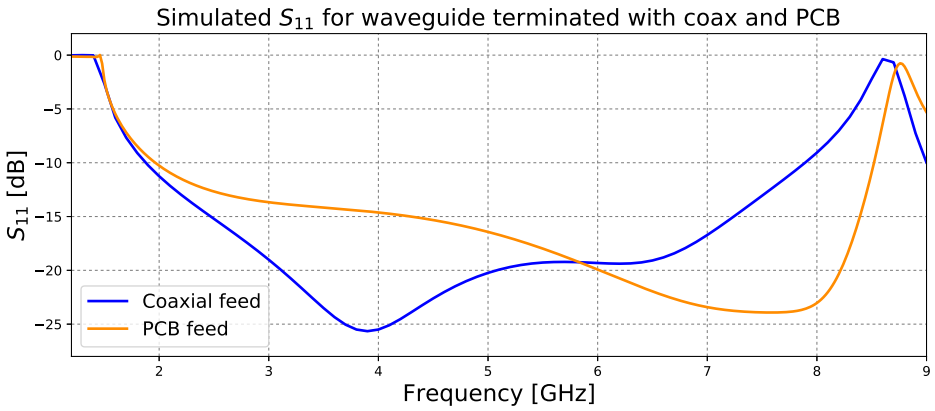

Figure 3.31: Comparing simulated S_{11} for the waveguide using coaxial feed and microstrip feed.

It is observed in the two figures that the E-field has some radiation into the cavity part. Comparing this to the E-field plot for the microstrip feed solution seen in Figure 3.33 and Figure 3.35, it is shown that there are no electrical field radiation into the cavity. It is also seen that the electric field is stronger for the coaxial probe compared to the microstrip solution.

3.4.3 Evaluation the microstrip feed

Based on the modeling results for microstrip transmission line, PCB feed seem to be promising. The simulations shows almost equal results for the reflection coefficient compared to results in Figure 3.31. As discussed in the introduction chapter, the plastic is not conductive and requires copper coating (spraying) for electrical charge transport. Although the complete antenna may be 3D printed as one, solid

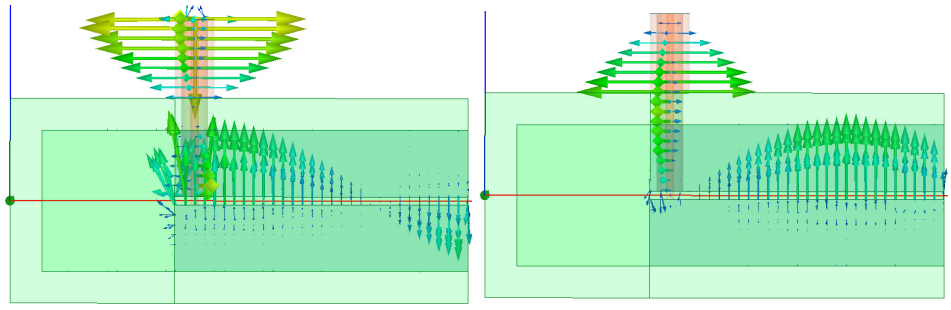

(a) Phase = 0°. (b) Phase = 90°.

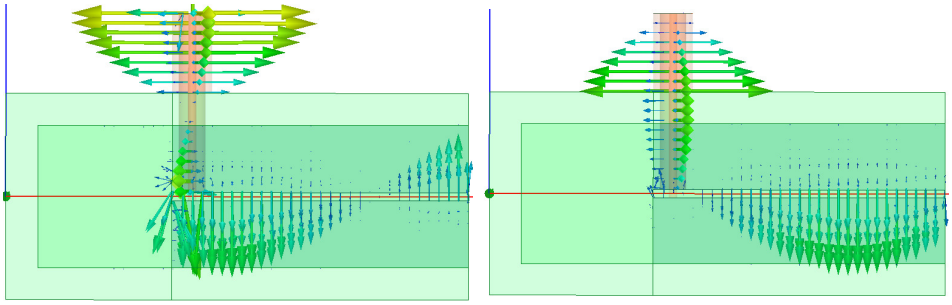

(c) Phase = 180°. (d) Phase = 270°.

Figure 3.32: Plot of E-field vector for coax to waveguide transition for 4 GHz.

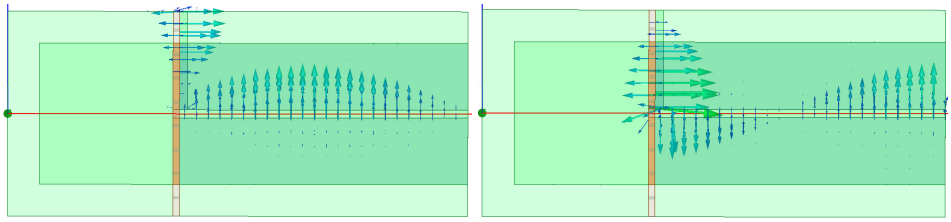

(a) Phase = 0°. (b) Phase = 90°.

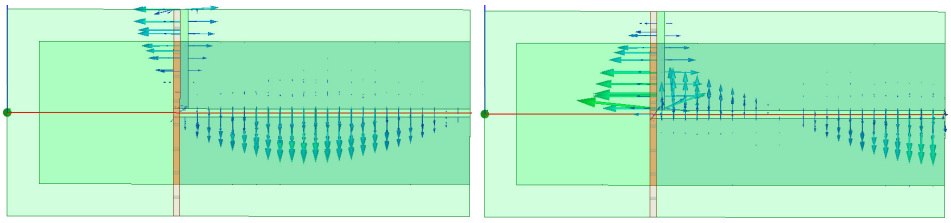

(c) Phase = 180°. (d) Phase = 270°.

Figure 3.33: Plot of E-field vector for microstrip line to waveguide transition for 4 GHz.

structure, spaying of the inside is challenging. Therefor, it is necessary to split the model into smaller parts. This will result in additional splits between the pars, and more signal will probably leak out. The simulation model is a solid model and therefor not suitable for a 3D print. Additional details may be found in *Chapter 4 Measurements and Results*.

The simulated PCB is a 800μm thick FR-4 substrate. This substrate and thickness was selected because of availability in the lab. Such a thin substrate is not

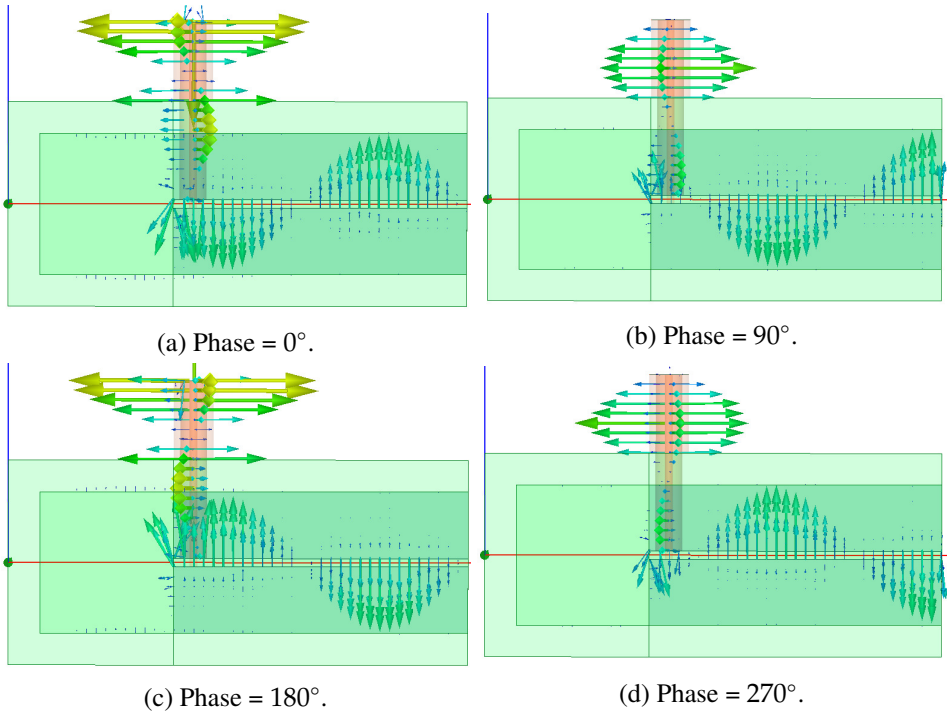

(a) Phase = 0°. (b) Phase = 90°.

(c) Phase = 180°. (d) Phase = 270°.

Figure 3.34: Plot of E-field vector for coax to waveguide transition for 7.5 GHz.

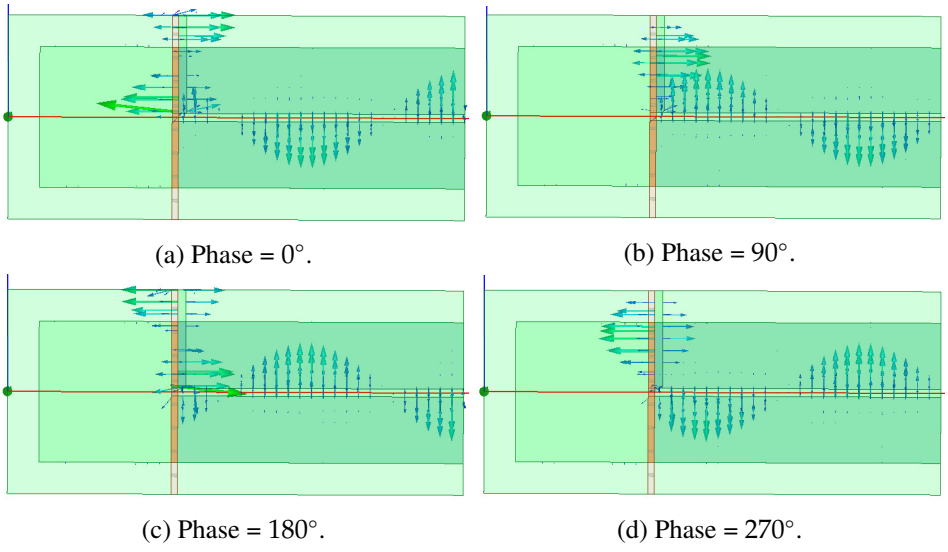

(a) Phase = 0°. (b) Phase = 90°.

(c) Phase = 180°. (d) Phase = 270°.

Figure 3.35: Plot of E-field vector for microstrip line to waveguide transition for 7.5 GHz.

preferred since it is easily exposed to bending, which may impact antenna performance. Perhaps for a further improvement, a thicker substrate is preferred for improved stability. Also, other types of substrate that is more suitable for RF-signals should be evaluated. Using a different substrate or changing the width would require recalculations of the width of the copper trace.

3.5 Design of stepped ridge horn antenna

It was shown in section *3.3 Design of tapered double ridged horn antenna* that none of the previously designed antennas were able to meet the system requirements. In this section a new method will be examined. The principals are the same as discussed in the previous section, where the purpose of the ridge is to ensure a smooth transition between the input of 50 Ω and the output of 377 Ω (free air). This new method takes the benefit from the ridge inside the waveguide to ensure good bandwidth, and the geometry of the horn section to ensure a stable gain over the frequency band. This is accomplished by stepping the ridge inside the waveguide so that the impedance at the end of the waveguide is matched to 377 Ω. Impedance matching in waveguides are commonly used when two waveguides with different operating frequencies is to be matched to each other and are well documented in [58, pp. 261-267] and [59].

Figure 3.36 shows the cross section the proposed stepped ridge horn antenna. In the design of the tapered DRHA in section *3.3.5 Design of tapered ridged horn aperture*, the ridge was tapered out in the horn section. This ensured a smooth

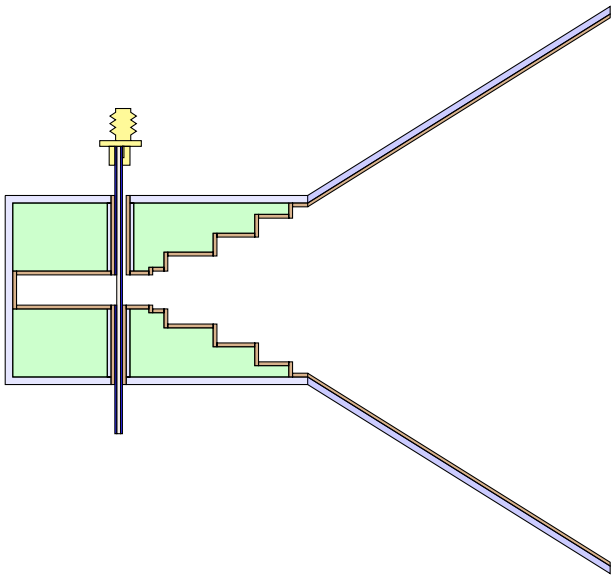

Figure 3.36: Model of stepped ridged horn antenna. Microstrip transmission line feeds the stepped ridge waveguide.

transition between the input and free space. In this design the ridges are stepped in order to match the input to the output at the end of the waveguide. A smooth transition would probably have been better, but the geometry would have been quite complex to model. Even though equations for estimating the steps exists, the dimensions has been optimized through simulations.

3.5.1 Design of stepped ridge waveguide

Stepped ridges has been widely use for some applications regarding matching between two dissimilar waveguides or between ridged waveguides and a coaxial line

[49]. The design for the stepped ridge waveguide in this thesis is based on two other reference designs [60] [59]. [60] explains in short terms the concept of the transition between a coaxial line and a double-ridged waveguide using stepped ridges for impedance matching. [59] explains the design method for matching a high impedance waveguide to a low impedance coaxial line using a Chebyshev type of impedance match. Common for the two designs, is the coax to waveguide transition. The proposed design uses the microstrip feed solution explained in the previous section, and not the coaxial transition.

In the design of the tapered DRHA, it was shown a trade-off between the gain and bandwidth. Seen in Figure 3.36, the ridges are ended inside the waveguide section. The idea is to use ridges in the waveguide and keep the horn section as it was for a standard rectangular horn antenna. The ridging ensures good bandwidth and the horn ensures stable gain over the entire frequency band. To do so, it is important that the ridges are matched already inside the waveguide. If this is not done properly, there will be a mismatch between the input and output.

To begin with, only the waveguide section will be examined together with the microstrip feed solution. Because stepping the ridges will change the first and second dominant cut-off frequency, it is reasonable to believe that the bandwidth will become more narrow. The waveguide designed in section *3.2.1 Designing a waveguide for rectangular horn* is therefor the preferred model to use, because it was designed for a cut-off frequency of 2 GHz and a center frequency of 4 GHz. Each stepping of the ridge is carefully designed in order to reduce the reflections back to the input. It was experienced that by completing the ridge all the way inside the cavity gave a better result for the reflection coefficient. Also, changing width of the ridges from 5 mm to 6 mm gave an better result. Table 3.5 shows the height and length for each of the steps inside the ridge. At the 4th step, there are two lengths.

Parameters	End of waveguide	1st step	2nd step	3td step	4th step
Height of ridge (mm)	0	4.86	6.08	6.08	1.22
Depth of step (mm)	11.99	21.74	18.74	17.49	4.20+19.55
Impedance (Ω) (2.5 GHz - 5.5 GHz)	425 -255	355 - 245	235 - 190	98 - 96	45 - 45

Table 3.5: The height, length and impedance for each step.

The first is from the edge of the step to the PCB, and the second length is from the PCB to the back of the cavity. Figure 3.37 shows the simulated stepped ridge waveguide.

3.5.2 Simulation of stepped ridge waveguide

A plot of the reflection coefficient can be seen in Figure 3.38. The bandwidth below -10 dB is found to be 2.8 GHz in the range 2.3 GHz to 5.1 GHz. As expected, the bandwidth is significantly decreased compared to the one simulated in Figure 3.31. This is due to the stepping of the ridge. As explained in an earlier section, the gap

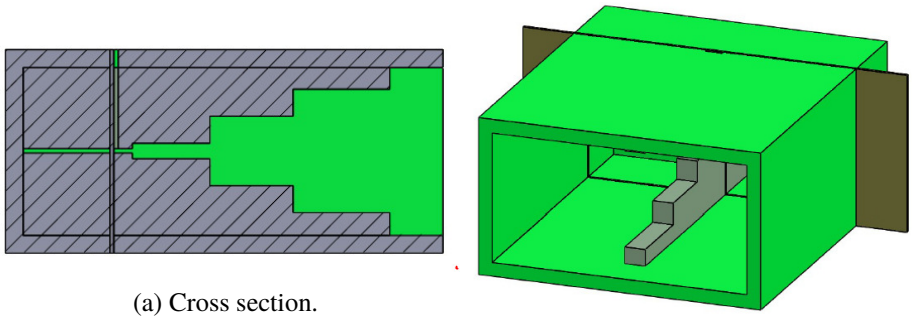

(a) Cross section.

(b) 3D model.

Figure 3.37: Cross section and 3D model of the stepped double ridged waveguide using transmission line feed solution.

between the ridges is an important parameter for optimal bandwidth. As the gap now increases, it is therefore expected with a reduction in the bandwidth.

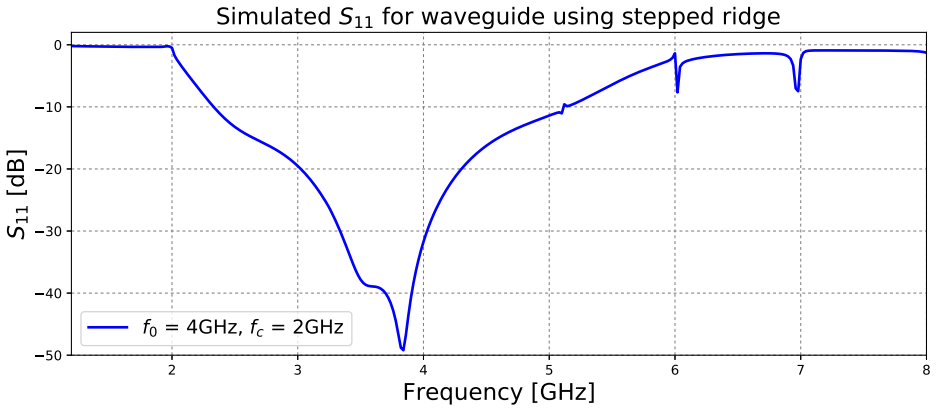

Figure 3.38: Plot of S_{11} for stepped ridge waveguide with microstrip feed.

Figure 3.39 shows a plot of the impedance at each step. As the frequency increases, the impedance decreases. This is expected since the characteristic impedance is a function of the frequency, as can be seen in the following equation [61].

$$\frac{Z_0}{Z_{0\infty}} = \frac{1}{\sqrt{1-\left(\frac{f_c}{f}\right)^2}} \tag{3.21}$$

where: Z_0 = characteristic impedance
$Z_{0\infty}$ = characteristic impedance at infinite frequency
f_c = waveguide cut-off frequency
f = operating frequency.

Table 3.5 summarizes the different impedances for the range between 2.5 GHz to 5.5 GHz for each of the steps in the waveguide.

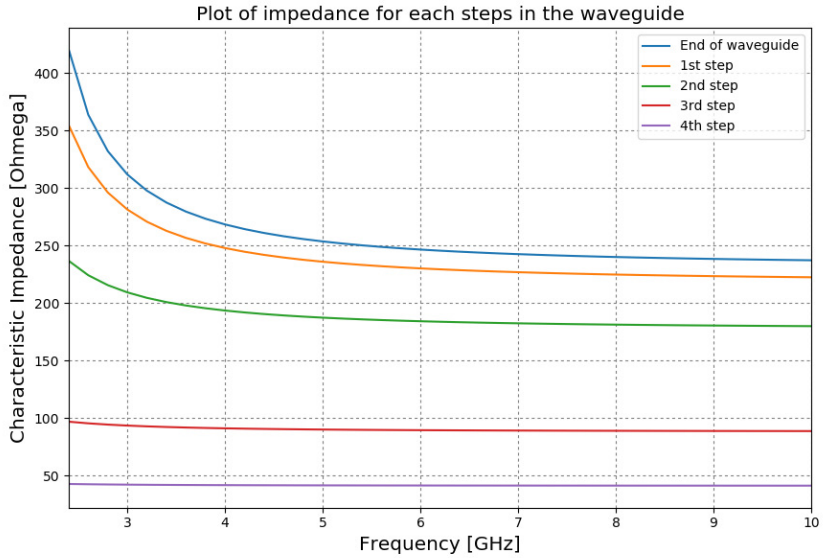

Figure 3.39: Plot of impedance at each step in the waveguide.

The stepping of the ridge is promising despite that the bandwidth does not entirely fulfill the requirement between 2.5 GHz to 5.5 GHz. More tuning of the steps would probably have given an better result, but due to time limitations it was decided to use the presented design. Also, as an further improvement it would have been interesting to model the ridges more smoother, same as for an tapered ridge. Smoother edges would have been preferred over stepped ridges, but this would have result in an increase in the complexity of the geometry [49]. The solution presented does not have an logarithmic approximation so tapering would not work.

3.5.3 Design of stepped ridge horn antenna

It has been shows that the bandwidth of a rectangular horn antenna was unchanged when the horn aperture was added to the waveguide. In this design, this benefit has been exploited. The dimensions are experimentally evaluated in order to achieve the best possible result. Table 3.6 summarizes the three different aperture configurations that were tested. The second column is a special case, where the width and height of the aperture is scaled by 1.2 times the size for the aperture designed for 12 dBi gain. The length of this horn is selected to be 100 mm for practical purposes.

	$G_{dBi} = 12dBi$	$G_{dBi} = 12dBi$ (scaled by 1.2)	$G_{dBi} = 15dBi$
Width	132.87 mm	159.44 mm	187.78 mm
Height	108.48 mm	130.18 mm	165.50 mm
Length	51.31 mm	100.00 mm	141.26 mm

Table 3.6: Horn aperture dimensions for three different cases.

3.5.4 Simulation of stepped ridge horn antenna with microstrip transmission line feed

Figure 3.40 shows a plot of S_{11} for the three different horn apertures. From the figure it is clear that the bandwidth is almost unchanged for the three sizes. Based on these results, it is shown that the stepping of the ridges is beneficial regarding the bandwidth. It also means that if a higher gain is needed, it is possible to replace the horn section and keep the waveguide as it is. This is especially beneficial for 3D printed antennas.

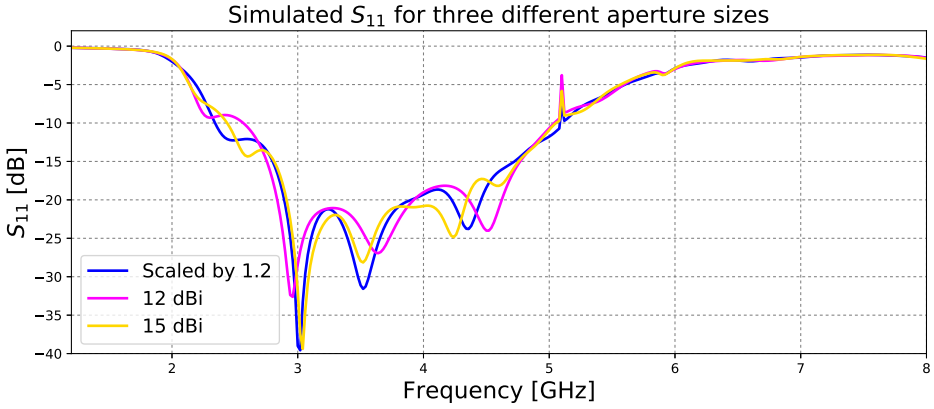

Figure 3.40: Effect on bandwidth with three different horn apertures.

Comparing the simulated S_{11} for the horn antenna and the waveguide shown in Figure 3.38, it is seen that the shape of the curves is changed. Adding the horn aperture to the waveguide gives more reflections within the band of operation. However, these reflections are in the order of -20 dB or 1 % of the transmitted signal. Comparing the upper and lower cut-off frequency at the -10 dB point it is shown that for the complete horn antenna, the bandwidth is approximately between 2.4 GHz and 5.1 GHz. For the waveguide alone, the bandwidth was found to be between 2.3 GHz and 5.1 GHz.

Figure 3.41 shows a plot of the gain against the frequency. As was seen for the tapered ridged horn antenna, the gain varied significantly within the band of operation. Seen in the figure for the scaled antenna, the gain varies between 11.4 dB for 2.4 GHz and 17.0 dB for 5.1 GHz. At the center frequency of 4 GHz, a gain of 15.4 dB is achieved. Above 6 GHz the gain starts to decrease due to mismatches in the antenna. However, this is beyond the frequencies of interest. One other observation is that the gain increases almost linearly from 1.9 GHz until it reaches 5.5 GHz. This is good because it ensures stable and high gain over the entire bandwidth.

The simulated E-plane and H-plane cut of the radiation pattern at 4 GHz can be seen in Figure 3.42. At 4 GHz the boresight gain is 15.4 dB and front-to-back ratio is 22 dB. The simulated HPBW is approximately 24° in the E-plane and 26° in the H-plane. This was also the same results obtained for the rectangular horn antenna.

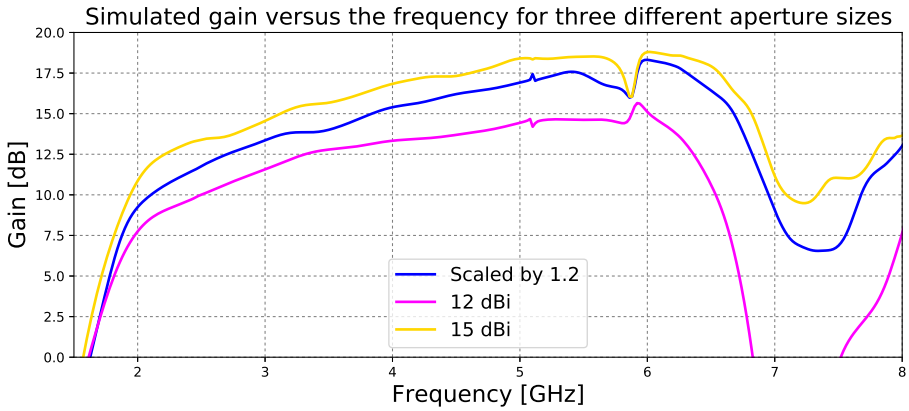

Figure 3.41: Plot of gain versus frequency for three different aperture sizes.

Figure 3.42: Plot of E- and H-plane directivity at 4 GHz for the stepped ridge horn antenna with mictrostrip transmission line feed. Peak gain of 15.4 dBi. HPBW of 24° in E-plane and 26° in H-field.

3.5.5 Summary of stepped ridge horn antenna

The stepped ridge horn antenna (SRHA) with the new feed solution looks promising despite that the requirement for the bandwidth was not entirely fulfilled. As explained in Chapter 2, the Ventricorder radar module has the ability to switch between different PG-selections. If the center frequency is set to an lower frequency, the antennas with the achieved bandwidth will work fine. The problem arises when the center frequency are shifted to an higher frequency. The achieved bandwidth of 2.7 GHz in the range 2.4 GHz to 5.1 GHz will therefore work fine for lower PF-selections.

The new feed solution matches the traditional coaxial probe feed. This is very beneficial regarding the implementation to the 3D printed horn antenna. In addition, for a system without RF cables where the radar and antenna feed is assembled on the same PCB is feasible removing the cost of SMA connectors and RF cables.

3.6 3D printed antennas

The focus in this thesis is to create a 3D printed horn antenna using low cost thermoplastic polymers (ABS, PLA). So fare the discussion has been focused on the design of the horn antenna discussing the performance of different types of configurations. To meet the requirements for the remote Geo-Sensing, it is important that the system is light weighted and easy to carry. Fabricated horn antennas that matches the size of the one designed in the previous section, weights about 1.6 Kg [62]. For a complete radar system, two of these antennas are needed, resulting in a total weight of 3.2 Kg, only for the antennas. Also, the price is an crucial factor. Antennas in the same category, costs about $3,500.00. Both reducing the weight and cost are two important aspects regarding 3D printed antennas. Some work has been developed regarding metalized 3D printed plastic antennas, and the performance matches the machined [30] [31].

3.6.1 Challenges by 3D printing antennas

As was explained in Section *3.4 A new method for feeding plastic waveguides* problems arises regarding the feeding of the plastic waveguide. As a proposal to this problem, a PCB feed is placed between the cavity and the waveguide. Splitting the waveguide is not preferred as the RF-signals may leak out in the gaps between the 3D printed parts. Minimizing this risk is therefore extremely important for maximum performance.

Another problem that arises, is the metallization of the plastic parts. PLA has a permittivity of approximately 3.5 [63] which means that if the 3D part is not entirely copper coated, the RF signal will leak out from the uncovered areas. In order to ensure good copper coating, the model has to be split into several smaller parts. Regarding the metallization, the copper coating spray will contribute to much more electrical losses compared to a conventional metal antenna. The resistive losses for three copper coated layers is 0.011 Ω/sq [64]. This assumes that the entire model is equally coated. The resistive losses have been simulated in HFSS on the same antenna model explained in the previous section, to see the difference between PEC and realistic values for the electrical conductor. The results can be seen in Figure 3.43.

Simulations shows minor differences in the PEC simulated model and the one with realistic values. However, this assumes that the copper is equally coated over the entire surface. In addition, the model has been simulated as a solid model covered with the realistic material, and not specified for any layer thickness.

3.6.2 3D printed stepped ridge horn antenna

To minimize the risk of leakage of the RF-signal, it is crucial that the mechanical parts of the antenna is designed properly. Figure 3.44 shows a model of the printed SRHA designed in HFSS (see Appendix B for machine drawings). The horn aperture is split into four parts, one for each of the walls. To assemble the walls, the parts are screwed together at the outside of the antenna, as can be seen in the

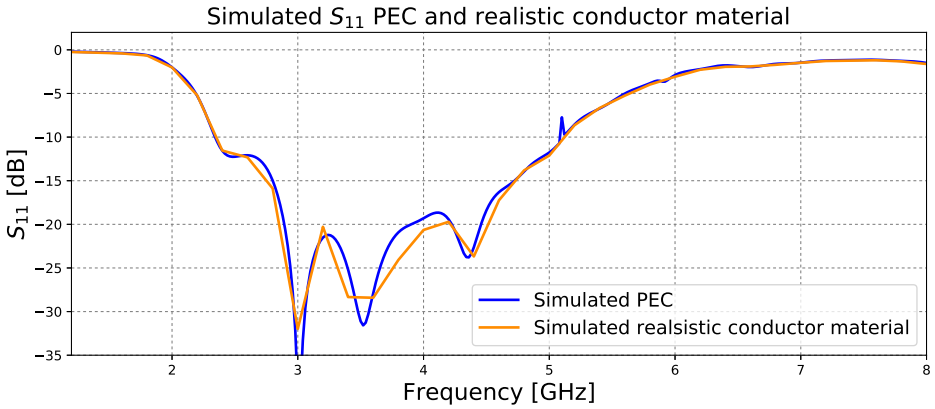

Figure 3.43: Comparing S_{11} for SRHA simulated with PEC and realistic values for electrical conductor.

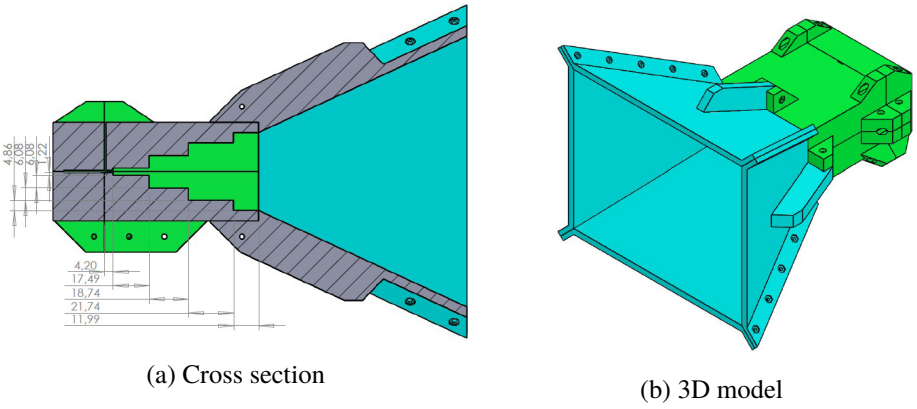

(a) Cross section

(b) 3D model

Figure 3.44: Model of the 3D printed antenna. (a) showing the cross section of the 3D printed model including dimensions for the ridges. (b) showing the 3D printed model with montage for the different mechanical parts

figure. Splitting the parts into four makes it easier to copper coat the surface. The drawback of splitting the model, is the possibility of leakage in the gaps between the 3D printed parts.

The waveguide has also been split into four parts for the same purpose. Because of the ridges it is necessary to split the model to ensure good copper coated layers. To eliminate the risk of gaps, screw montages for holding the structures together is added. The most critical part is the interface between the cavity and waveguide, where the PCB is placed. Extra montages has therefore been included in this area.

For 3D printing of the model, Ultimaker 2+/3 Extended has been used. Ultimaker is a Fused deposition modeling (FDM) printer, which means that the printer adds material layer by layer [65]. With layer thickness of 60 μm and high mechanical accuracy, the FDM 3D printer can produce advanced geometrical shapes with smooth surface. Even though, it is shown that the surface roughness has minimal

impact in the performance [66]. The size of the models is limited by the size of build plate (215x215x300).

Preparing the print is one important design procedure. As the 3D printed parts is extruded layer by layer, the parts are weaker in the extruded direction than for the horizontal. It is therefore important that for parts that are highly exposed for stresses and bendings are printed in a way that minimize the risk of damaging the model. Also, printing the model in a difficult direction requires more support material, which will result in longer printing time. These two considerations are important for a optimal print setup and results.

One additional benefit of splitting the antenna into several parts, is the elimination of support material for demanding shapes. The 3D printer is capable of printing in a 45° overhang without the need for support material. Laying the side-walls flat down on the build plate is preferred for optimal strength and lowest possible printing time. Also, the need of support material is minimized and only needed at the screw hole rails. The screw hole montage at the waveguide and cavity is designed to be 45° to eliminate the need for support. The need for support is therefore totally eliminated for all of the antenna parts.

Figure 3.45 shows two 3D printed SRHA's coated with copper on the inside. Each antenna is printed with a layer resolution of 60 μm resulting in a total print time of approximately 100 hours for each antenna. The weight is less than 400 g and the total price including copper coating is approximately $60. This is significantly lower than for the equivalent antennas explained in the beginning of this section.

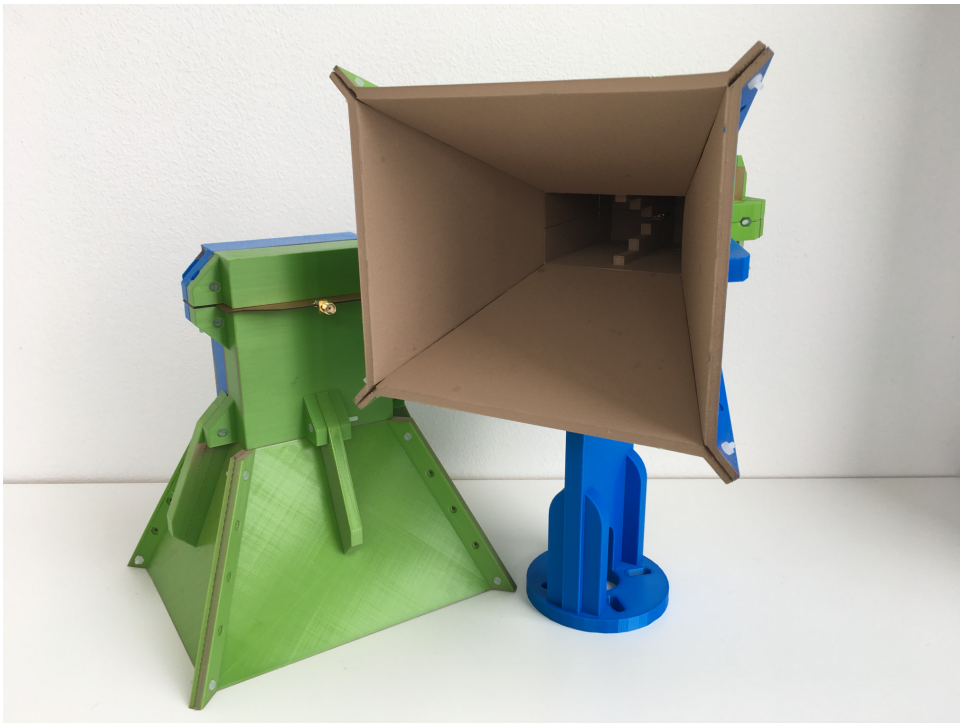

Figure 3.45: 3D printed SRHA.

Chapter 4

Measurements and results

4.1 Introduction

So far the discussion have only considered different designs for rectangular and double ridged horn antennas and waveguides. In this chapter, the printed models has been evaluated in anechoic chamber at the University of Oslo, Department of Informatics. The antennas has also been tested on a simulated snow structure consisting of layers of pressed wood, and outdoor measurements at Finse Alpine Research Center (Figure 4.1). The first part of this chapter presents the setup for the antennas in the anechoic chamber. Later, measured results for the printed antennas will be discussed.

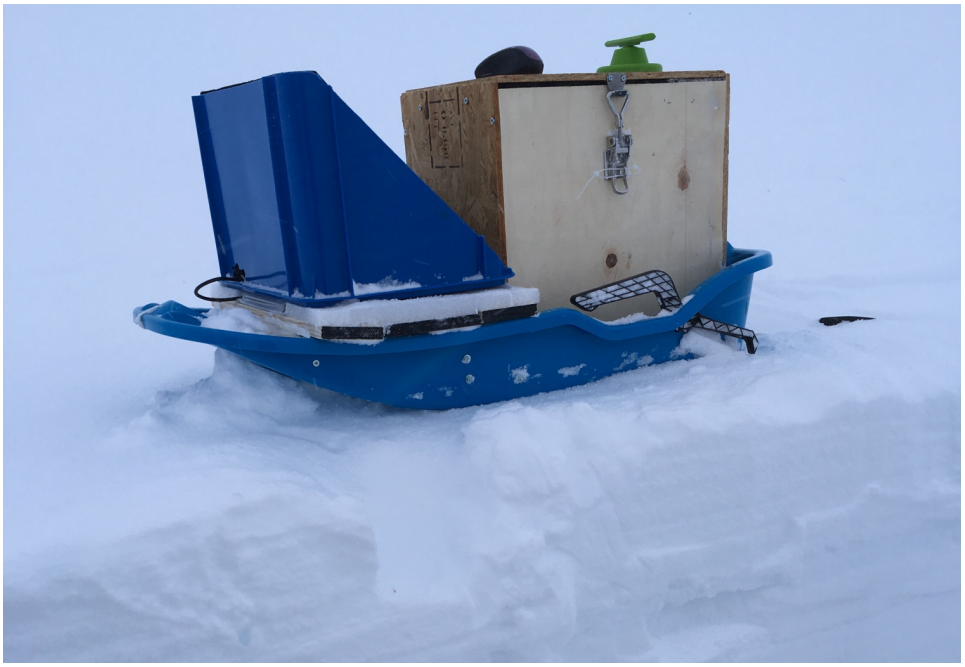

Figure 4.1: The complete radar system implemented on a sled.

4.2 Method

For measurements of the scattering parameters, Rohde&Schwarz vector network analyzer covering frequencies from 10 MHz to 20 GHz, has been used. All measurements of the gain and directivity for the antennas has been performed in a anechoic chamber. The chamber has a size of 6m x 3m x 3m. The reference antenna used for characterizing the printed antennas is a wideband double ridge guide horn (SAS-571) covering the range between 700 MHz to 18 GHz with a gain between 1.4 dBi to 15 dBi [62]. A picture of the setup can be seen in Figure 4.2.

The snow lab measurements has been performed using a several pressed wood plated stocked upon each other, with air-gaps between each plate. The lab- and outdoor measurements has been recorded on a PC running the Matlab script *ModuleConnector* created by Novelda AS.

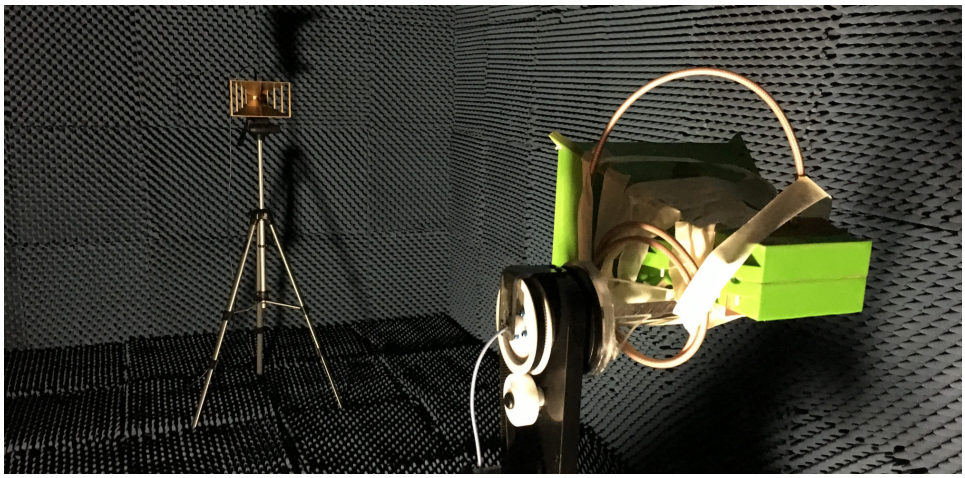

Figure 4.2: Antenna setup in anechoic chamber. Reference antenna is a SAS-571 covering a bandwidth of 700 MHz to 18 GHz .

4.3 Evaluation of the printed waveguide

In section *3.4 A new method for feeding plastic waveguides* in the previous chapter, it was found that the microstrip feed solution matched the results for the traditional coaxial probe feed. This method is simpler to manufacture and more robust when used together with plastic structures. A full scale model of the waveguide that was designed in section *3.3.4 Design of double ridge waveguide for a new cut-off frequency* was then 3D printed in VeroClear plastic and PLA using Object Connex500 from Stratasys and Ultimaker 2+, respectively.

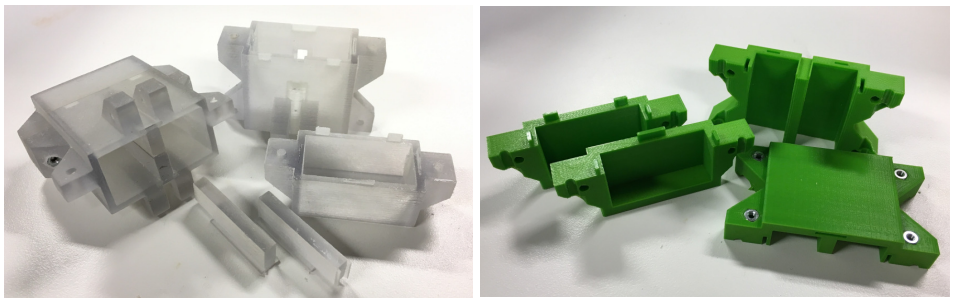

(a) (b)

Figure 4.3: Printed models of the waveguides (a) shows the VerClear model and (b) shows the PLA model.

The first printed waveguide was printed in a plastic called VeroClear [67] and can be seen in Figure 4.3 (a) and the PLA model can be seen in Figure 4.3 (b). Plastics are not conducive itself, so it was therefore necessary to spray the inside with a conductive material. It was found that *MG Chemicals 843AR-340G Super Shield Silver Coated Copper Conductive Coating* [64] was well suited regarding resistive losses and frequency operation range. The 843AR-340G provides high conductivity and a surface resistivity of only 0.011Ω /sq with three coats.

It is crucial that the paint encloses the entire surface at the inside of the waveguide to ensure perfect electrical conductivity. If this is not done properly, it may influence the characteristics and the waveguide may probably not work as expected. One problem that occurred during the painting of the VeroClear, was that the copper spray did not adhere sufficiently to the surface of the material. It was also experienced that if more copper was added to a dry copper layer, the layer started to contract from the plastic. This made it difficult to get a solid layer covering the entire surface.

4.3.1 Measured results for the first printed waveguide

The wavegudie measurements is done by using a two port network analyzer measuring the scattering parameters. In order to measure S_{21}, two identical models were printed and placed against each other as can be seen in Figure 4.4. The scattering parameters are measured in the frequency range 1 to 9 GHz.

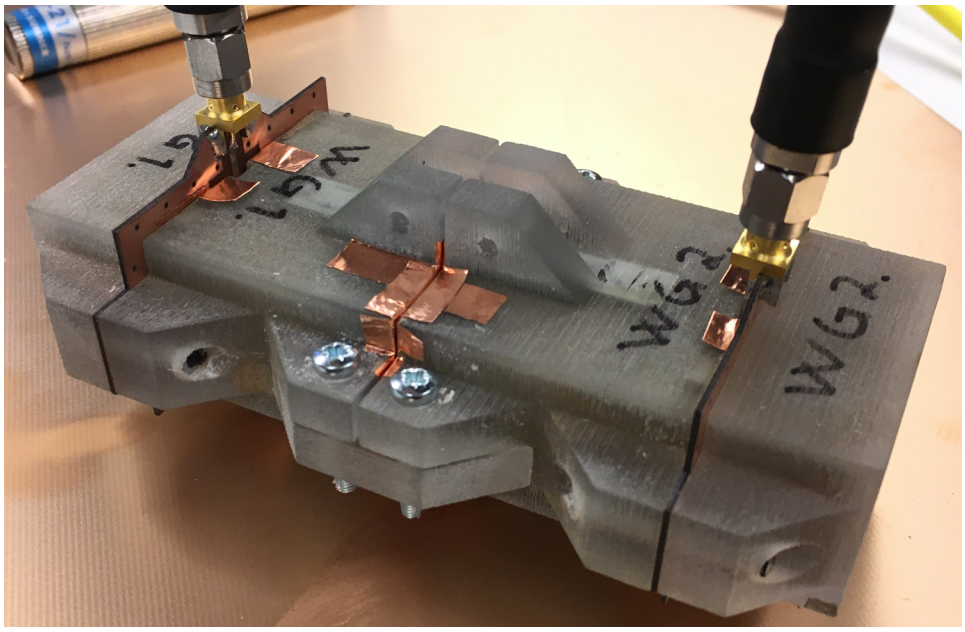

Figure 4.4: Measurement set-up for two waveguides.

Figure 4.5 shows a plot of the reflection coefficient for the simulated waveguide discussed in the previous chapter (black line) and measurements for two different printed waveguides (blue and orange lines). The two plots for the printed waveguides represented in the figure is in fact two identical waveguides printed in different materials. The blue line represents the VeroClear model and the orange line represents a model printed in Polylactic Acid (PLA). The PLA plastic is one sixth of the

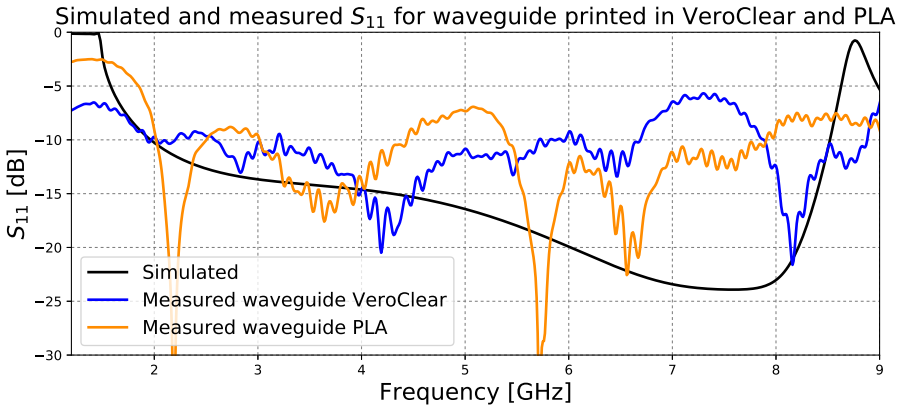

Figure 4.5: Simulated and measured S_{11}.

price of the VeroClear, and it is therefore beneficial to use this if the RF properties are the same. From the figure it is clear that none of the printed models has a good match to the simulated one. For the first printed model, the achieved bandwidth is in between 3.2 GHz to 5.9 GHz, while for the second model the band is split. The first band is between 3 GHz to 4.5 GHz, and the second band between 5.5 GHz to 8 GHz. It is observed from the figure that the cut-off frequency for the simulated and

the two printed waveguides are the same. This means that the waveguide models has a good match to the simulated model. At higher frequencies, the performance starts to decrease. This may be caused by the mechanical implementation. One other theory is that the input not only suffer from reflections from the interface between the PCB and ridge, but also reflections from the second source. In the simulation, a wave-port is used at the end of the waveguide, and not measured against an other model. It is therefore reasonable to believe that reflections from the second source is the main contributor to the difference in the performance.

A plot of S_{21} can be seen in Figure 4.6. The black line shows the simulated result and the blue and orange lines shows the measured results for the first and second printed waveguide, respectively. It is shown that the transmitted signal is attenuated by approximately -5 dB in the frequency range of interest. A 5 dB loss, means a loss of approximately 32 % of the transmitted signal.

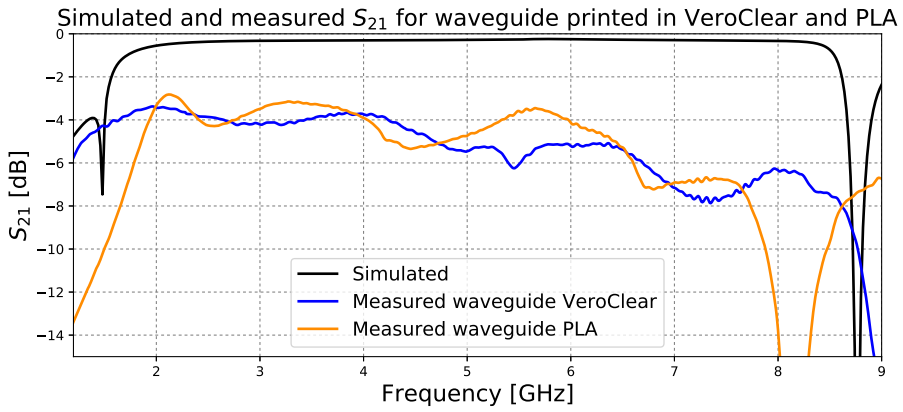

Figure 4.6: Simulated and measured S_{21}.

4.3.2 Summary of the printed waveguide with PCB feed

Despite that the measured results did not entirely meet the simulated result, the performance of the PCB feed looks promising. It was experienced during measurements that the sensitivity of the PCB changed the characteristics of the waveguide. This is due to the thin substrate thickness. For an further improvement, it would be wise to use a thicker substrate for this purpose. However, due to the availability in the lab, only the thin substrate will be used in further measurements.

In this section, measurements on two identical waveguides using different types of materials has been shown. For the VeroClear model, it was experienced that the copper coating did not adhere sufficiently to the surface. This resulted in areas where the model was not entire coated. In the second test, a waveguide printed in PLA was manufactured. It was experienced that copper coating the PLA model was much easier than the VeroClear model. Based on this experiment, the PLA has been used in the further designs.

The measurements on the waveguide was carried out in order to test the performance of the PCB feed. The models were designed in an early stage of the thesis, and turned out to not be suited for the complete antenna system. This has been explained in detail in the previous chapter. In the next section, the performance of the antenna designed in section *3.5.3 Design of stepped ridge horn antenna* will be examined.

4.4 Printed stepped ridge horn antenna

In this section, the evaluation of the 3D printed antenna will be discussed. The printed models was seen in Figure 3.45 in the previous chapter. In this section, the characteristics of the antennas including polarization, gain and bandwidth will be discussed.

4.4.1 Measured reflection coefficient

The simulated and measured reflection coefficient can be seen in Figure 4.7. The simulated bandwidth defined by the -10 dB point was found to be between 2.4 GHz and 5.1 GHz. Measured S_{11} bellow -10 dB for the first printed antenna was found to be between 2.35 GHz and 6.1 GHz. It is shown that the lower cut-off frequency matches the simulated, but the upper frequency is increased by 1 GHz making the antenna more wide-banded. The bandwidth for the second printed antenna is between 1.6 GHz to 6.2 GHz. Except from a variation in the lower cut-off frequency, the antennas perform as expected. A potential reason for the variation of the lower cut-off frequency is mechanical mismatch between the different antenna parts.

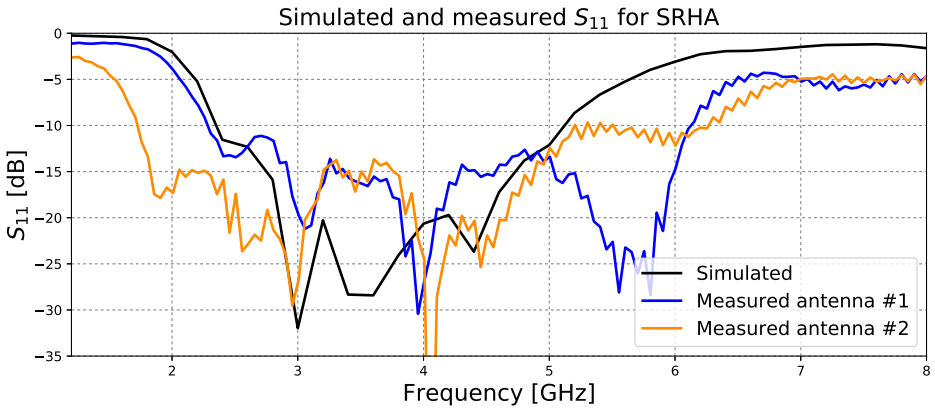

Figure 4.7: Measured and simulated S_{11} for the stepped ridge horn antenna.

A simple stress and strain test was performed to compare the two antennas. A plot of this test can be seen in Figure 4.8 and Figure 4.9. Three different tests have been performed. In the first test (#1.x), the antenna as it originally was designed, have been tested for three different mechanical stresses. The first (# 1.1) is when the PCB feed is not exposed to any pressure at all. This has been done by holding the cable in a position where it does not affects the PCB. The next case (# 1.2) is when pressure is added to the cable and PCB. This is done by lifting the cable so that the PCB establishes best possible contact to the ridge. In the final test (# 1.3), the cable is hanging without any intersections. These three tests has then been performed for two more cases. In the second case (# 2.x), the antenna is kept as is originally was designed, but the PCB feed has been swapped. Antenna #1 has now the PCB feed that was originally used for antenna #2, and the other way around. In the final case (# 3.x), the cavities for the two antennas has been swapped.

Interestingly enough, antenna #1 reacted more to the PCB bending than antenna #2. By switching the cavity between the two antennas, it was observed that the two cavities had different characterization.

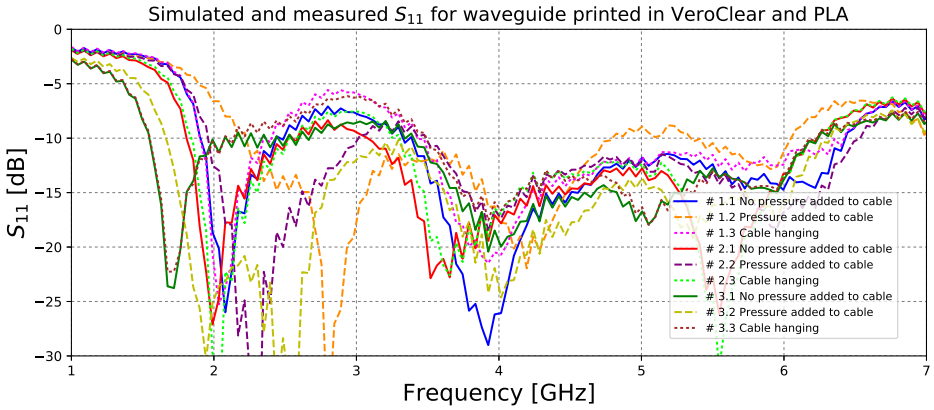

Figure 4.8: Measured S_{11} for different stress tests at antenna #1. # 1.x indicates the original antenna as it was printed, # 2.x indicated the original antenna as it is, but the PCB feed is swapped, and # 3.x indicates that the cavity of the two antennas was swapped.

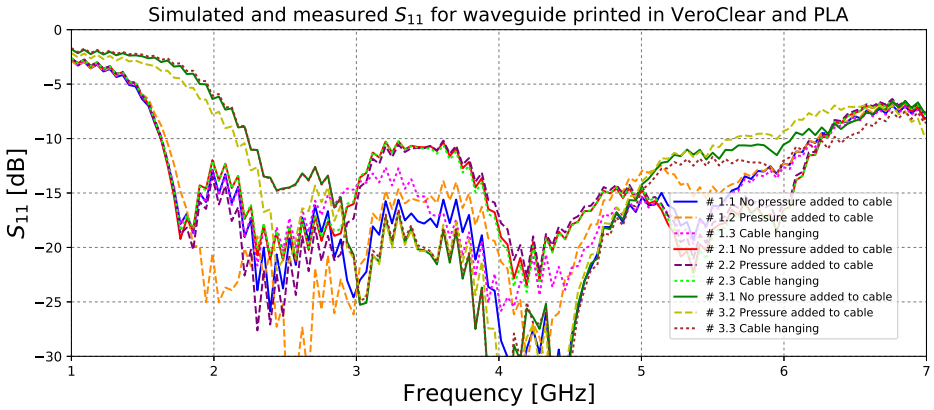

Figure 4.9: Measured S_{11} for different stress tests at antenna #2. # 1.x indicates the original antenna as it was printed, # 2.x indicated the original antenna as it is, but the PCB feed is swapped, and # 3.x indicates that the cavity of the two antennas was swapped

4.4.2 Gain

Figure 4.10 shows a plot of the simulated and measured gain against the frequency for the two printed antennas. Shown in the figure, both the printed antennas performs equally compared to each other. Comparing the simulated and the measured results shows a degradation in the gain. At 2.5 GHz the gain is measured to be approximately 10 dBi for bot antennas. Compared to the measured result, the

gain has been reduced by approximately 1 dB. The gain at 5.5 GHz was measured to be 13 dB. This is much less than the simulated result of approximately 17 dB. On the other hand, it is shown that the measured antennas has a more constant approximation of the gain within the frequency band of interest.

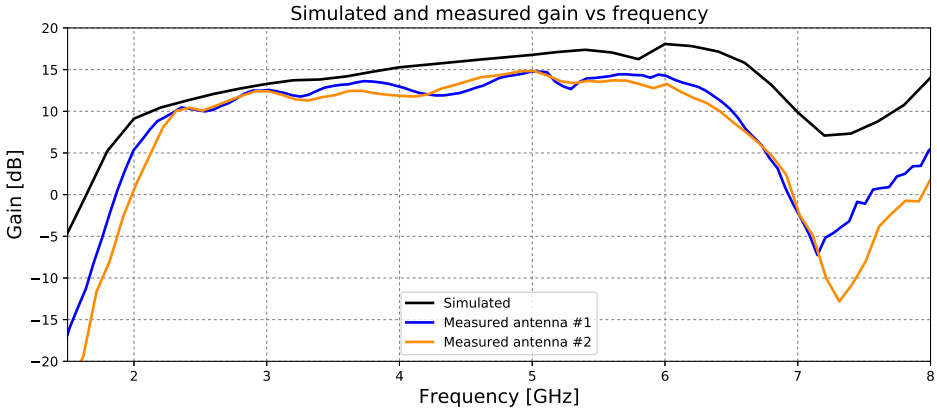

Figure 4.10: Simulated and measured gain versus frequency.

Figure 4.11 shows a plot of the measured and simulated E- and H-plane for the two printed antennas. At 4 GHz, the simulated boresight gain is 15.4 dB and the front-to-back ratio is 22 dB. The simulated half-power-beamwidth (HPBW) is 24° in the E-plane and 26° in the H-plane. The measured boresight gain at 4 GHz for the first printed antenna is 12.6 dB and the front-to-back ratio is 22 dB. The HPBW is 26° in the E-plane and 26° in the H-plane. The second antenna has a boresight gain of 12 dB and the front-to-back ratio is 24 dB. The HPBW was found to be 24° in

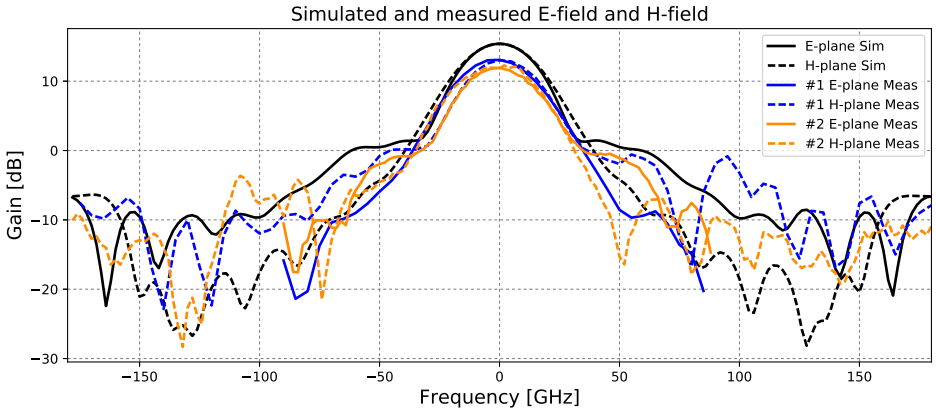

Figure 4.11: Measured and simulated E- and H-field.

the E-plane and 28° in the H-plane. Comparing the simulated and measured results for both antennas, shows that the first printed antenna has reduction of 2.8 dB in the gain, while the second printed antenna has a reduction of 3.4 dB compared to the simulated result. This may be due to resistive losses in the copper coating and glitches between the 3D printed parts.

4.4.3 Polarization

A plot of the simulated and measured co- and cross polarization of the E-plane and H-plane at 4 GHz can be seen in Figure 4.12 and Figure 4.13, respectively.

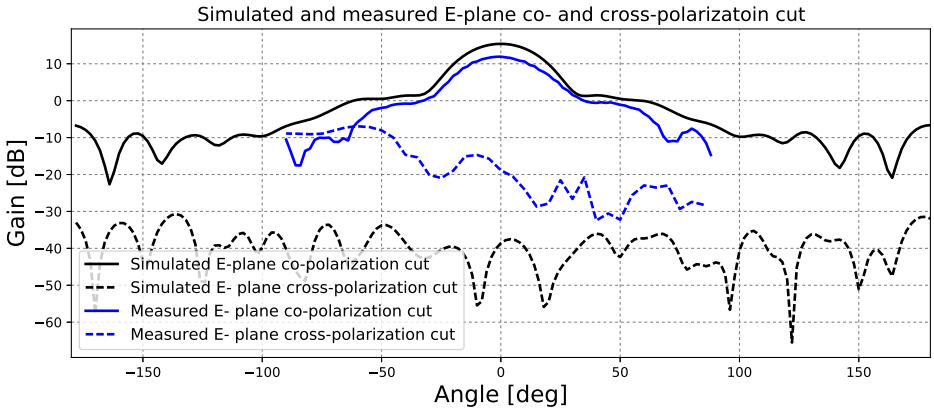

Figure 4.12: Simulated and measured E-plane co- and cross polarization.

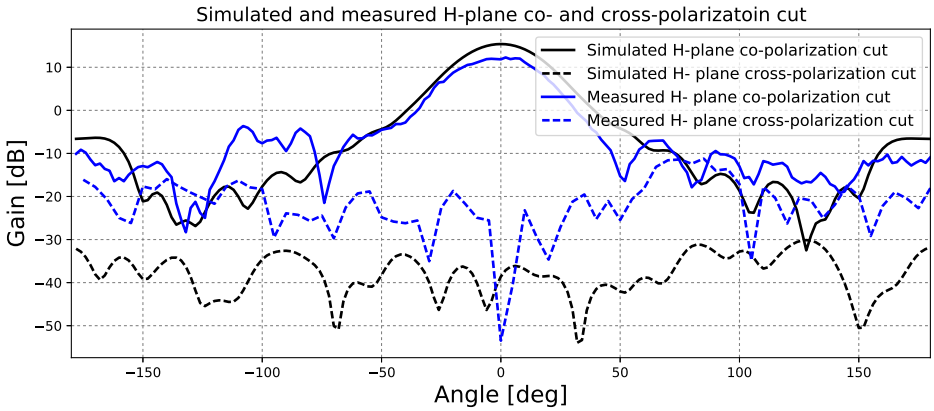

Figure 4.13: Simulated and measured H-plane co- and cross polarization.

It is seen that the measured and simulated cross polarization varies quite much. This may be due to the mechanical challenges for the 3D printed parts. A -20 dB difference between the peak gain in the co-polarization and peak gain in the cross-polarization is acceptable. The simulated and simulated difference in the E-plane cut at 4 GHz and zenith, is approximately 45 dB and 28 dB, respectively. In the H-plane, the simulated and measured co- and cross polarization difference for the same condition is approximately 55 dB and 70 dB, respectively.

4.4.4 Efficiency

As was explained in an earlier section, one possible solution for the degradation in the gain may be due to the efficiency of the antenna. Figure 4.14 shows a plot of the measured and simulated efficiency of the antenna. On the simulated plot, the

antenna has been used the parameters given by MG Chemicals for the copper spray. Yet, the efficiency is approximately equal to 100 % in the band of interest. The efficiency of antenna #2 was measured to be 50-80 % within the band of interest. This is much lower than expected. It is believed that this is due to the glitches between the 3D printed parts and resistive losses in the copper coated layers. For three coated layers, the resistive losses is expected to be 0.011 Ω/sq, according to the manufacturer [64]. This assumes that the entire model is equally coated. In [30], it was found that the conductive paint had much more resistive losses (0.036 Ω/cm) compared to electroplating (0.0006 Ω/cm) and vacuum metalization (0.007 Ω/cm). It is therefore reasonable to believe that the main contributor to the reduced efficiency is due to bad copper coating.

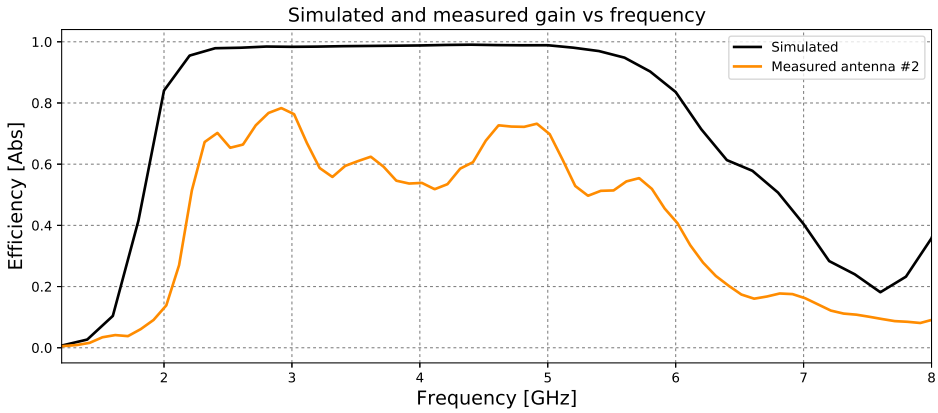

Figure 4.14: Simulated and measured efficiency for antenna #2.

4.5 Radar measurements

Measured results for the two printed antennas shows promising for a complete snow radar system. In this section, the two antennas have been tested at the Snow Lab at the University of Oslo and outdoor measurements at Finse Alpine Research Center. Figure 4.15 shows a 3D printed box created to protect the Ventricorder module. The figure also shows a rail for holding the antennas in right position while measuring.

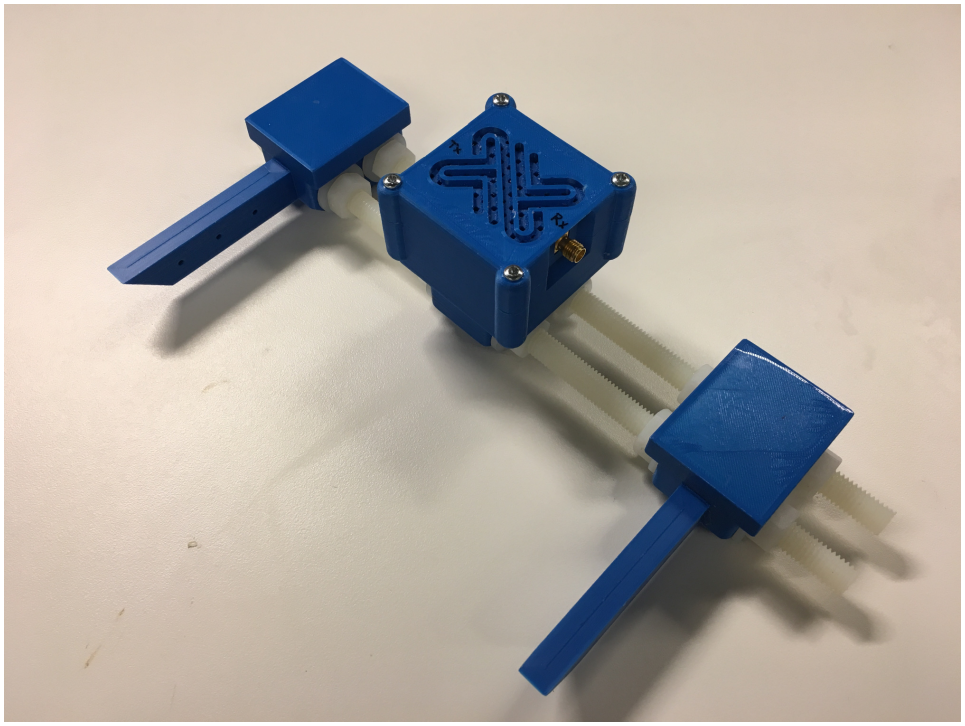

Figure 4.15: The image shows a 3D printed box for protecting the Ventricorder model and rails for holding the measurement setup in the right position.

4.5.1 Snow lab measurements

For the purpose of testing antennas and radar systems intended for snow analysis, it has been created a Snow Lab. The Snow Lab consists of layers of stacked pressed wood plates, as can be seen in Figure 4.16. Pressed wood plates is suitable for this type of analysis because it has a relatively low permittivity. The dielectric constant was measured in-house to be 1.89. This matches the reference values given in [68] and [69]. In Chapter 2, it was shown that the permittivity of snow varies depending on the condition of the snow. The Snow Lab can therefore only be treated as dry snow. For further tests, it is possible to experiment with different types of materials.

The test setup can be seen in Figure 4.17. The radar module is connected to the two antennas using a SUCOFLEX 104P cable. SUCOFLEX is easy to bend, and is therefore suitable regarding the sensitivity of the PCB feed. A PC is connected to the radar to run the diagnostics. The software is written in Matlab, given by Novelda AS. The pressed wood stack-up is four plates stacked upon each other

Figure 4.16: Snow Lab plate stack-up.

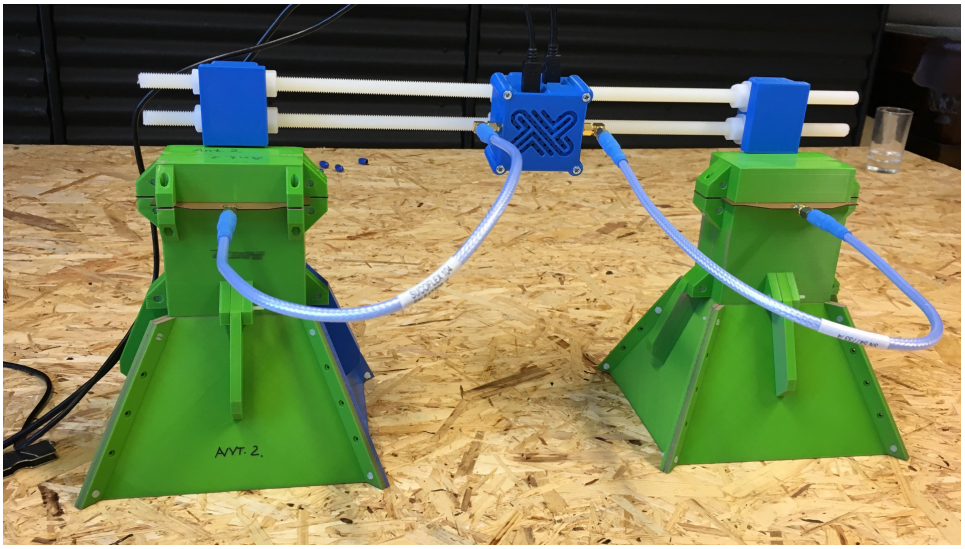

Figure 4.17: Measurement setup for the two antennas and Ventricorder.

with a 20 cm space between each plate. Figure 4.16 shows three plates stacked upon each other.

Figure 4.18 shows the measured result of a four layer stack-up with same spacing between the plates as shown in Figure 4.16. Because of the high gain, a shadow field exists close to the antennas. This shadow field makes the first wood-plat invisible to the radar. The radar is therefore seeing the second plate as the first layer. The size of the shadow field was experimentally found to be approximately 5 cm, meaning that objects that are closer than 5 cm to the antennas will not be discovered. This however, is not an particularly interesting area to detect, because

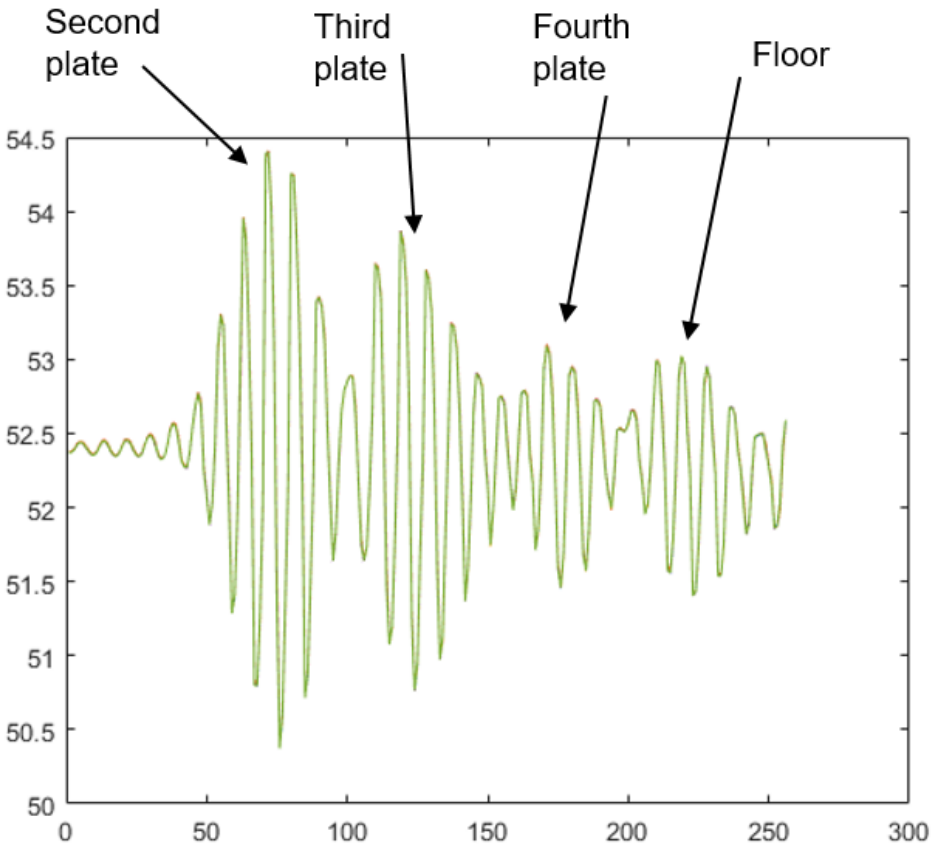

Figure 4.18: Reflected pulses from five plate stack-up measured in the Snow Lab.

one can simply analyze the top snow layer by hand.

Figure 4.19 shows the same results as was presented in Figure 4.18 plotted in colors. The plot is placed besides the snow lab, and shows the distance between each wood layer.
One interesting observation while measuring in the snow lab was that if an object was placed inside one of the air gaps, the RF signal started to change direction. This may be a problem in an outdoor measurements where the ground is not uniform over the entire measuring area. If a rock lays beneath the snow, one may experience that non of the transmitted signal will return.

4.5.2 Field measurements

The field measurements has been carried out at Finse Alpine Research Center, Norway in March, 2017. The purpose of the trip was to get outdoor measurements of the snow using the radar system. To get Real-Aperture Radar (RAR) images a sled for carrying the radar system was made. The radar sled can be seen in Figure 4.20. A box on the back of the sled was created to protect the system from snow and water.

Three different tests were planed to be performed in the field. The first test was to

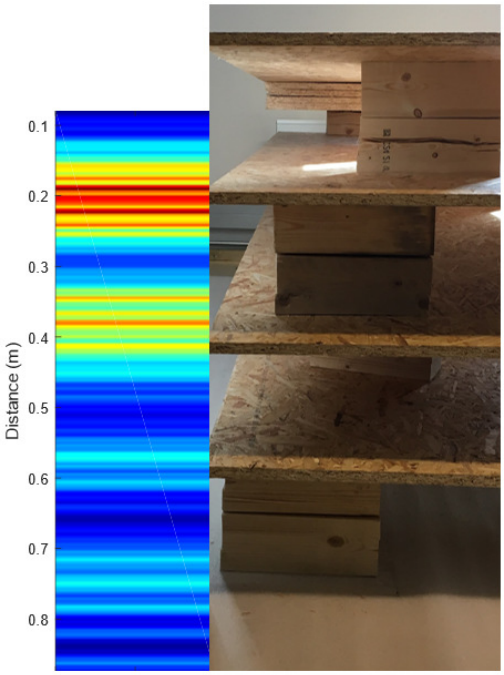

Figure 4.19: The reflected signal plotted in colors, placed beside the snow lab.

Figure 4.20: Reflected pulses from five plate stack-up measured in the Snow Lab.

send one single pulse down into the snow in order to get reflections from each layer. This test is some what similar to the test performed in the lab. The second test was to place the radar at one location and take one measurement for each frequency selection available for the radar. The third and last test, was to perform a RAR analysis over a distance of 75 meters with measurement every second meter. Unfortunately during the field measurement, the microcontroller unit on the Ventricorder module failed. Necessary equipment for re-flashing the Atmel microcontroller was

not brought out in the field. Therefore, only the first two measurements were successful. Figure 4.21 shows the radar sled to the left in action before measurement of the 75 meter long RAR test. The radar to the right, is a similar Ph. D. project at the university.

Figure 4.21: Measurements at Finse Alpine Research Center, Norway. Radar to the lest is the radarsled and to the right is a similar Ph.D. project of a SAR radar.

Figure 4.22 shows the measured results for the single scan measurement with a snow depth of 70 cm. One can clearly see the ground, but analyzing the different snow

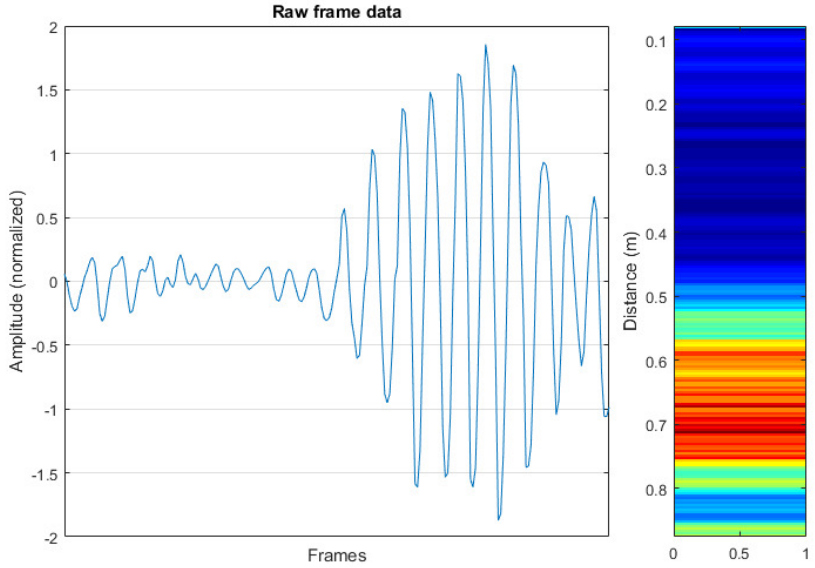

Figure 4.22: Measurements done by placing the radar on a 70 cm deep snow pack.

layers is difficult. Therefore, a snow pit was excavated to see the different layers. These analysis showed that there were two layers of ice located at 25 cm and 50 cm

from the top. Looking at these distances in the figure, reviles two lighter areas. It is believed that these are the two ice layers. However, further signal processing on these results are required on order to see more details. Due to limited time, this was not possible to accomplish.

Figure 4.23 shows the measured results for different PGSelections. PG stands for Pulse Generator and is a function for selecting between different center frequencies between approximately 3.5 GHz to 4.5 GHz in for the Novelda X2 radar module. In Chapter 2, it was seen that the downrange resolution was dependent on the bandwidth. Increasing the center frequency of the X2 radar, means an increase in the bandwidth because the pulse shape is finite. It is therefore interesting to see how the snow measurements changes for different center frequencies. Figure 4.23 does not contain much interesting information as it is presented. This mea-

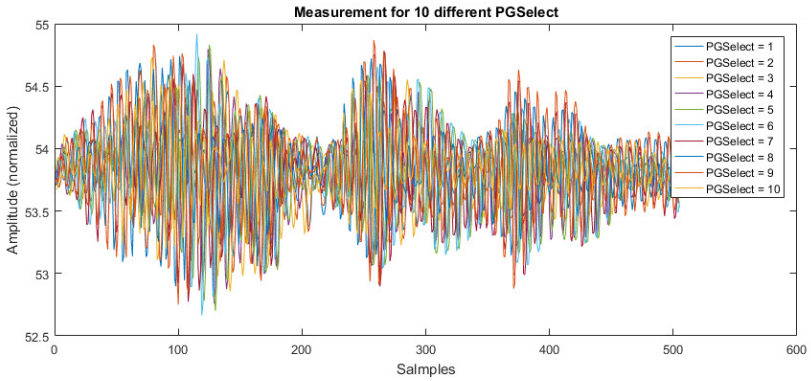

Figure 4.23: Measurements done by changing the PGSelect of the radar.

surements was done for snow depth of approximately 3 meters. Unfortunately, the stitching was not long enough to reach the ground which is the reason why there are no strong signals in the end. A similar color plot as the one shown in Figure 4.22 would not be a good representation, because for such a long distance there will probably be multiple layers which will change the dielectric constant several times as the wave propagates. This can be estimated to make this type of plot, but was not prioritized due to limited time.

4.6 Summary of all results

In this chapter, the results for the final antennas has been presented. It was seen in the first section that the printed waveguide did not performer very well. However, the concept of the PCB feed solution was shown to be promising. One other interesting observation obtained form the waveguide measurements, was that the performance between the low cost PLA and the expensive VeroClear was negligible, in fact it was more difficult to work with the VeroClear model. This is beneficial regarding simplicity and cost. Instead of using professional 3D printers, one can simply use a hobby printer.

In the next section, the performance of the 3D printed antennas was shown and discussed. It was seen that the performance matches the simulated quite good. It is reasonable to believe that the mismatch is caused by mechanical challenges. More on this discussion will be presented in the next chapter.

In the last section, lab- and outdoor measurements were presented. In the lab, the radar system was able to detect each wood layers, which was seen in Figure 4.19. Also, outdoor measurements has been presented, but this data needs further verification by signal processing.

Chapter 5

Discussion

Most of the discussion about the simulated and measured results has been discussed trough the thesis and will not be repeated here. In this chapter, some of the practical issues regarding the fabrication of the 3D printed antennas, along with some difficulties regarding the copper coating of the inside, will be discussed further. In the last section one alternative application will be discussed.

5.1 Issues regarding 3D printing antennas

5.1.1 3D printing

In section *3.6 3D printed antennas*, some discussion regarding the issues that may occur during 3D printing were discussed. One of the main problems that arises are the copper coating on the inside of the plastic horn. Because of this, the model were spitted into several smaller parts and assembled when all parts were coated. Splitting the model is ideally not preferred as the parts may cause mismatch of the performance due to RF leakage through gaps and reflections from uneven surfaces in the joints. It was shown in the previous chapter that the performance of the antenna, especially the antenna efficiency was degraded from the simulated model. It is reasonable to believe that this is caused these problems. Figure 5.1 shows an image of the inside of the antenna. It can be seen from the cavity section that the gap between the upper and lower part are quite big. Also, uneven surfaces in the joints, especially between the waveguide and horn section is quite significant.

A suggestion to this problem would be to split the entire antenna into two models, instead of eight. This however, would result in difficulties regarding 3D printing. The model would have needed lots of support materials in order to print the various geometries. Trade-offs regarding performance and manufacturing is therefor aspects the designer needs to be aware of.

5.1.2 Copper coating

In the datasheet for the MG Chemicals 843AR Super Shield it is specified a sheet resistance for one, two and three layers of copper coating. The difference in the resistance between one and three layers are quite significant. MG Chemicals implies that the resistance of one coated layer (2.3 mil/58μm) is 0.071Ω/sq (14 S), while

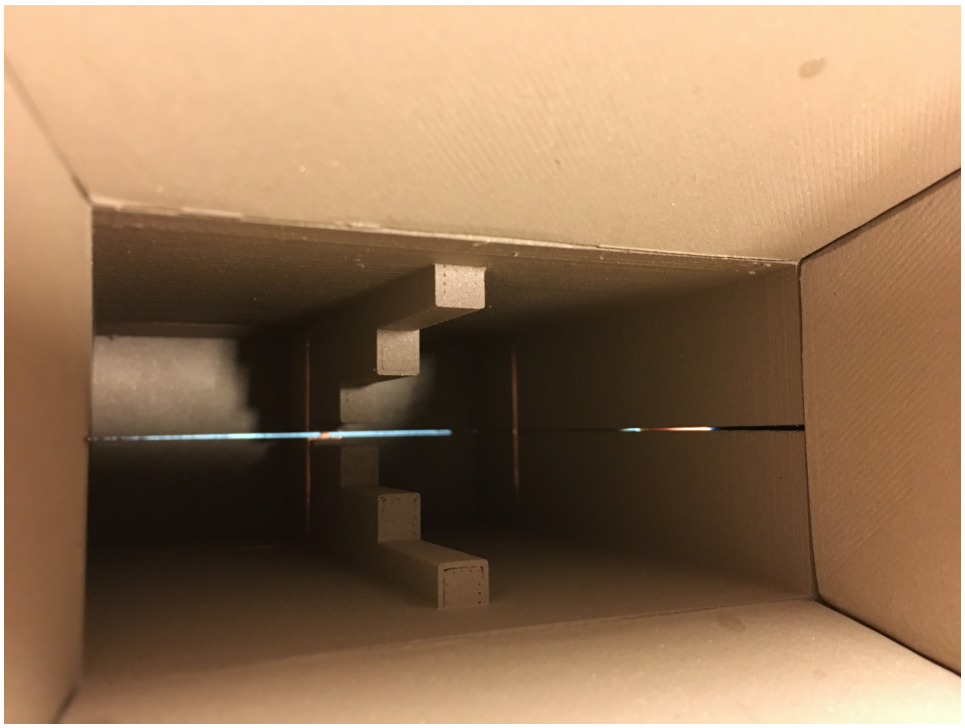

Figure 5.1: Image showing gaps between the 3D printed parts in the waveguide and cavity section.

for three layers (5.4 mil/137μm) there will be 0.011 Ω/sq (91 S) [64]. However, for a practical implementation, the control of each layer thickness will be difficult. It has been assumed that the thickness of the layers are more than enough, but due to some of the shapes in mode, it was difficult to get even layers over the entire antenna. Therefor, this may also be one significant factor regarding the mismatch in the performance.

5.2 Interface between PCB and waveguide

One critical point for the performance of the antenna is the interface between the PCB and the ridged waveguide, as can be seen in Figure 5.2. Figure 5.2 (a) shows the interface between the PCB and the ridged waveguide, and Figure 5.2 (b) shows the interface between the PCB and the cavity. It is very important that the PCB and

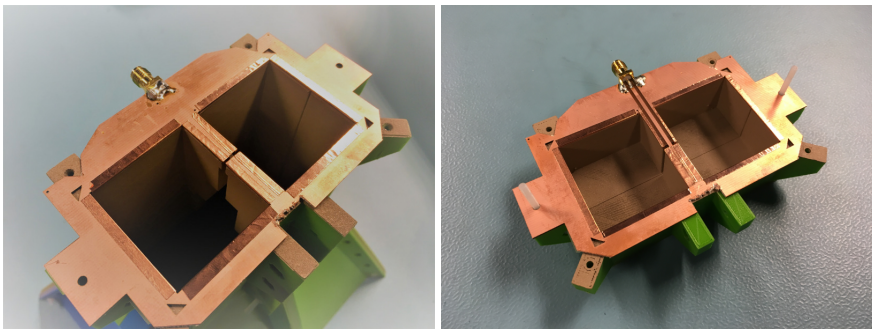

(a) (b)

Figure 5.2: (a) showing interface between the PCB and the waveguide and (b) shows the interface between the PCB and the cavity.

the ridged waveguide has good electrical contact. Therefore, the intersecting part of the cavity and the waveguide as been coated with extra care. In addition, copper tape has been added around the substrate of the inner part of the PCB. This will be discussed more in the next section. Mechanically, there has been added screw holes around the cavity and waveguide to squeeze the parts together for extra electrical protection.

One last thing worth mentioning about the interface between the PCB and ridged waveguide is the coating of the intersecting part of the waveguide. The microstrip is designed as a coplanar waveguide where the width of the trace are matched to 50Ω. As the RF signals propagate along the strip line, it will most likely change its characteristics if the coating of the waveguide is not done properly. When the strip line enters the waveguide (from air), it changes its characteristic into a strip line covered by a ground plane on the top and bottom the the line. This type of strip line requires a different width in order to be matched to 50Ω. Therefore, the area where this is critical, needs to be masked so that there will be no copper in this area. The final result is shown in Figure 5.3

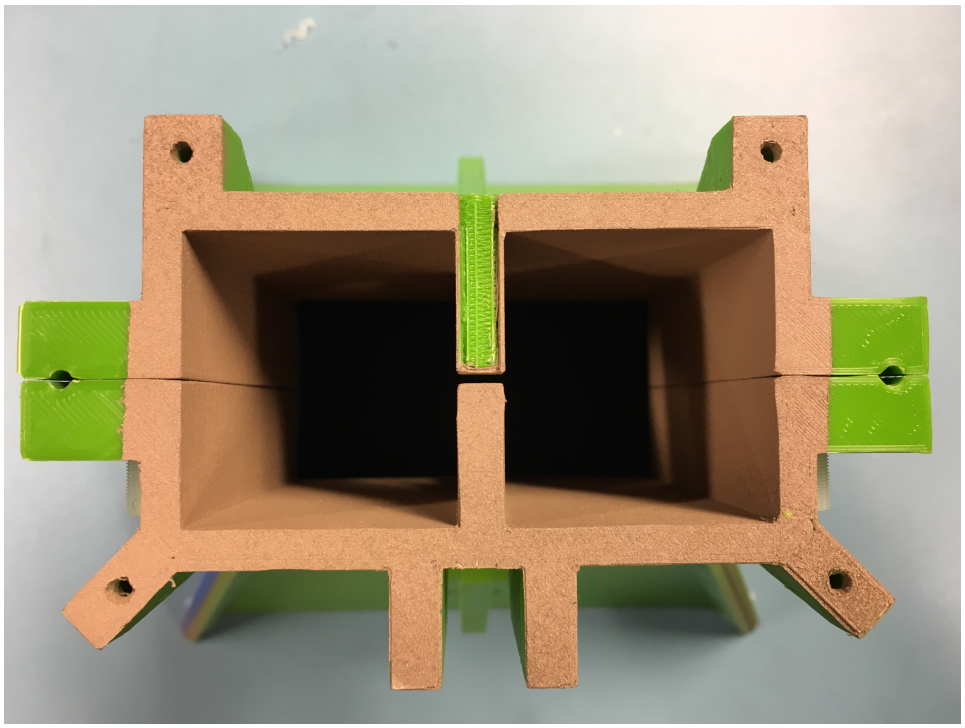

Figure 5.3: Image showing the uncovered area where the microstrip line is going.

5.3 Suggestions for further work

5.3.1 New waveguide design

The waveguide designed for the stepped ridge horn antenna is originally designed using equations for a rectangular waveguide without ridges. This was found to be the best suited solution for the stepped ridge implementation. For the best performance of the ridge, it was found that completing the ridge all the way back to the end of the cavity gave the best result. This is not common use for traditional ridged waveguide, where the cavity is used as a groove for trapping signals going in the opposite direction. Seen in Figure 3.33, the electric field propagated forward in the waveguide, and almost nothing was propagating backwards. The means that the cavity has no other effect than clamping the PCB between the two parts. For an further improvement of the antenna, it is suggested that the cavity is removed on order to reduce the size. Simulations were the length of the cavity were changed has been performed. The results shows that the length has no significant impact on the antenna performance.

In section *4.4.1 Measured reflection coefficient*, it was shown that the lower cut-off frequency was shifted on the second printed antenna. Based on the test shown in Figure 4.8 and Figure 4.9, it is reasonable to believe that the cause of this is an mechanical error caused by the cavity. Splitting the 3D printed parts was necessary in order to ensure proper copper coating. Removing the cavity will therefore minimize the risk of errors in the performance.

5.3.2 PCB feed

It has been shown that the antenna performance is heavily affected by stresses in the feed which is not good in a complete radar system. As an improvement, it would be advisable to use a thicker PCB substrates. The one used in the current design is 0.8 mm thick. Doubling this thickness will probably give a much more stable system. If a thicker substrate with the same dielectric properties are used, a much wider trace is required to match the 50Ω impedance. Therefore, for the same trace width, it would be necessary to use a substrate with a different dielectric.

As the PCB used in this thesis was manufactured in the lab, it does not have any vias. Instead, copper tape was added between the top and bottom copper layer, as can be seen in Figure 5.4. Therefore, ordering a PCB with vias from a manufac-

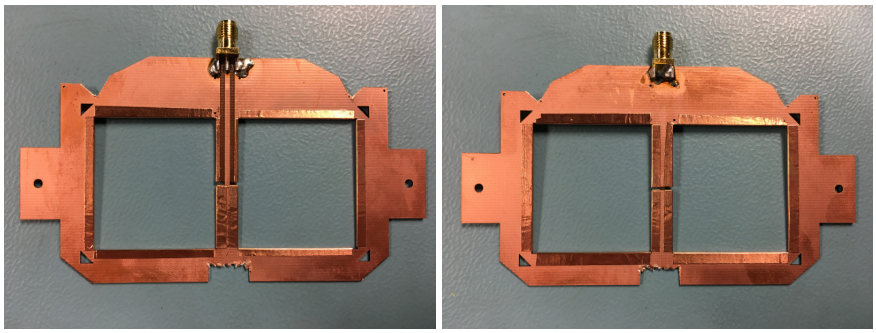

(a) (b)

Figure 5.4: (a) showing the front side of the PCB and (b) shows the back side. Between the two copper layers, there are added a tape to ensure electrical connection between the layers.

turer, would eliminate the manual work of taping the top and bottom layer together. If a PCB is to be ordered, it is important that the areas where there should be contact between the PCB and waveguide is not covered with stencil.

5.3.3 One single PCB for a complete radar system

For a complete radar system, the proposed solution discussed in the previous section is not preferred. Instead, one possible solution would be to design a single PCB including the feeds and the radar hardware. Having one single PCB, would reduce the total cost eliminating the need for coaxial cables. Also, the sensitivity in the PCB will be minimized.

5.4 Alternative radar applications

The main application that has been discussed though this thesis, is imaging of the snow profile to map the potential risk of snow avalanches. One other important discussion is to use radar for human detection in a snow avalanche. There excises few products on the marked that are efficient for detecting buried humans. One solution is the Snow Scan Rescue Radar from Sensors & Software [70], but this system needs movement from the person in order to be detected. Besides the use of radar the most efficient technique the avalanche beacon, but this only works if the affected person have a his or hear own beacon.
Using the presented design on a snow stick, it can easily be carried out on the avalanche area and create RAR images. After a snow avalanche, the snow will be hard and compact, so the dielectric properties will probably be equal for the hole snow pack. Therefore, human detection may be possible.

Chapter 6

Conclusion

This thesis present the design and measurements of two 3D printed stepped ridge horn antennas, suitable for snow imaging and remote Geo-Sensing applications. The antennas have been characterized for air due to small changes between air and dry snow, as have been discussed in Chapter 2. The design specifications were derived based on the requirements for ultra-wideband, high gain antennas required for directive beam measurement of the snow. Modeling and simulations has been performed using Ansys HFSS and the characterization has been performed at the anechoic chamber at the Department of Informatics, University of Oslo.

The presented design is a stepped ridge horn antenna which has been characterized for large bandwidth in the range 2.4 GHz to 6.1 GHz with a high gain over the entire area. Measured results shows that the gain varies between 10 dBi and 15 dBi within this antenna bandwidth. At center frequency (4 GHz), the peak gain was measured to be 12.6 dBi and 12 dBi for antenna #1 and antenna #2, respectively. The measured half-power beamwidth of antenna #1 is 26° in the E-plane and 26° in the H-plane at 4 GHz. For antenna #2 the measured half-power beamwidth is 24° and 28°. Measured front-to-back ratio is 22 dB and 24 dB for antenna #1 and antenna #2, respectively.

The feeding technique for the 3D printed waveguide is proposed by new PCB microstrip solution, replacing the traditional coaxial probe feed solution. The performance of the PCB feed matches the probe feed, as was seen in section *3.4 A new method for feeding plastic waveguide*. The work in this feeding technique has been submitted to the IEEE MTT-S International Microwave Workshop Series on Advanced Materials and Processes (IMWS-AMP) conference (see Appendix A).

The measured results for the antenna has a relatively good match to the simulated, and it is believed that the mismatch is due to mechanical challenges and uneven copper coating of the plastic surface. Referring to Figure 4.8 and Figure 4.9, it was seen the cavity of the first printed antenna shifted up the lower cut-off frequency approximately 800 MHz when it was used together with the second printed antenna. This is believed to be differences in the two 3D printed models. In Chapter 5 that gaps between the 3D printed parts was shown to be remarkable. Also, the same two figures showed that the PCB was highly exposed to mechani-

cal stress. As a further improvement it has been suggested to use a thicker substrate.

Measurements has been performed together with the Novelda X2 Ventricorder module at the university Snow Lab. Also, outdoor measurements at Finse Alpine Research Center has been performed. Based on the measurements, it is believed that the radar are able to distinguish between different snow layers. However, more signal processing needs to be performed to verify this.

Bibliography

[1] L. Dawson. (Sep. 2014). Avatech electronic snow profile sensor & data network, [Online]. Available: https://www.wildsnow.com/14505/avatech-smartphone-app-probe-sp1/ (visited on 05/10/2017).

[2] N. A. (2010). N.a., [Online]. Available: https://www.polartrec.com/files/members/katey-shirey/images/img5510.jpg (visited on 04/19/2017).

[3] "IEEE Standard Letter Designations for Radar-Frequency Bands", *IEEE Std. 521-2002*, pp. 1–10, 2002. DOI: 10.1109/IEEESTD.2003.94224.

[4] Novelda AS. (2015). Xethru x2, [Online]. Available: https://www.xethru.com/x2-uwb-radar-chip.html/ (visited on 04/19/2017).

[5] M. A. Richards, *Fundamentals of radar signal processing*, 2nd ed. USA: Mc. Graw Hill, 2014.

[6] D. J. Daniels, "Ground penetrating radar", in, D. J. Daniels, Ed., 2nd ed. London, UK: The Institution of Electrical Engineers, 2004, ch. 1. Introduction, pp. 1–11.

[7] Wikipedia. (May 2017). History of radar, [Online]. Available: https://en.wikipedia.org/wiki/History_of_radar#Christian_H.C3.BClsmeyer (visited on 05/13/2017).

[8] H. C̃. D. Prospector Inst Fuer Praktisch Geol, "Verfahren zur elektrischen bodenerforschung (a method for electrical ground exploration)", German, Patent DE489434 C, Jan. 1930. [Online]. Available: https://www.google.com/patents/DE489434C?cl=en.

[9] A. P. Annan, *Ground Penetrating Radar Principles, Procedures & Applications*, 1st ed. Mississauga, Canada: Sensors & Software Inc., 2003.

[10] varsom.no. (2017). Snøskredulykker- og hendelser, [Online]. Available: http://www.varsom.no/ulykker/snoskredulykker-og-hendelser/ (visited on 05/13/2017).

[11] J. Floyer. (Dec. 2016). Backcountry conditions, [Online]. Available: http://powdercanada.com/2016/12/backcountry-conditions/ (visited on 05/06/2017).

[12] C. Wolff. (Nov. 1998). Radartutorial.eu, [Online]. Available: http://www.radartutorial.eu/index.en.html (visited on 05/03/2017).

[13] F. T. Ulaby and D. G. Long, *Microwave Radar and Radiometric Remote Sensing*. Ann Arbor, MI: The University of Michigan Press, 2014.

[14] S. Y. Huang, *Loss tangent*, Notes, Feb. 2012.

[15] D. R. Kwok, *Lossy medium*, Lecture slides, Apr. 2015. [Online]. Available: http://www.engr.sjsu.edu/rkwok/EE142/Lossy_Medium.pdf.

[16] T. M. Hallikainen, F. T. Ulaby, and M. Abdelrazik., "Modeling the dielectric behavior of wet snow in 4-18 ghz range", *IEEE International Geoscience and Remote Sensing Symposium*, 31 August - 2 September 1983.

[17] T. M. Hallikainen, F. T. Ulaby, M. C. Dobson, and A. El-Rayes., "Dielectric measurements of soils in the 3 to 37 ghz band between -50 °c and 23 °c", *IEEE International Geoscience and Remote Sensing Symposium*, 27 - 30 August 1984.

[18] T. M. Hallikainen, F. T. Ulaby, and M. Abdelrazik, "The dielectric properties of snow in the 3 to 37 ghz range", *IEEE Transactions on Antennas and Propagation*, vol. 34(11), pp. 1329–1340, 1984.

[19] D. J. Daniels, "Ground penetrating radar", in, D. J. Daniels, Ed., 2nd ed. London, UK: The Institution of Electrical Engineers, 2004, ch. 2. System Design, pp. 13–36.

[20] B. R. Mahafza, *Radar Systems Analysis and Design Using MATLAB*, 1st ed. Huntsville, AL: Chapman & Hall/CRC, 2000.

[21] 3D Radar. (N.A.). Gpr technology, [Online]. Available: http://www.3d-radar.com/?page_id=939 (visited on 05/04/2017).

[22] M. I. Skolnik, *Introduction to RADAR Systems*, 3rd ed. Nagar, New Delhi: McGraw-Hill, 2001.

[23] C. A. Balanis, "Modern antenna handbook", in, C. A. Balanis, Ed., 1st ed. Hoboken, NJ: John Wiley & Sons, 2008, ch. 1. Fundamental Parameters and Definitions for Antennas, pp. 3–56.

[24] Sensors & Softwares. (). Pulseekko, [Online]. Available: https://www.sensoft.ca/products/pulseekkopro/overview/ (visited on 05/02/2017).

[25] National Avalanche Center. (N. A.). Starting zone the portion of an avalanche path where an avalanche releases., [Online]. Available: http://www.fsavalanche.org/starting-zone/ (visited on 05/02/2017).

[26] National Avalanche Center. (N. A.). A snowpack stratum differentiated from others by weather, metamorphism, or other processes., [Online]. Available: http://www.fsavalanche.org/layer-snow/ (visited on 05/02/2017).

[27] S. Greffin and T. Pippett, "Ground penetrating radar", *Geophysical and Remote Sensing Methods for Regolith Exploration (CRCLEME)*, vol. 144, pp. 80–89, 2002.

[28] J. Lux. (2000). Soil dielectric properties, [Online]. Available: http://pe2bz.philpem.me.uk/Comm/-%5C%20Antenna/Info-905-Misc/soildiel.htm (visited on 05/05/2017).

[29] S.-. E. Hamran, "Ground penetrating radar", in, D. J. Daniels, Ed., 2nd ed. London, UK: The Institution of Electrical Engineers, 2004, ch. 11.4. GPR sounding of polythermal glaciers, pp. 455–460.

[30] K. V. Hoel, S. Kristoffersen, J. Moen, K. G. Kjelgård, and T. S. Lande, "Broadband antenna design using different 3d printing technologies and metallization processes", *10th European Conference on Antennas and Propagation (EuCAP)*, pp. 1–5, 2016.

[31] V. Midtbøen, K. G. Kjelgård, and T. S. Lande, "3d printed horn antenna with pcb microstrip feed for uwb radar applications", *Progress in IEEE MTT-S International Microwave Workshop Series on Advanced Materials and Processes (IMWS-AMP)*, 2017.

[32] Wikipedia. (Apr. 2017). Parabolic antenna, [Online]. Available: https://en.wikipedia.org/wiki/Parabolic_antenna (visited on 05/02/2017).

[33] H. Schantz, *The Art and Science of Ultrawideband Antenna*, 2nd ed. Norwood, MA: Artech House, 2015.

[34] J. Huang, "Modern antenna handbook", in, C. A. Balanis, Ed., 1st ed. Hoboken, NJ: John Wiley & Sons, 2008, ch. 4. Microstrip Antennas: Analysis, Design, and Applications, pp. 97–156.

[35] A. De, C. K. Chosh, and A. K. Bhattacherjee, "Design and performance analysis of microstrip patch array antennas with different configurations", *International Journal of Future Generation Communication and Networking*, vol. 9(3), pp. 97–101, 2016.

[36] W. F. Croswell, T. Durham, M. Jones, D. Schaubert, P. Friederich, and J. G. Maloney, "Modern antenna handbook", in, C. A. Balanis, Ed., 1st ed. Hoboken, NJ: John Wiley & Sons, 2008, ch. 12: Wideband Arrays, pp. 581–629.

[37] R. C. Tylor, B. A. Munk, and T. E. Durham, "Wideband phased array antenna and associated methods", United States, Patent US6512487 B1, Jan. 2003. [Online]. Available: https://www.google.com/patents/US6512487.

[38] D. T. Emerson. (1998). The work of jagadis chandra bose: 100 years of mm-wave research, [Online]. Available: https://www.cv.nrao.edu/~demerson/bose/bose.html (visited on 05/01/2017).

[39] S. A. Schelkunoff and H. T. Friis, *Antennas: Theory and Practice*, 1st ed. NY, USA: John Wiley & Sons, Inc, 1952, Appendix VI.

[40] ETS-Lindgren, *Emc antennas: Double-ridge waveguide horn*, 2014. [Online]. Available: http://www.ets-lindgren.com/pdf/3115.pdf (visited on 05/01/2017).

[41] S. J. Orfanidis, *Electromagnetic Waves and Antennas*, 1st ed. Rutgers University: Sophocles J. Orfanidis, 2016.

[42] K. Blattenberger. (2017). Coaxial cable equations, [Online]. Available: http://www.rfcafe.com/references/electrical/coax.htm (visited on 05/07/2017).

[43] K. Blattenberger. (Sep. 2016). Rectangular & circular waveguide: Equations, fields, & fco calculator, [Online]. Available: https://www.rfcafe.com/references/electrical/waveguide.htm (visited on 09/05/2016).

[44] K. L. Walton and V. C. Sundberg, "Broadband ridged horn design", *Microwave J.*, pp. 96–101, 1964.

[45] W. H. Pickering *et al.*, "Waveguide handbook", in, N. Marcuvitz, Ed., 1th ed. New York, NY: Dover Publications, 1951, ch. 8. Composite Structures, pp. 387–413.

[46] C. Granet, G. L. James, and A. R. Forsyth, "Modern antenna handbook", in, C. A. Balanis, Ed., 1st ed. Hoboken, NJ: John Wiley & Sons, 2008, ch. 3. Aperture Antennas: Waveguides and Horns, pp. 157–200.

[47] J. J. Carr and G. W. Hippisley, *Practical Antenna Handbook*, 5th ed. USA: McGraw-Hill Companies, 2012, pp. 447–489.

[48] MicrowaveTools.com. (Dec. 2016). Pin-fed pyramidal horn, [Online]. Available: http://www.microwavetools.com/pin-fed-pyramidal-horn/ (visited on 12/19/2016).

[49] S. Hopfer, "The design of ridged waveguides", *IRE Transactions on Microwave Theory and Techniques*, vol. 3, pp. 20–29, 1955.

[50] T. S. Bird and A. W. Love, "Antenna engineering handbook", in, J. L. Volakis, Ed., 4th ed. Upper Saddle River, NJ: McGraw-Hill Education, 2004, ch. 14. Horn Antennas.

[51] Y. Yang, Y. Wang, and A. E. Fathy, "Design of compact vivaldi antenna arrays for uwb see through wall applications", *Progress In Electromagnetic Research (PIER)*, vol. 82, pp. 401–418, 2008.

[52] F. Karshenas, A. R. Mallahzadeh, and A. Imani, "Modified tem horn antenna for wideband applications", *International Symposium on Antenna Technology and Applied Electromagnetics and the Canadian Radio Science Meeting*, pp. 1–5, 2009.

[53] C. Sarkar, "Some parametric studies of vivaldi antenna", *International Journal of u- and e- Service, Science and Technology*, vol. 7, pp. 323–328, 2014.

[54] T. A. Milligan, *Modern Antenna Design*, 2nd ed. Hoboken, NJ: John Wiley & Sons, 2005, pp. 356–372.

[55] B. Majumdar, D. Baer, S. Chakraborty, K. P. Esselle, and M. Heimlich, "Advantages and limitations of 3d printing a dual-ridged horn antenna", *Microwave and Optical Technology Letters*, vol. 58, pp. 2110–2117, 2016.

[56] J.-C. S. Chieh, B. Dick, S. Loui, and J. D. Rockway, "Development of a ku-band corrugated conical horn using 3-d print technology", *IEEE Antennas and Wireless Propagation Letters*, vol. 13, pp. 201–204, 2014.

[57] E. Pucci, E. R. Iglesias, J. L. V. Roy, and P.-S. Kildal, "Planar dual-mode horn array with corporate-feed network in inverted microstrip gap waveguide", *IEEE Transactions on Antennas and Propagation (SUBMITTED)*, vol. 62(7), pp. 3534–3542, 2014.

[58] D. M. Pozar, *Microwave Engineering*, 4th ed. USA: John Wiley & Sons, 2012, pp. 261–267.

[59] Y. Zhou, E. Li, G.-F. Guo, T. Yang, and L. Liu, "Design of millimeter wave wideband transition from double-ridge waveguide to coax line", *J Infrared Milli Terahz Waves*, vol. 32, pp. 26–33, 2011.

[60] Antenna Magus. (2012). Coax to dual-ridged rectangular waveguide transition, [Online]. Available: http://www.antennamagus.com/database/antennas/antenna_page.php?id=304 (visited on 02/14/2017).

[61] S. B. Cohn, "Properties of ridge wave guide", *Proceedings of the IRE*, vol. 35(8), pp. 783–788, 1947.

[62] A. H. Systems, *SAS-571 Double Ridge Guide Horn Antenna*. [Online]. Available: http://www.ahsystems.com/datasheets/SAS-571_Horn_Antenna_Datasheet.pdf (visited on 03/08/2017).

[63] E. Huber, M. Mirzaee, J. Bjorgaard, M. Hoyak, S. Noghanian, and I. Chang, "Dielectric property measurement of pla", *Electro Information Technology (EIT), 2016 IEEE International Conference on*, pp. 0788–0792, 2016.

[64] MG Chemicals, *Super shield silver coated copper conductive coating 843ar technical data sheet*, 2017. [Online]. Available: http://www.mgchemicals.com/downloads/tds/tds-843ar-l.pdf (visited on 03/12/2017).

[65] Wikipedia. (Mar. 2017). Fused deposition modeling, [Online]. Available: https://en.wikipedia.org/wiki/Fused_deposition_modeling (visited on 04/20/2017).

[66] C. R. Garcia, R. C. Runpf, H. H. Tsang, and J. H. Barton, "Effects of extreme surface roughness on 3d printed horn antenna", *Electronics Letters*, vol. 49(12), pp. 1–2, 2013.

[67] Stratasys Ltd, *Veroclear (rgd810)*, 2016. [Online]. Available: https://goo.gl/pYn40M (visited on 03/12/2017).

[68] C. Thajudeen, A. Hoorfar, and F. Ahmad, "Measured complex permittivity of walls with different hydration levels and the effect on power estimation of twri target returns", *Progress In Electromagnetics Research B*, vol. 30, pp. 177–199, 2011.

[69] Clipper Controls. (2017). Dielectric constant values, [Online]. Available: http://www.clippercontrols.com/pages/Dielectric-Constant-Values.html (visited on 04/26/2017).

[70] Sensors & Software. (N. A.). Snowscan overview, [Online]. Available: https://www.sensoft.ca/products/snowscan/overview/ (visited on 05/13/2017).

Appendices

Appendix A

Paper

The following paper has been submitted to the “IEEE MTT-S International Microwave Workshop Series on Advanced Materials and Processes (IMWS-AMP) conference” Acceptance status is as of this writing not yet known.

3D Printed Horn Antenna with PCB Microstrip Feed for UWB Radar Applications

Vegard Midtbøen, Kristian G. Kjelgård, Tor S. Lande
Department of Informatics,University of Oslo, Norway
Email: vegard.midtboen@fys.uio.no, {kristigk,bassen}@ifi.uio.no

***Abstract*—In this paper, a 3D printed Double Ridge Horn Antenna (DRHA) for mobile snow cover monitoring is presented. The DRHA is designed for high bandwidth and high gain as required for a pulsed radar system. The bandwidth is between 2.4 and 5.1 GHz with an in-band gain between 12 to 14 dBi. The antenna parts are fabricated with a standard 3D printer using light-weighted plastic material (PLA). The surface is copper coated on the inside adding conductivity. A PCB plate is inserted as feed for 3D printed plastic waveguides replacing traditional coaxial probe feed. The antenna has a total weight of less than 400g and the total cost is about $60. Both cost and weight is significantly lower than commercially available DRHAs adding fast and easy prototyping. Low weight, high gain and large bandwidth makes this antenna suitable for mobile systems like snow cover analysis.**

I. Introduction

In applications where low weight, geometric flexibility as well as low cost is desired, 3D printed antennas may offer advantages where machined, metal antenna fall short. Surprisingly good performance is attainable with easy and fast prototyping. Typically, in mobile applications like Unmanned Aerial Vehicles (UAV) light weight antennas are desired and may even be integrated as an integral mechanical part of the mobile platform [1]. However, challenges exist fabricating antennas in plastic materials like proper conductive coating, mechanical stability and robustness. Still, our initial experiments are promising although somewhat different design procedures are required.

In countries with snow covered mountains, snow cover assessment is important especially for snow avalanche risk determination. Today fairly manual time-consuming methods are used like digging a pit in the snow or inserting a pole in the snow pack and sense the mechanical resistance. Due to very few real observations risk assessment is both difficult and inaccurate. In order to increase observation density, better, faster and more observations are desired. Our project is to bring forward an electronic "pole" for snow assessment using a miniaturized radar system. A mobile radar beam is looking downwards into the snow pack and continuously measuring while dragging a radar-sled over the terrain.

Our snow assessment radar sled is built around a single chip CMOS, UWB radar [2]. For proper radar SAR imaging resolution, a center frequency of 4 GHz with a signal bandwidth of 1.5 GHz is adopted. A key component for proper operation is antennas adding gain and focus. Aiming for high gain some sort of horn derivative antenna architecture should provide desired performance, but commercially available horns are expensive, heavy and some add significant dispersion degrading performance.

3D printing technology has made low cost high-quality mechanical prototyping fast and easy. The consumer/semi-pro 3D printer market is dominated by simple Fused deposition modelling (FDM) machines using low cost thermoplastic polymers (ABS, PLA). Various metallization processes of 3D printed microwave components such as electroplating and spray painting may add conductive surfaces [3], [4]. In [3] an original antenna in aluminium was compared with a 3D printed copy using electroplating and metal spray paint. Radiation pattern and reflection coefficient of the original and 3D printed antenna matched within the measurement error proving the feasibility of 3D printed horn antennas. Still further refinement is required towards the interface between 3D printed parts and RF source. Traditional coaxial feeds with SMA connector are expensive, heavy and less compatible with 3D printed parts requiring soldering or mechanical fixture [5], [6]. In addition, special considerations are required for robust operation of 3D printed feed structures.

In this paper, we propose a new DRHA design optimized for snow radar assement. The antenna is 3D printed and metallized with conductive spray. A transmission line implemented on a Printed Circuit Board (PCB) line directly feeding the antenna ridges.

II. Design

DRHA are often designed for maximum bandwidth by tapering the ridges from the bottom of the feed to the horn edge, even extended outside the horn. Conventional tapering trades very wide bandwidth match for non-linear gain severely distorting the wideband pulse transmitted. To widen the bandwidth of un-ridged horns without sacrificing the gain at lower frequency we designed a new tapering profile. By stepping the ridge down to the horn surface inside the waveguide section, the impedance matching is maintained over the required bandwidth with flat gain. The dimensions of the desired waveguide is determined from [7]. For a cut-off frequency of f_c = 2 GHz and a center frequency of f_0 = 4 GHz, width a = 74.95 mm and hight b = 37.47 mm is required. The size of each step is shown in Fig. 1.

Raising the impedance from 50 Ω signal to 377 Ω air within the waveguide will take advantage of the high gain provided by the horn aperture. The dimensions of the horn aperture can be

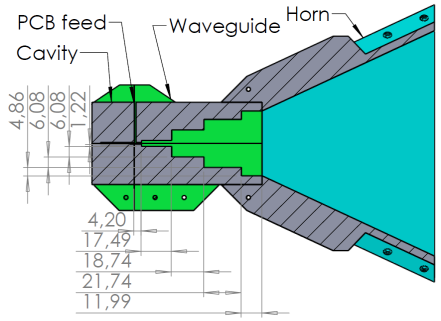

Fig. 1. Horn antenna tapering cross section

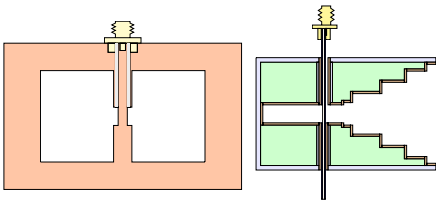

Fig. 2. Microstrip PCB cross section front / side

determined by equations for a rectangular horn antenna given in the literature [8]. For practical purposes, the height, width and length of the aperture was chosen to be 130 mm, 160 mm and 100 mm, respectively sufficiently close to modeled requirements. In Fig. 1 a cross section of the tapering profile and horn aperture is presented.

Sensitivity to mechanical stress and strain on RF cable and mechanical joints is a challenge with plastic antennas. Several 3D printing filaments with different properties are available, but in this experiment, we have evaluated the simplest and less expensive (PLA) type and by design ensure proper mechanical stability. A standard coaxial feed structure is typically a screw-type coupling through the metal feed further soldered directly to the antenna fixture. However, soldering directly on plastic is not feasible. Our solution is to use a mechanically stable waveguide design on a PCB to be inserted in a proper feed position of the waveguide. The waveguide is simply designed with a split for clamping the PCB feed between two sections of the ridged waveguide. In Fig. 2 a cross section of the horn waveguide and the PCB feed is illustrated. The PCB feed is designed as a Co-Planar WaveGuide (CPWG) transmission line to the ridge waveguide transition. The mechanical stress from the RF cable is now distributed over the PCB and a complete feed is assembled by clamping the two parts of the ridge waveguide together. A SMA connector is soldered to the PCB feed for standard RF cables. A system with the radar chip directly soldered on the feed PCB is envisioned.

III. Results

Two identical antennas were 3D printed, metallized and assembled. The antenna pattern, gain and reflections coefficient (S_{11}) was measured in the MilliLab (Nano, Dept of Informatics, UiO) anechoic chamber. The chamber is 6x3x3m and equipped with a full spherical rotation rig, VNA and reference antenna. In Fig. 3 the normalized simulated and measured E-plane and H-plane cut of the radiation pattern of antenna #2 at 4 GHz is shown. At 4 GHz the simulated boresight gain is 15 dB and the front-to-back ratio is 22 dB. The simulated half-power beamwidth (HPBW) is 24° in the E-plane and 26° in the H-plane. For antenna #2 the measured boresight gain at 4 GHz is 13 dB and front-to-back ratio is 22 dB. The HPBW is measured to be 24° in the E-plane and 28° in the H-plane. It is shown that the peak gain is decreased by 2 dB compared to the simulated model. However, the HPBW and the front-to-back ratio for the measured antenna matches the simulated result.

The gain plotted against the frequency, and S_{11} of both antennas are shown in Fig. 5. Expect from the variation in the S_{11} lower cut-off frequency the antennas perform as expected. A probable reason for variation of the S_{11} lower cut-off is mechanical mismatch between the different antenna parts.

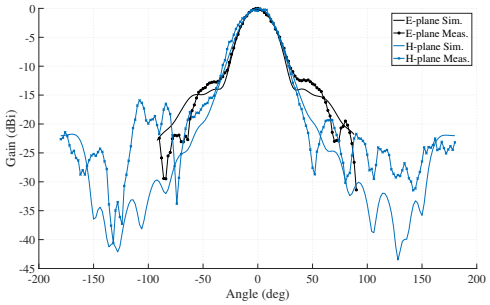

Fig. 3. Measured/Simulated Normalized Radiation Pattern 4 GHz

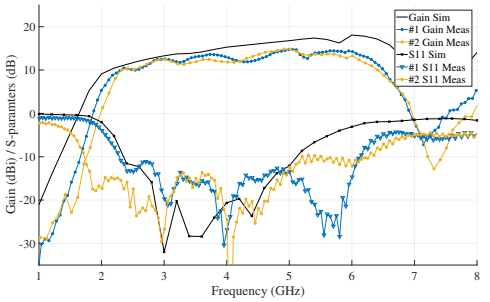

Fig. 4. Measured Gain and S11

A simple stress and strain test was performed comparing two antennas variations. Interestingly enough, antenna #1 reacted more to PCB bending than antenna #2. By switching the cavity between antennas, we observed that the two cavities had different characteristics. The cavity for the antenna #1 increased the cut-off frequency for both antennas. These variations are believed to originate from uneven surface of mechanical parts and possibly also glitches.

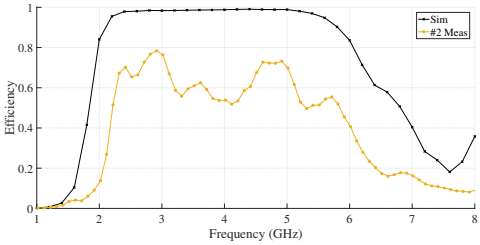

Fig. 5. Antenna radiation efficiency

The efficiency of antenna #2 was measured to be 50-80 %. We believe that this is caused by the glitches between the 3D printed parts and resistive losses in the copper coated layers. For three coated layers, the resistive losses is expected to be 0.011 Ω/sq, according to the manufacturer [9]. This assumes that the entire model has uniformly coating covering (not easy with manual spaying). In [3], it was found that the conductive paint had much more resistive loss (0.036 Ω/cm) compared to electroplating (0.0006 Ω/cm) and vacuum metallization (0.007 Ω/cm). It is therefore expected that the efficiency would decrease compared to the simulated model. In order to reduce the risk of non uniform coating, the antenna has been split into smaller models. Still uniform manual spraying is difficult and probably the primary reason for degraded efficiency.

Fig. 6 and Fig. 7 shows an image of the two 3D printed horn antennas and a prototype of a snow cover radar inspection system. The antennas are printed in PLA plastic using Ulimaker 3 and copper coated with the *843AR Super Shield* [9]. The system was tested at Finse Alpine Research Center, Norway in March 2017.

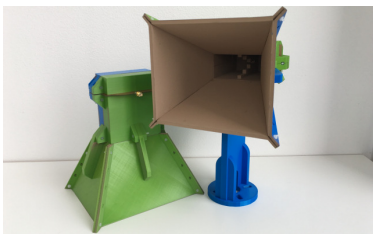

Fig. 6. 3D printed horn antennas.

Fig. 7. Radar sled.

IV. Conclusion

A new 3D printed DRHA design is presented. A stepped ridge inside the waveguide portion of the horn enable wide-band impedance matching while maintaining the gain of the non-ridged horn. With a measured gain of 12-14 dB from 2.3 to 6 GHz, symmetric radiation pattern and good match the antenna provide the characteristics required in our snow radar-sled. To reduce weight and cost of the antenna, Low-cost 3D printing technology combined with simple copper metal spray is used. Compared to commercial metal antennas, cost and weight is significantly reduced. A slightly lower efficiency than expected is measured which is due to surface resistance and glitches antenna parts. The PCB feed developed for 3D printing is distributing mechanical stress and simplifying the RF connection. A system with radar chip and antenna feed on a single PCB is feasible for further development.

References

[1] K. V. Hoel, S. Kristoffersen, J. Moen, G. Holm, and T. S. Lande, "Characterization of a 3d printed wideband waveguide and horn antenna structure embedded in a uav wing," in *2016 10th European Conference on Antennas and Propagation (EuCAP)*, April 2016, pp. 1–4.

[2] N. AS, "X2 impulse radar transceiver," 2014. [Online]. Available: https://www.xethru.com/x2-uwb-radar-chip.html/

[3] K. V. Hoel, S. Kristoffersen, J. Moen, K. G. Kjelgrd, and T. S. Lande, "Broadband antenna design using different 3d printing technologies and metallization processes," in *2016 10th European Conference on Antennas and Propagation (EuCAP)*, April 2016, pp. 1–5.

[4] E. G. Geterud, P. Bergmark, and J. Yang, "Lightweight waveguide and antenna components using plating on plastics," in *2013 7th European Conference on Antennas and Propagation (EuCAP)*, April 2013, pp. 1812–1815.

[5] A. Prigaud, S. Bila, O. Tantot, N. Delhote, and S. Verdeyme, "3d printing of microwave passive components by different additive manufacturing technologies," in *2016 IEEE MTT-S International Microwave Workshop Series on Advanced Materials and Processes for RF and THz Applications (IMWS-AMP)*, July 2016, pp. 1–4.

[6] B. Majumdar, D. Baer, S. Chakraborty, K. P. Esselle, and M. Heimlich, "A 3d printed dual-ridged horn antenna," in *2016 International Conference on Electromagnetics in Advanced Applications (ICEAA)*, Sept 2016, pp. 836–839.

[7] J. J. Carr and G. W. Hippisley, *Practical Antenna Handbook*, 5th ed. USA: McGraw-Hill Companies, 2012, pp. 370–383.

[8] G. L. J. C. Granet and A. R. Forsyth, *Modern Antenna Handbook*, 1st ed. Hoboken, NJ: John Wiley & Sons, 2008, ch. 3. Aperture Antennas: Waveguides and Horns, pp. 118–119.

[9] M. Chemicals, "Super shield silver coated copper conductive coating 843ar technical data sheet," 2017. [Online]. Available: http://www.mgchemicals.com/downloads/tds/tds-843ar-l.pdf

Appendix B

Machine drawings

Machine drawings for Stepped Ridge Horn Antenna v4.1.

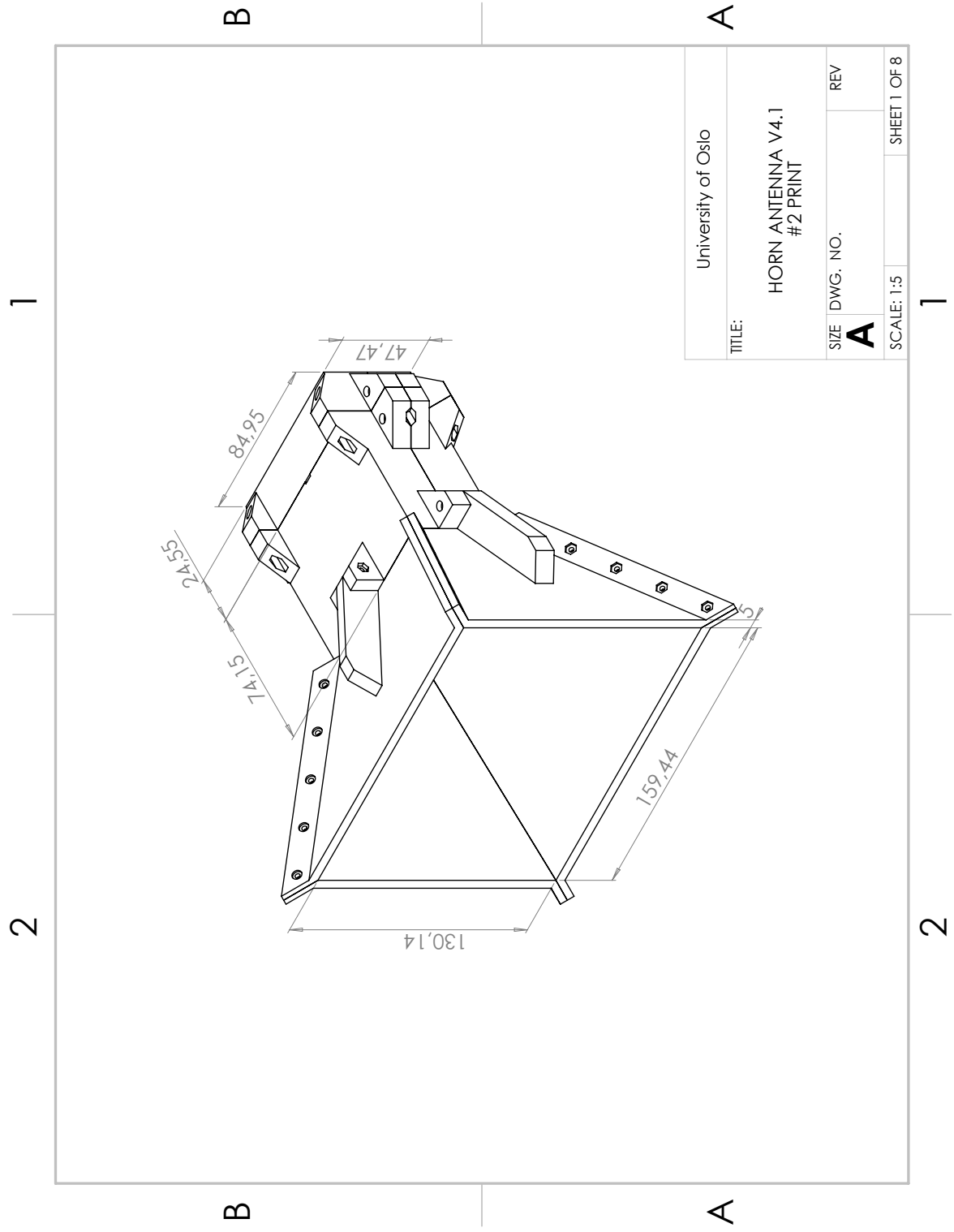
B
A
1
2
University of Oslo
TITLE:
HORN ANTENNA V4.1
#2 PRINT
SIZE
A
DWG. NO.
REV
SCALE: 1:5
SHEET 1 OF 8
47,47
84,95
24,55
74,15
5
159,44
130,14

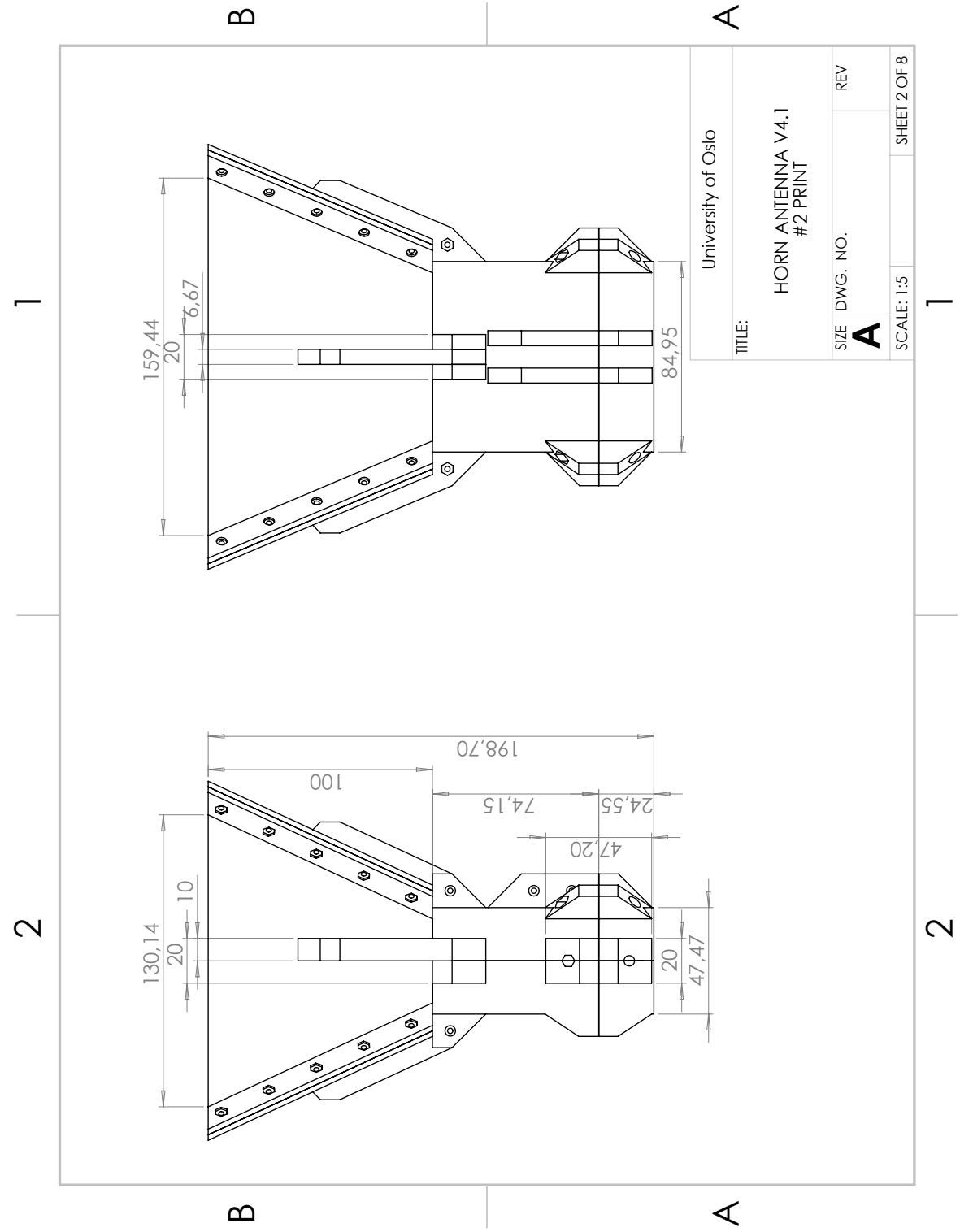
B
A
1
2
159,44
20
6,67
84,95
198,70
100
74,15
24,55
47,20
130,14
20
10
20
47,47
University of Oslo
TITLE:
HORN ANTENNA V4.1
#2 PRINT
SIZE
A
DWG. NO.
REV
SCALE: 1:5
SHEET 2 OF 8

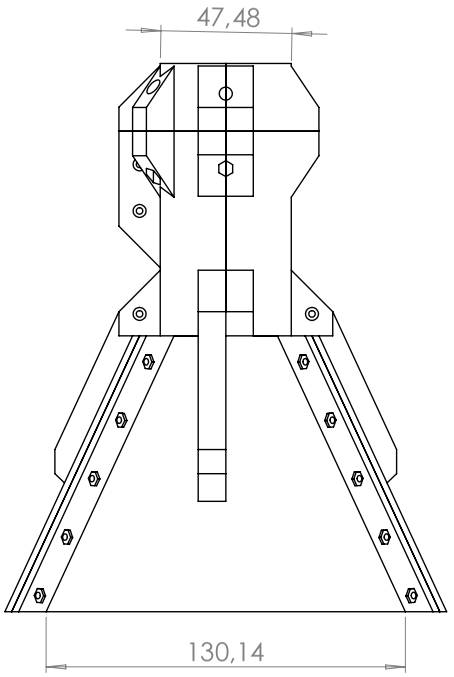

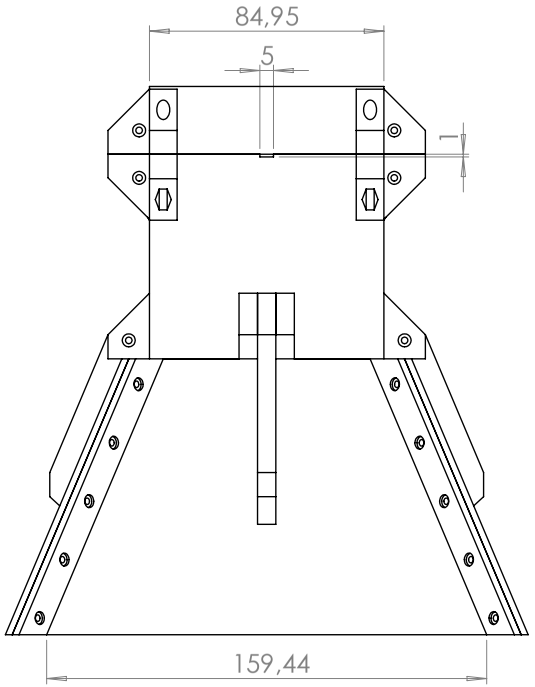

University of Oslo		
TITLE: HORN ANTENNA V4.1 #2 PRINT		
SIZE A	DWG. NO.	REV
SCALE: 1:5		SHEET 3 OF 8

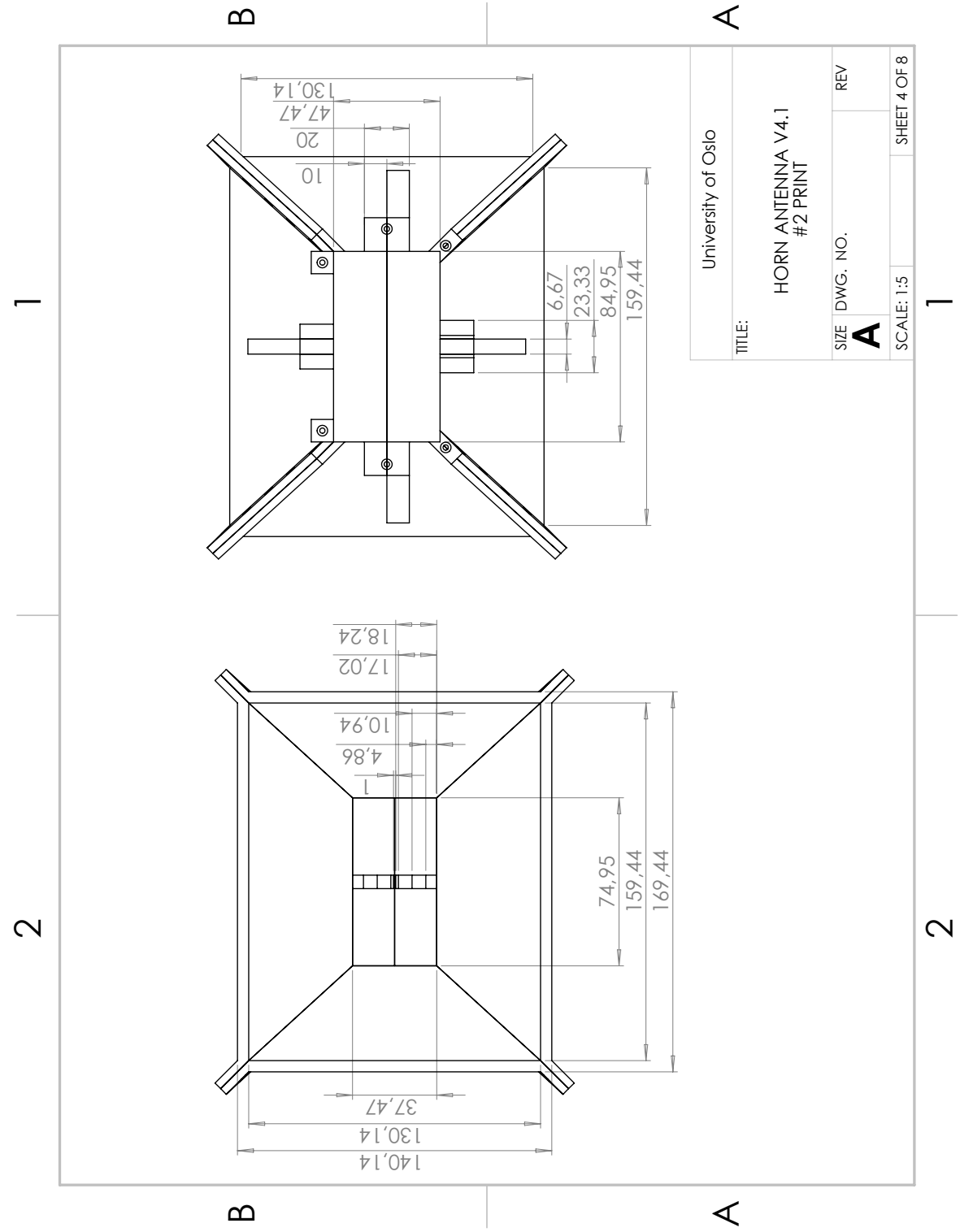
B
A
1
2
130,14
47,47
20
10
6,67
23,33
84,95
159,44
18,24
17,02
10,94
4,86
1
74,95
159,44
169,44
37,47
130,14
140,14
University of Oslo
TITLE:
HORN ANTENNA V4.1
#2 PRINT
SIZE
A
DWG. NO.
REV
SCALE: 1:5
SHEET 4 OF 8

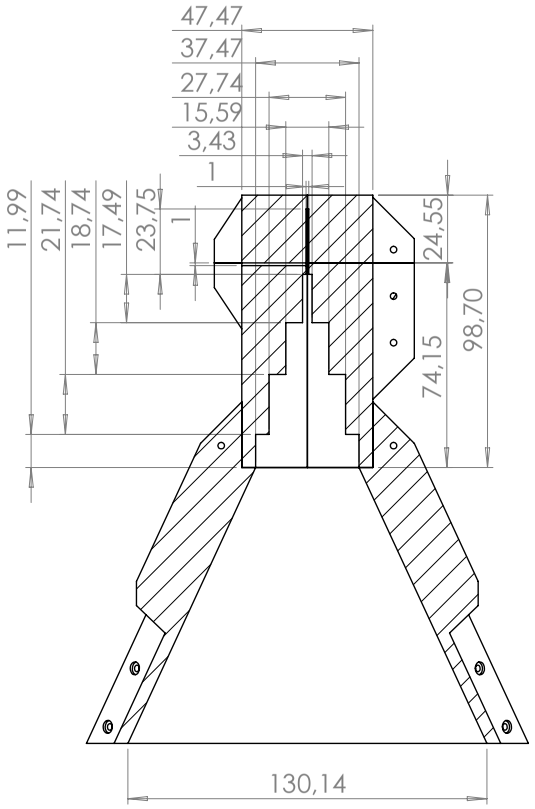

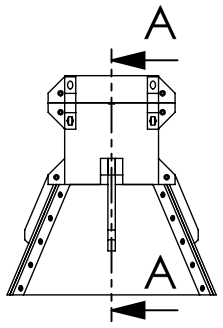

SECTION A-A

SCALE 1 : 2

University of Oslo		
TITLE: HORN ANTENNA V4.1 #2 PRINT		
SIZE A	DWG. NO.	REV
SCALE: 1:5		SHEET 5 OF 8

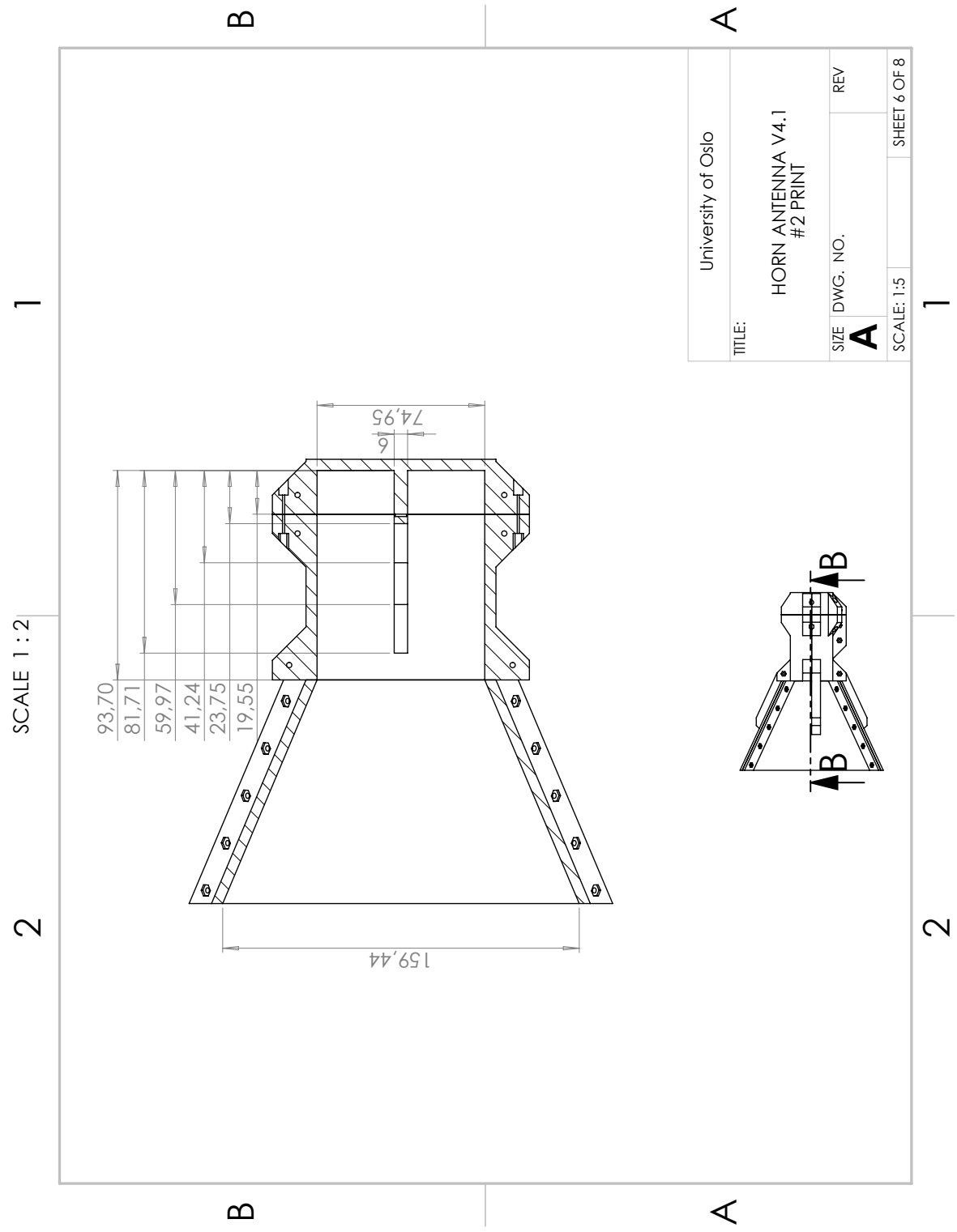
B
A
1
2
SCALE 1 : 2
University of Oslo
TITLE:
HORN ANTENNA V4.1
#2 PRINT
SIZE A
DWG. NO.
REV
SCALE: 1:5
SHEET 6 OF 8
74,95
6
93,70
81,71
59,97
41,24
23,75
19,55
159,44
B
B

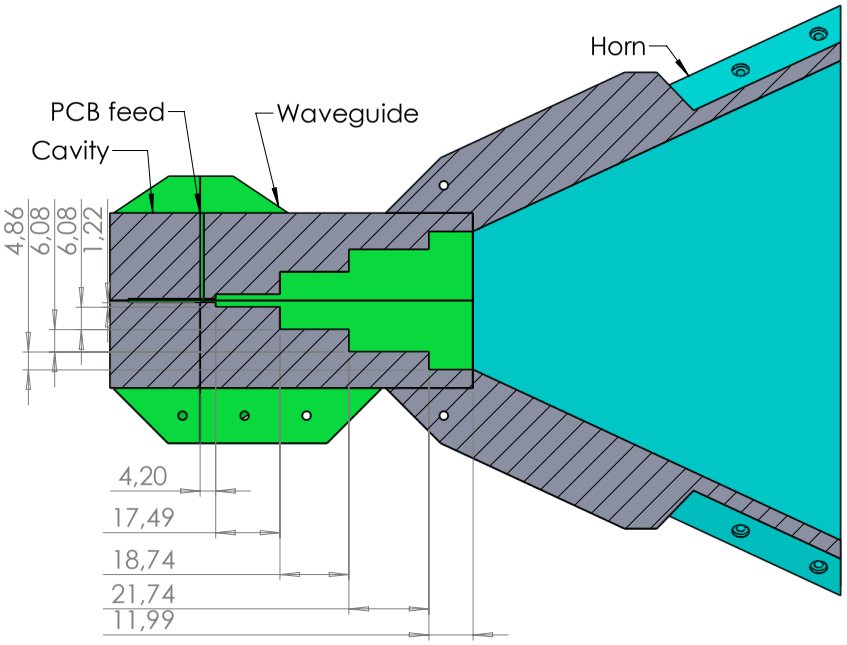

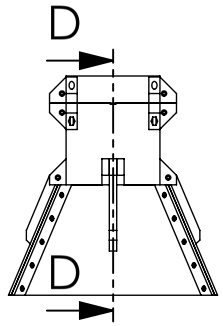

SECTION D-D

SCALE 1 : 1.5

University of Oslo		
TITLE: HORN ANTENNA V4.1 #2 PRINT		
SIZE A	DWG. NO.	REV
SCALE: 1:5		SHEET 7 OF 8

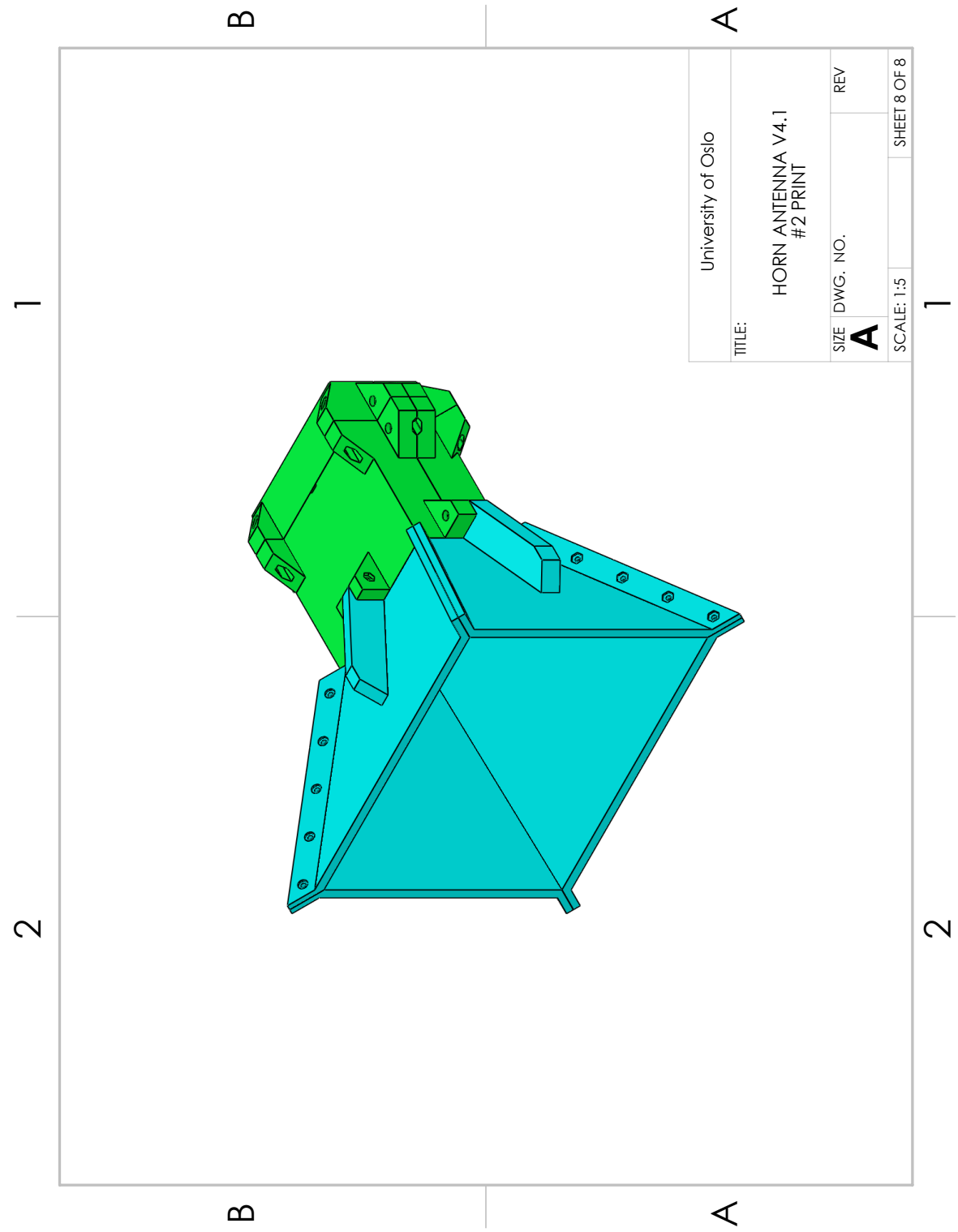
B
A
1
2
University of Oslo
TITLE:
HORN ANTENNA V4.1
#2 PRINT
SIZE
A
DWG. NO.
REV
SCALE: 1:5
SHEET 8 OF 8